UNIVERSITY OF SOUTHAMPTON

INSTITUTE OF SOUND AND VIBRATION RESEARCH
FACULTY OF ENGINEERING, SCIENCE AND MATHEMATICS

A FLEXURAL WAVE SCATTERING METHOD FOR DAMAGE DETECTION IN BEAMS

by

Simon Paul Shone

Thesis submitted for the degree of

Doctor of Philosophy

October 2006

UNIVERSITY OF SOUTHAMPTON

ABSTRACT

FACULTY OF ENGINEERING, SCIENCE AND MATHEMATICS
INSTITUTE OF SOUND AND VIBRATION RESEARCH

DOCTOR OF PHILOSOPHY

A FLEXURAL WAVE SCATTERING METHOD FOR DAMAGE DETECTION IN BEAMS

by Simon Paul Shone

This thesis considers the use of the wave approach for damage detection in beams. It is proposed that the existence of damage can be predicted and its location and depth estimated by measurement of the wave scattering coefficients in the frequency domain. Importantly, the wavelengths considered here are much longer than the dimensions of the cross-section of the beam.

Here, a damaged beam with a transverse notch or slot is modelled using finite element (FE) analysis. This model offers a more detailed description of the shape of the damage and its dynamic characteristics than conventional analytical models. The FE model is assembled to semi–infinite spectral elements, which impose infinite boundary conditions at each end of the FE model. A wave superposition method is then used to estimate the scattering coefficients.

The scattering coefficients are estimated experimentally for a number of beams containing slots. These were made by cutting through the width of the cross-section. The measured reflection coefficients are compared with numerical results to estimate the slot depth and good agreement is found between the actual and estimated slot depths. Experimental errors and noise can make it difficult to estimate the scattering coefficients, particularly at low frequencies or when the reflection coefficient is small (e.g., a small slot).

It is shown how the location of the slot can be estimated, either from the reflection coefficient or the phase of the point frequency response function. Both variables include modulation that is related to the distance between the sensors and the slot. An inverse Fourier transform, applied to the reflection coefficient in the wavenumber domain and transforming into the spatial domain, is used to estimate the location of the slot. Moreover, this method can also be used to locate more than one slot. The accuracy of the estimated slot location depends on the resolution in the spatial domain, which depends on the frequency range used in the analysis; the resolution is approximately equal to half the minimum flexural wavelength.

The results in this thesis show that the reflection coefficient offers a useful feature for detecting damage in beams. The main limitation lies in the fact that experimental error and noise make it difficult to detect small slots. From the results given here, the method works best when the slot depth, and hence the reflection coefficient, is large.

Acknowledgements

I would like to thank my supervisors Brian Mace and Tim Waters for the many hours spent ruminating, cogitating, aiding and abetting. Their comments were always helpful and, I am left to say, it was a pleasure to work with them.

I would like to thank the members of my internal review panel, Mike Brennan and Paul White. I found their additional input helpful and I thank them for their time.

Also, I want to thank all those at the ISVR who I have met along the way. They have provided a wealth of friendship and distraction as needed.

Finally, I wish to acknowledge and thank my parents who have supported me throughout my studies. I am very grateful.

Abbreviations

NDT	Non-destructive testing.
SHM	Structural health monitoring.
VBDD	Vibration-based damage detection.
FRF	Frequency response function.
FE	Finite element.
SE	Spectral element.
FESE	Combined finite and spectral element.
LRT	Longitudinal rod theory.
LVRT	Love rod theory.
EBT	Euler-Bernoulli beam theory.
TBT	Timoshenko beam theory.
DSM	Dynamic stiffness matrix.
*k*IFT	Inverse Fourier transform in the wavenumber domain.
*k*IFFT	Inverse fast Fourier transform in the wavenumber domain.

Symbols

Material symbols

E	Young's modulus.	A	Area of the cross-section.
ρ	Mass density.	I	Second moment of area.
υ	Poisson's ratio.	G	Shear modulus.
g	Radius of gyration.	κ	Timoshenko shear coefficient.
b	Width of beam.	h	Height of beam.

Variables and degrees of freedom

f	Frequency [Hz].	ω	Frequency [rads./s] ($\omega = 2\pi f$).
t	Time variable.	x, y	Co-ordinates.
u, v	Displacement x and y	ψ	Rotation.
$\phi, \boldsymbol{\phi}$	General degrees of freedom.		

Forces

F	Axial force.	C	External axial force.
Q	Shear force.	P	External transverse force.
M	Bending moment.	B	External moment.
σ	Stress.	$\mathbf{p}$	Nodal forces.

Damage variables

D	Notch/slot depth.	γ	Non-dimensional Notch/slot depth.
W	Notch/slot width.	K	Stiffness.
$\mathcal{K}$	Stress intensity factor.	$\mathcal{G}$	Energy release rate.

Wavenumbers

k_0 Longitudinal wavenumber.

k_s Shear wavenumber.

k_L Love rod wavenumber.

k_b Euler-Bernoulli flexural wavenumber.

k_t Timoshenko wavenumber for propagating waves.

k_n Timoshenko wavenumber for nearfield waves.

k_e Experimental wavenumber.

Wave scattering variables

$a, \mathbf{a}$ Wave amplitudes.

$R, \mathbf{R}$ Reflection coefficients. $T, \mathbf{T}$ Transmission coefficients.

r, t Power reflection and transmission coefficients.

Damage location

Λ Spatial variable. f_s Frequency sampling vector.

k_s Wavenumber sample vector. Δf Frequency sample spacing.

k_s' Wavenumber re-sampled vector. Δk Wavenumber sample spacing.

Other symbols

m Mass. $\mathbf{M}$ Mass matrix.

K Stiffness. $\mathbf{K}$ Stiffness matrix.

η Damping loss factor. $\mathbf{C}$ Damping matrix.

$\mathbf{D}$ Dynamic stiffness matrix. $\mathbf{H}$ Receptance matrix.

$\mathbf{\Omega}$ Transformation matrix. $\mathbf{I}$ Unit matrix.

μ Accelerance.

Vector quantities are denoted in lower-case bold font and matrices in upper-case bold font.

CONTENTS

LIST OF FIGURES

1. Introduction

1.1. Background

Non-destructive testing (NDT) of damage in structures has been of interest to engineers for many years. The term damage is taken to mean a change in the structure that can lead to an adverse affect on its integrity, safety and performance. Damage and failure of structures can be both costly and catastrophic. NDT allows engineers to survey structures, assess damage and maintain the structures; thereby, increasing the life of a structure and improving performance and safety.

It is desirable that damage is detected at the earliest possible moment. The structure is therefore monitored for damage and this is referred to as structural health monitoring (SHM). In principle, a SHM system monitors a structure for the occurrence and progress of damage. This might also include identifying the damage, estimating its severity, its location, and developing a prognosis of the remaining life of the structure.

1.1.1. Structural health monitoring

Evaluating the health of a structure is much like medically treating a sick patient. An overview of how a SHM system might be designed is given in [1, 2]; in summary the main points are:

1. establish possible damage scenarios;

2(a). feature selection;

2(b). define what data is to be acquired;

2(c). numerical analysis and evaluation of chosen features;

3. testing and data processing;

4. diagnosis and

5. prognosis.

These steps are elaborated more in [1, 2]. One of the most important steps is selecting a feature. A feature is a variable or parameter that is monitored, a change in which is used to signify damage. Drawing on a medical analogy, this might be considered similar to a symptom. It is from the recording and measurement of the features that a diagnosis and prognosis can be made. The sensitivity of the chosen feature to damage is therefore very important because a more sensitive feature means that the damage is easier to detect.

The diagnosis and prognosis steps (4 and 5) are often separated into the following [2, 3]:

- Diagnosis

  i. Existence: predicting the possible existence of damage in a structure.

  ii. Location: predicting the location of damage.

  iii. Extent: predicting the extent of the damage.

- Prognosis

  iv. Consequence of the damage, e.g., remaining life of the structure.

At each stage, our knowledge of the damage increases. Although stages i and ii might be accomplished by direct experimental methods alone, often stages iii and iv (in particular) require models, be they numerical or experimental, of the damage and the structure. The

diagnostic stage determines damage specific data, whereas prognosis is damage and structure dependent. Prognosis is a much more complex problem than diagnosis and may require a great deal of information about the structure, such as the working conditions, loading and fatigue behaviour, to name a few.

A SHM monitoring system is designed with a specific application in mind. Certain NDT methods may be inappropriate for certain structures, particular types of damage or environmental conditions. A number of desirable features might be identified and some examples are given in the following:

- the ability to detect damage from measurements elsewhere on the structure (remote sensing);
- practicality, e.g., suitable for use under working conditions;
- sensitive to small scale damage; and
- robustness (e.g., to changes in environmental or working conditions).

One benefit of remote sensing in damage detection is that damage can be detected using a number of fixed measurement locations, which monitor the whole structure. This is particularly useful when it is either impractical, dangerous or costly to move sensor devices manually.

Various methods have been considered for SHM in the past, some of which are discussed in [1]. Of particular interest here are vibration-based methods of damage detection for SHM. Previous work in this area is reviewed in chapter 2. One of the challenges in this field is finding a feature that is sensitive to small damage but can still be measured remote from the damage site. For example, where some ultrasonic methods can be sensitive to small damage, the monitoring must be local to the damage site;

conversely, where modal methods can be insensitive to small damage, the features can be measured remote from the damage site.

1.2. Aims and scope of the thesis

The aim of this thesis is to explore the use of wave scattering as a means for vibration-based damage detection in beams. This focusses on the use of the wave scattering coefficients as a feature for diagnosing a transverse slots cut into the beam, i.e., estimating existence, depth and location. This is motivated by the desire to find a feature that can be measured remote from the damage site, can be used to describe the properties of the slot and is sensitive to small damage.

Using waves that have wavelengths longer than the dimensions of the cross-section of the beam, it may be possible to detect the slot through measurements of the wavefield at locations remote from the damage site. It is assumed that the scattering coefficients depend on the slot shape and, hence, might be used to estimate its depth. Furthermore, wave propagation methods might also make it possible to locate the slot.

This thesis considers damage in mechanical structures, as might be found in civil, mechanical and aerospace engineering, concentrating on homogeneous and isotropic beams. Although the methods considered here may be equally applicable to non-uniform beams and composite beams, these types of structure are not considered.

1.3. Structure of the thesis

The chapters in this thesis are structured as follows:

2. Vibration-based damage detection This chapter reviews research in the area of

vibration-based damage detection (VBDD), covering the recent past and state of the art. This chapter highlights some of the methods currently under investigation and summarises the advantages and limitations of these approaches.

3. **Modelling wave scattering from discontinuities** This chapter reviews methods for modelling the wave motion and wave scattering in one-dimensional waveguides. Analytical methods for estimating wave scattering coefficients of a discontinuity are reviewed. A numerical method is used to model discontinuities, which uses a combination of finite element analysis and wave models (spectral element models). From this model, the scattering coefficients of the discontinuity can be estimated.

4. **Modelling a beam with a notch or slot** In this chapter, two models of the damaged beam are presented. The well-known linear and elastic lumped spring model of a notch [4, 5] is reviewed and its scattering coefficients are calculated. The second model is a combined finite element and wave model used to model both a notch and slot. This model includes more detail of the shape of the damage and is compared to the lumped-spring model.

5. **Measuring the scattering coefficients** This chapter reviews the methods used for experimentally estimating scattering coefficients of discontinuities in beams and an experiment is described. The effects of experimental error on the accuracy of the measured scattering coefficients is discussed. As an example, the scattering coefficients were measured for various masses that were attached to the beam. The experimental results are then compared with numerical results that are estimated from combined finite and spectral element models of the masses.

6. **Measuring the scattering coefficients of slots** Narrow slots, with various depths,

were cut into a number of beams. The scattering coefficients of the slots were measured and the results are presented in this chapter. The results are compared to numerical estimates derived from combined finite and spectral element models of the slot. The results are used to show how the measured reflection coefficient can be used as evidence that damage exists and for estimating the slot depth.

7. **Estimating slot depth** Given the numerical and experimental results of chapters 4 and 6, respectively, this chapter compares the two for estimating the slot depth from the measured reflection coefficients. A reference data set is generated using numerical models of the slot, to which experimental results are compared, in order to estimate the depth.

8. **Locating slot from the reflection coefficients** It is shown here that the location of a slot can be estimated by applying an inverse Fourier transform, in the wavenumber domain, to the measured reflection coefficients. Experimental results are given and the method is also used to locate more than one slot in the beam.

9. **Locating slots using phase information** It is shown in this chapter that an inverse Fourier transform in the wavenumber domain can be used to locate a slot from measurements of the phase of the point frequency response function.

10. **Discussion and suggestions for further work** This chapter summarises the main findings of the thesis and considers further work that might improve the method.

1.4. Contributions of the thesis

In the first half of this thesis, a method is considered that can be used to estimate the scattering coefficients of a discontinuity in a beam. The method follows previous work

by Doyle [6] and combines finite element models and wave models (spectral element models). The contribution of this part of the thesis lies in the application of the combined finite element and wave models to estimating the scattering coefficients of a discontinuity, in general, and more specifically notches and slots. The combined finite element and wave model is used to illustrate how the estimates of the scattering coefficients are affected by changes to the shape of the damage (e.g., width) and the existence of wave mode conversion. Comparing the results of the numerical damage models to conventional analytical models, provides some validation of the analytical models as well as suggesting their limitations.

The second half of this thesis concentrates on damage detection and estimation of the depth and location of a slot in the beam. Experimental results are presented to show the wave scattering coefficients of various sized slots. The main contribution here lies in the use of the measured scattering coefficients for assessing the damage. Methods are given for estimating the slot depth and location from the measured reflection coefficients.

Finally, a second method is described that shows how the location of the slot can be estimated from measurements of the phase of the point FRF.

In summary, the contributions of this thesis are:

- application of combined finite element and spectral element methods to estimating scattering coefficients of discontinuities, with specific application to notches and slots;
- numerical and experimental investigation of the wave scattering properties of slots in beams; and
- development of methods that can be used to estimate the depth and location of a slot, from measurements of the wavefield.

2. Vibration-based damage detection

2.1. Introduction

The term vibration-based damage detection (VBDD) refers specifically to methods used for SHM that rely on measurements of the dynamic response of a structure and use vibro-acoustic features for damage detection.

Over the last 25 years, there has been growing interest in VBDD and the amount of research has been on the increase [7]. High frequency methods such as ultrasonics have been used for many years in industrial applications. In the recent past, there has been much research activity concentrated on low frequency methods. These are attractive as they offer the possibility of sensing damage using measurements made remote from the damage site. In this chapter, an overview of the research in this area is given. In particular, this focusses on the detection and assessment of cracks in homogeneous isotropic beams.

2.2. Characterising damage

Damage causes changes in the properties of a structure. These changes can be characterised in different ways, and models of the damage can be developed. Damage is often characterised as a [7–9]:

- localised change in structural flexibility (increased flexibility);
- localised change in mass; and

- localised change in damping (increased damping).

Furthermore, damage may also cause a noticeably non-linear response.

A localised change in flexibility occurs when a crack is formed and elastic energy stored in the beam is released. The change can be related to the strain energy release rate [10] and the stress intensity factor [11]. These concepts are explained further in chapter 4.

Changes in mass may occur if the damage is severe, causing part of the structure to break off. This type of effect may be seen in composite materials in which layers of the composite may spall away. One may also find it in other materials, such as concrete structures that have been damaged or metal structures as a result of corrosion.

Localised changes in damping occur owing to dissipative mechanisms at the damage site (e.g., thermoelastic behaviour and friction) but such changes are difficult to measure in practice. VBDD using changes to modal damping parameters have been considered in [8].

In general, cracks behave non-linearly and in some cases, the non-linear behaviour can provide a useful feature from which the crack can be detected [9, 12, 13].

2.2.1. Modelling damage in beams

Modelling a damaged structure has a number of uses. Estimates from a model might be compared with experimental results and used to estimate parameters of the damage, e.g., its size. Furthermore, the model might be used to estimate how sensitive a particular feature is to damage and hence predict how useful that feature might be for damage detection.

A number of damage models can be found in the literature, although some are adopted

more than others. The behaviour of damage at low frequencies is often modelled as a change in the stiffness local to the damage site. For convenience, often the non-linear response is not included in the model and it is assumed that, at low frequencies, changes in the damping and mass are not significant in comparison to the change in stiffness [7].

One fracture model that has been used in various references is the lumped-spring model (sometimes referred to as the spring-hinge model) and this is considered in more detail in chapter 4. This model relates the changes in the local strain energy at notch shaped fracture to the stiffness of a spring for a given fracture mode [4, 5]. At low frequencies, one might assume that only the opening mode is significant, as in [4, 5, 14–17].

Although the lumped-spring model is used often in the literature, a number of other analytical models exist. For example, in [18], the rigidity of the beam is calculated over its length. The damage causes a reduction in this rigidity which depends on its type and size. A more qualitative approach can also be used to simulate damage, in which the elastic modulus of the structure is reduced at the damage site in proportion to its size [19, 20].

Conventional analytical models often assume a particular type of damage. The lumped-spring models are derived from analysis of a the static behaviour of a notch in a beam under a load. In this case, it is assumed that the notch is always open and, as such, the change in stiffness is assumed to be constant over time and frequency. This model is considered to be most accurate at low frequencies [7].

Were the notch subjected to an oscillating load, it will open and close [21]; this is referred to as breathing. Neglecting any non-linear behaviour that can ensue (such as friction or contact between the notch faces), the dynamic behaviour of a breathing notch

is time dependent. The time dependence might be included in the model as in [21], where the equivalent stiffness is allowed to vary with time. In [21] and [14], examples of the differences between the breathing and open notch models are presented. As these references consider changes in the modal parameters, the effects of a breathing notch depend on the location of the notch.

Numerical models offer the advantage of modelling the damage in more detail. For example, in [22, 23] and [24] the finite element and boundary element methods are used, respectively, to model the shape of a notch and to estimate its dynamic properties. These models offer a more detailed analysis of the dynamic behaviour and may provide a more accurate analysis of the dynamic response, in comparison to the lumped-spring model.

2.3. Linear vibration-based damage detection

In this section, some methods for VBDD are reviewed. An overview of each method is given, concentrating on the underlying principles.

2.3.1. Modal methods

The dynamic response of a structure can be described by its mode shapes and natural frequencies. For discrete multiple degree-of-freedom systems, both parameters can be determined from the well-known eigenvalue problem [25], which for undamped linear free vibration is

$$\left(\mathbf{K} - \omega^2 \mathbf{M}\right)\boldsymbol{\phi} = \mathbf{0} \tag{2.1}$$

where $\mathbf{K}$ is the stiffness matrix, $\mathbf{M}$ is the mass matrix, $\omega = 2\pi f$, f is the frequency and $\boldsymbol{\phi}$ is a vector of degrees of freedom. The mode shapes are the eigenvectors of Eq. 2.1 and the natural frequencies are predicted from the eigenvalues.

Damage to the structure is assumed to alter the stiffness matrix, such that

$$\left(\tilde{\mathbf{K}} - \omega^2\mathbf{M}\right)\boldsymbol{\phi} = \mathbf{0} \tag{2.2}$$

where $\tilde{\mathbf{K}} = \mathbf{K} - \Delta\mathbf{K}$ and $\Delta\mathbf{K}$ is the change in stiffness at the damage site. The eigenvalues and eigenvectors of Eq. 2.2 differ from those in Eq. 2.1 and it is this feature that is exploited by modal damage detection methods.

For example, as explained in [19], the change in the jth natural frequency, $\Delta\omega_j$, between the undamaged and damaged structures is a function of the change in stiffness and the location, otherwise written as

$$\Delta\omega_j = g_j(\Delta\mathbf{K}, \mathbf{r}) \tag{2.3}$$

where $\mathbf{r}$ is a general location vector and g is a function. This suggests that by measuring a change in natural frequency, it may be possible to locate the damage. Also, the change in natural frequency is a function of $\Delta\mathbf{K}$, which itself is a function of the size of the damage.

To detect damage, the results must be compared to either a model of the undamaged structure or a model of the damaged structure. These models may be analytical, numerical or based on experimental testing. By comparing measurements made on a damaged structure to the undamaged model, it may be possible to note changes in the modal parameters that may signify damage, as in [19]. If one wanted to estimate the size of the damage, it would be necessary to model the effect of damage and compare this to experimental results, as in [4].

Typically, only the first few modes are considered for damage detection. In [4], the mode shapes and natural frequencies are calculated for a cantilever Euler-Bernoulli beam with a single transverse notch, modelled as a rotational spring. Similar studies have

considered double-sided notch [5], multiple notch [26] and notch in stepped beams [27]. In other studies, the curvature mode shapes have been considered and it is suggested that they are more sensitive to damage than the displacement mode shapes [2,28].

Experimental results, such as those given by [4], show how the lumped spring model can be used to predict the location and extent of a notch in a beam. However, when using modal parameters, the accuracy of the damage detection depends on its location. For beams in bending, the sensitivity of the modal features depends on the curvature of the beam, i.e., changes in strain energy. Therefore, if damage occurs where the curvature is large, the effect of the damage is large; while, if the damage occurs where the curvature is small, the effect is small. The chances of a damage occurring where the curvature is large are improved if higher frequency modes are considered but this is often impractical due to the number of sensors and measurements required.

In the lowest modes, the modal features tend to be insensitive to small damage [4,7]. This might be improved by measuring higher frequency modes but, again, this solution is often impractical.

Given that the lower modes are insensitive to small damage, the changes in the modal parameters may not exclusively be a result of damage. Temperature variation or other environmental effects may alter the modal parameters, as might small changes in the boundary conditions.

To summarise, the advantages and limitations of modal methods for VBDD are as follows:

- **Advantages**
  - Damage can be detected from measurements made at locations away from the damage site.
  - Modelling methods available for complicated structures.
  - Experimental and numerical methods well understood.
  - Can be less costly than other NDT methods.
- **Limitations**
  - Features are insensitive to small damage.
  - Ability to detect damage can depend on the location of the damage.
  - Practical issues often constrain the analysis to the first few modes.
  - Method requires either data describing the undamaged structure and/or models of the damaged structure.

2.3.2. Frequency response methods

A frequency response function (FRF) describes a ratio between two quantities in the frequency domain, e.g., a ratio between the response and the excitation force (receptance, mobility and accelerance), a ratio between responses at different locations or a ratio between two forces (transmissibility).

FRFs include magnitude and phase information about the structural response. When damage occurs in the structure the FRF is affected and, as with modal methods, the

effects are dependent upon the location of the excitation, the location of the damage and also on the extent of the damage.

The most significant effects of damage on the FRF occur at the resonances and anti-resonances. Other effects can be seen in the phase. This is shown in [20], in which a number of FRFs are predicted from numerical models and are used to simulate damage detection on a bridge/truss-like structure. This approach compares the changes between the damaged and undamaged structures to locate damage and similar methods were used in [29,30].

As with the modal methods, FRF methods often require either a model of the undamaged structure or a model of the damaged structure. This means that the plant response of the structure must be estimated either by numerical or experimental means.

Damage can also create new resonances in the FRF and this has been used as a feature for damage detection in [31]. New resonances and anti-resonances are created when waves scatter between the damage and the ends of the beam. At certain frequencies, the scattered waves interfere constructively to give a new peak in the FRF or destructively to create a new trough.

When waves are scattered by damage, some of the energy is reflected and some is transmitted. As a consequence, damage can cause small changes in the magnitude of the peaks in the FRF. This was suggested in [32] as a possible feature for damage detection.

In [29,33,34] the changes seen in the anti-resonances were considered as a feature for damage detection. In [29] the anti-resonances of the damaged and undamaged structures were compared and used to estimate the location of the damage. The method was also applied to beams with multiple notches in [33] and, although the numerical simulations described in [33] show that both notches can be located, the experimental results are not

as conclusive. Some reservations about this method are put forward by [34], in reference to the practicality of accurately measuring the anti-resonances. Anti-resonances are affected by environmental conditions and changes in the boundary conditions that might occur in practice but an additional problem is noise. Often, when measuring an FRF such as the mobility, one can expect the coherence between the response and excitation to be much less than unity at the anti-resonances, which primarily is a result of a poor signal-to-noise ratio. The accuracy of this result is then brought into question and one asks: how much of the measurement is the signal and how much is noise? This has repercussions for repeatability and consistency in the accuracy of the method.

To summarize the use of FRF methods for VBDD:

- **Advantages**
  - Single measurements can cover a larger frequency ranges than modal methods.
  - Possibility of remote damage detection.
  - Experimental and numerical methods are well established.
- **Limitations**
  - Features are insensitive to small damage at low frequency.
  - Ability to detect damage can depend on its location.
  - Method requires either data describing the undamaged structure or models of the damaged structure.

2.3.3. Wave analysis

The motion of a structure can be described in terms of the wavefield, and a discontinuity, such as damage, described in terms of its scattering properties. The use of the wave method for VBDD is the particular focus of this thesis and more detail is given in chapter 3. Wave methods in VBDD have mostly been considered for very high frequency behaviour and these are discussed in the next subsection.

Wave methods have been employed to produce models of damaged beams for predicting, for example, the frequency response [15] or the response in time domain [35, 36]. In these studies, the wave method has been used specifically for the model, while the wave parameters, such as the scattering coefficients of the damage, have not been considered as features for damage detection.

In [15] and [37] the axial and flexural scattering coefficients of a notch in a beam were derived, respectively, using the lumped-spring notch model. This analysis showed that the scattering coefficients of the lumped-spring depend on frequency and the stiffness of the spring (i.e., the notch depth). Therefore, it may be possible that the scattering coefficients can be used as a feature for damage detection, as suggested in [37], and this is considered in more detail in Chapter 4.

In [38] the wave scattering coefficients of a beam with inhomogeneities and delamination were estimated from analytical wave models. Again, analytical results showed how the scattering coefficients depend on the size of the inhomogeneity and on frequency.

2.3.4. Very high frequency wave methods

Very high frequency wave methods, such as ultrasonic and surface wave methods, are well established and used frequently in industrial applications [1,39]. For these methods the wavelength is much shorter than the dimensions of the structure.

Acoustic emission (AE) analysis [1] is based on the measurement of lamb waves that propagate through the structure. AEs are stress waves created by damage as it occurs and may emanate from the damage when a load is applied to the structure. AEs are not repeatable, thus the structure must be continuously monitored. The main advantage of AE analysis is that it can be used to detect small scale damage. One of the disadvantages lies in the reproducibility of the AEs, thus requiring the structure to be monitored continuously.

Guided waves (or Lamb waves) are very sensitive to small defects. The waves propagate through the thickness of the structure as wave modes [40] and these waves scatter at any discontinuities. There are an infinite number of wave modes but they propagate only when the excitation frequency is above the cut-on frequency of the wave mode. In guided wave methods, the aim is to excite the wave modes and measure their existence at some point remote from the damage site. This might be achieved due to intentional external excitation but can also occur when the structure becomes damaged, e.g., when a crack grows.

Given that Lamb waves are typically of very short wavelength and propagate through the thickness of, for example, a plate or beam, the use of such methods offer the possibility of detecting small surface and internal defects [41]. Such methods have been considered for isotropic and composite structures [39,41–43].

There are various difficulties in using Lamb waves for damage detection. Firstly, at a

given frequency, a number of wave modes may contribute to the signal. Given that each wave mode propagates at a different velocity, having many wave modes can make it more difficult to determine specific reflections from damage sites [41]. Another major issue lies with signal to noise problems that can arise due to attenuation and dispersion. For these reasons, a particular excitation frequency band is chosen to minimise the effects of dispersion, i.e., a band in which the group velocity varies by only a small amount. In particular, attenuation and dispersion limit the distance over which a particular wave can be detected, although the maximum distance can be in the region of a few meters, depending on the structure [42].

Ultrasonic methods, such as C-scan methods, are well-established in commercial applications [1]. A number of standard texts can be found on the subject, for example [44]. The structure is excited by an ultrasonic pulse and the scattered pulse is then measured at some time later. Using this method, one can build up an image of the damaged area. In contrast to Lamb wave methods and AE analysis, ultrasonic scattering methods do not rely on exciting wave modes that propagate within the structure. Instead, damage is detected through measurement of very high frequency wave reflections from defects and other discontinuities within a localised area. The need to perform many tests at many points along a structure is seen as one of the main deficiencies of such methods for practical SHM.

2.3.5. Time domain methods

It may be possible to detect damage from measurements of the scattered waves. For example, a pulse is sent through a structure, is scattered and then returns to the excitation point some time later. If the wave speed is known and is also constant with frequency, the time delay between sending and receiving the pulse can be used to estimate the

location of the scatterer. This approach is used in pulse-echo ultrasonics and is considered for lower frequency applications in [35, 36].

In dispersive systems, different frequencies travel at different speeds. Dispersion makes it difficult to differentiate between the waves that scatter from the damage and waves that scatter from other discontinuities, as explained in [35, 36].

Other ways of looking at time-domain measurements in dispersive media, such as time-frequency or wavelet processing techniques may enable more information to be extracted. There has also been some interest shown in the possibility of using time-reversal methods in SHM. For example, in [45] time-reversal techniques were applied to lamb wave propagation to detect experimentally where masses were attached to a plate. Similarly, in [46], numerical simulations show how damage in a plate can be located by time-reversal methods.

2.4. Processing of data from damage structures

In vibration engineering, time data is often processed and converted to the frequency domain, the purpose of which is to show more information about the physical make-up of the signal. Similarly, in VBDD there are many different methods used to process damage detection features in order to learn more about the features and perhaps enhance them. Many of these methods seek to quantify a chosen feature and this may lead to the estimation of the damage parameters such as location and extent.

In vibration, the data that is processed is often recorded in the frequency, time or modal domain. It should be remembered that the ability to detect damage from a given feature is more a question of choosing a suitable feature than it is of choosing a suitable processing method. In other words, if the chosen feature is insensitive to damage, it is

unlikely that processing that same feature will improve the ability to detect the damage.

The main concern of this thesis is the use of waves for VBDD and not signal processing. Therefore, in this section, a brief overview of some of the processing methods in the literature is given but it is by no means exhaustive. The reader is directed to [1] and [47] for further examples, explanation and references.

2.4.1. Non-stationary signal processing

Non-stationary signal processing includes a range of processing methods that are used to process signals that are time-variant. In the literature there are a number of papers that consider the use of the wavelet transform for VBDD. As explained in [48], the variation of wavelet parameters, such as the scale, can be related to the location and extent of the damage. In [49], the spatial wavelet transform is implemented on mode shape data for a cracked beam and is used to locate local perturbations in the mode shape that may signify the existence of a crack.

One of the benefits of time-variant or time-frequency analysis methods is the ability to capture and track changes in the structural parameters and this can be particularly useful in SHM.

2.4.2. Statistical methods

Statistical methods are used to look for underlying statistical trends or anomalies in the measured data which can make the existence of damage become clearer. A number of examples are given in [1], such as outlier analysis [50] and principle component analysis. These two methods, for example, have been used to signify the existence of damage. By quantifying the anomalies in the statistical analyses, it is possible to set-up threshold levels that can be used to warn of damage in the structure.

In [51], kurtosis is used to predict the existence of abrupt changes in the signal that may be caused by a crack. The kurtosis can be used to signify the existence of the crack and, through multiple measurements, it was shown in [51] that a notch can be located and its depth estimated.

2.4.3. Pattern recognition

Damage detection can be considered as a pattern recognition problem. When damage occurs it causes changes to a number of features. By considering how the features change and recognising the pattern of the changes, it may be possible to detect the damage.

A description of pattern recognition using artificial neural networks for VBDD is given in [1] and in [3]. Briefly, the neural network is trained using various input and output variables for many different damage scenarios . In an experiment, the input and output variables are measured and the network used to predict the scenario that best fits the measured data. The accuracy of this method depends on the quality of the training data, which is often numerical.

2.5. Summary

In this chapter, an overview of the methods used for vibration-based damage detection has been given. Importantly, the damage causes changes in a number of features. There has been a substantial amount of research into how damage affects modal parameters and the frequency response.

Low frequency methods of VBDD are advantageous because they can be used to detect damage at locations remote from the damage site but they are limited by not being sensitive to small scale damage. Very high frequency methods are more sensitive to

damage but can not always be used for remote damage detection, particularly if the waves are localised or attenuation is an issue.

This thesis explores the use of wave methods in a frequency range that falls between the low frequency modal methods and the very high frequency wave methods. With this approach it may be possible detect damage remote from the damage site whilst obtaining information about the damage from the scattering coefficients.

3. Modelling wave scattering from discontinuities

3.1. Introduction

It is proposed that the wave scattering coefficients of a crack depend on parameters such as the crack depth. Therefore, by measuring the scattering coefficients of the crack, it may be possible to estimate the crack depth. To do this requires a model to which experimental results can be compared.

Here, analytical and numerical models of a discontinuity are described, from which the scattering coefficients can be estimated. In this chapter, the models are described in general, for any discontinuity, whereas the specific case of a crack is considered in chapter 4.

When the dynamic properties, e.g., the equilibrium and compatibility conditions, of a discontinuity can be described analytically, the wave scattering coefficients can be estimated using the wave method, and this is reviewed here. However, for a general case, the dynamic properties of the discontinuity are not known analytically.

When an analytical model is not available, the discontinuity can be modelled numerically and its dynamic properties estimated using finite element (FE) analysis. However, estimating the scattering coefficients of the discontinuity directly from the FE model is not straightforward, least of all because the model is finite and waves reflect at the ends.

It would be easier to estimate the scattering coefficients of the discontinuity if the model were infinite, i.e., without the reflections from the ends of the model. Such a

model is developed here using the methods previously described by Doyle *et al.* [6, 22], in which models of structures were developed by combining FE and spectral element (SE) models. Taking a FE model of a portion of the beam that contains the discontinuity, semi-infinite boundary conditions can be imposed at both ends using the SE method. This step effectively removes the reflections from the ends of the FE region. Here, a method is described that can be used to estimate the scattering coefficients of the discontinuity from the assembled FE and SE model. A number of issues surround the assembly of the two models, which are addressed in due course.

The motivation for producing this model lies in the fact that, although analytical models of a cracks exist, they do not account for the exact shape of the crack or dynamic behaviour such as wave mode conversion at the crack. Therefore, the FE model may provide a more detailed model to compare with experimental results and also suggest the accuracy and limitations of the conventional analytical crack models (this is considered further in chapter 4).

3.2. Wave propagation in rods and beams

The vibration of any structure can be described in terms of a wave field. Waves transport energy through the structure and at a given frequency each wave type is characterised by a wavenumber [52]. In this thesis, the wave method is used to model the behaviour of beams with discontinuities and, in particular, cracks. In this section the wave method is reviewed.

Throughout, it is assumed that the vibration of the structure is linear and time-harmonic. In this case, the deformation of a one-dimensional structure, such as a

beam, can be described in the frequency domain by

$$\phi(x, \omega) = \mathbf{\Phi}(x, \omega)\mathbf{a}(\omega) \tag{3.1}$$

where ϕ is the deformation, the $\mathbf{\Phi} = \{\Phi_1, \Phi_2, \cdots, \Phi_N\}$ is a row vector of N wave functions that are evaluated at location x, $\mathbf{a} = \{a_1, a_2 \ldots, a_N\}^T$ is a column vector of corresponding wave amplitudes, T is the transpose operator, $\omega = 2\pi f$ and f is the frequency.

The response in the time-domain is obtained by applying the principle of superposition and summing the waves over all frequencies, so that

$$\phi(x, t) = \int_{-\infty}^{+\infty} \mathbf{\Phi}(\mathbf{x}, \omega)\mathbf{a}(\omega)\ e^{i\omega t} d\omega \tag{3.2}$$

which can be seen as the inverse Fourier transform (IFT) of the wave functions. Although the wave functions are complex, the time domain response is real.

The wavefields in a uniform rod or beam are described by an equation of motion. Rod theory is said to describe the axial wave motion and a beam theory describes the flexural motion.

Here, the longitudinal and Love rod theories and Euler-Bernoulli and Timoshenko beam theories will be briefly reviewed and more detail can be found in [52]. Each rod/beam is described without including damping, though structural damping can be included using a complex modulus of elasticity $E(1 + i\eta)$, where E is the Young's modulus and η is the damping loss factor.

3.2.1. Longitudinal rod theory

Longitudinal rod theory (LRT) assumes that the cross-section remains plane under axial stress, such that the stress distribution remains constant over the area of the cross-section and shear stresses are negligible. These assumptions are most accurate for small

displacements and when the wavelength is much longer than the dimensions of the cross-section. If the rod is uniform, the equation of motion is [52]

$$EA\frac{\partial^2 u}{\partial x^2} - \rho A\frac{\partial^2 u}{\partial t^2} = C \tag{3.3}$$

where ρ is the material density, u is the axial displacement, A is the area of the cross-section and C is the applied axial force per unit length. The sign convention is illustrated in Fig. 3.1 and the internal axial force is

$$F = EA\frac{\partial u}{\partial x} \tag{3.4}$$

The general solution of Eq. 3.3, for free vibration ($C = 0$), is found by assuming that the displacement is defined by a wave function, such that $u(x, \omega) = a\Phi(x)e^{i\omega t}$, where a is the wave amplitude. Substituting this into Eq. 3.3 and omitting the time dependence $e^{i\omega t}$, the general solution can be shown to be

$$u(x, \omega) = a_+^A e^{-ik_0 x} + a_-^A e^{ik_0 x} \tag{3.5}$$

where $k_0 = \omega\sqrt{\rho/E}$ is the longitudinal wave number, $a_{+,-}$ denotes the amplitude of a propagating forward-going or backward-going wave and the superscript A indicates an axial wave.

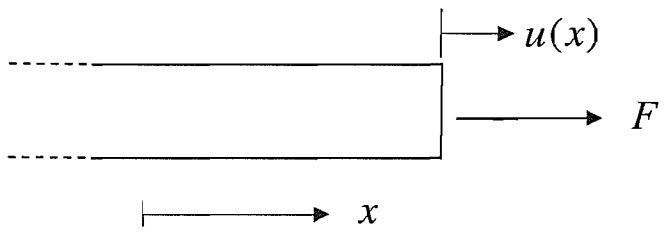

Fig. 3.1: Sign convention for axial motion and forces.

3.2.2. Love rod theory

Love rod theory (LVRT) [52] is more accurate than LRT as it includes Poisson contraction. However, it remains a plane-stress model and does not account for contraction out of plane or any changes to the stress distribution caused by the changed shape of the cross-section.

For uniaxial stress σ_{xx}, the strains are related by $\epsilon_{yy} = -\upsilon\epsilon_{xx}$, where υ is Poisson's ratio and ϵ_{xx} and ϵ_{yy} are the normal strains in the x and y directions, respectively. Neglecting shear strains, the contraction in the y-direction is [52]

$$v = y\epsilon_{yy} = -y\upsilon\frac{\partial u}{\partial x} \tag{3.6}$$

Graff [52] shows how Eq. 3.6 is used to derive the equation of motion, which is

$$EA\frac{\partial^2 u}{\partial x^2} + \upsilon^2\rho I\frac{\partial^4 u}{\partial x^2\partial t^2} - \rho A\frac{\partial^2 u}{\partial t^2} = C \tag{3.7}$$

where I is the second moment of area of the cross-section. The internal force F_L is given as

$$F_L = EA\frac{\partial u}{\partial x} + \rho I\upsilon^2\frac{\partial}{\partial x}\left(\frac{\partial^2 u}{\partial t^2}\right) \tag{3.8}$$

The general solution for free vibration is found in the same way as LRT. Omitting the time dependence $e^{i\omega t}$, then

$$u(x,\omega) = a_+^A e^{-ik_L x} + a_-^A e^{ik_L x} \tag{3.9}$$

where $k_L = \sqrt{k_0^2/(1-[\upsilon k_0 g]^2)}$ is the Love wavenumber and $g = \sqrt{I/A}$ is the radius of gyration. LVRT differs from LRT by including the kinetic energy associated with in-plane Poisson contraction. This results in a fourth order differential term in the equation of motion, the importance of which depends on the radius of gyration. At long wavelengths ($\upsilon k_0 g << 1$), the contraction is negligible and the general solution and wavenumber are similar to LRT.

3.2.3. Euler-Bernoulli beam theory

Euler-Bernoulli beam theory (EBT) describes a beam in flexure, where wavelengths are much longer than the dimensions of the cross-section. As the beam bends, the cross-section displaces transversely by $v(x, t)$ and rotates through the angle ψ. EBT assumes that shear deformation and rotational inertia are negligible and, for small rotations, $\psi = \partial v/\partial x$. The equation of motion is [52]

$$EI\frac{\partial^4 v}{\partial x^2} + \rho A\frac{\partial^2 v}{\partial t^2} = P \tag{3.10}$$

where P is the applied transverse force per unit length. The bending moment M and shear force Q are

$$Q(x,t) = -\frac{\partial M}{\partial x} \;\; ; \quad M(x,t) = EI\frac{\partial^2 v}{\partial x^2} \tag{3.11}$$

Fig. 3.2 shows the sign conventions adopted here for a beam.

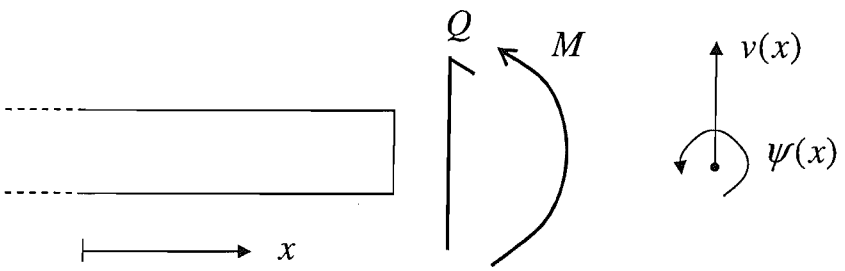

Fig. 3.2: Sign conventions for a beam in flexure.

The solution for free vibration ($P = 0$) is sought by substituting $v(x) = a\Phi(x)e^{i\omega t}$ into Eq. 3.10. Omitting the time dependence, the general solution can be shown to be

$$v(x,\omega) = a_+^P e^{-ik_b x} + a_+^N e^{-k_b x} + a_-^P e^{ik_b x} + a_-^N e^{k_b x} \tag{3.12}$$

where $k_b = \sqrt[4]{\omega^2 \rho A / EI}$ is the Euler-Bernoulli wavenumber and the superscripts P and N denote propagating flexural and nearfield waves, respectively. The nearfield waves decay exponentially with distance and do not radiate power to the farfield. Nearfield waves can not be neglected when considering the motion in close proximity to their source and they also play an important role when waves interact with discontinuities. When using Eq. 3.12, numerical problems can occur beacause $a_-^N e^{k_b x}$ increases exponentially with distance. This problem can be overcome by writing Eq. 3.12 as

$$v(x,\omega) = a_+^P e^{-ik_b x} + a_+^N e^{-k_b x} + \hat{a}_-^P e^{-ik_b(L-x)} + \hat{a}_-^N e^{-k_b(L-x)} \tag{3.13}$$

where L is the distance to some reference position on the beam and $\hat{a}_-^{P,N}$ are wave amplitudes that differ from Eq. 3.12 by a phase term.

3.2.4. Timoshenko beam theory

Timoshenko beam theory (TBT) [53] includes the effects of rotary inertia and shear deformation of the cross-section that are neglected in EBT. This theory is more accurate than EBT, particularly when the wavelength is not very long in comparison to the dimensions of the cross section. The governing equations are [52]

$$EI\frac{\partial^2 \psi}{\partial x^2} + GA\kappa\left(\frac{\partial v}{\partial x} - \psi\right) - \rho I\frac{\partial^2 \psi}{\partial t^2} = 0 \tag{3.14}$$

$$GA\kappa\left(\frac{\partial \psi}{\partial x} - \frac{\partial^2 v}{\partial x^2}\right) + \rho A\frac{\partial^2 v}{\partial t^2} = P(x,t) \tag{3.15}$$

where G is the shear modulus and κ is the Timoshenko shear coefficient. Eq. 3.14 relates the moments and angular acceleration, whereas Eq 3.15 relates transverse forces and lateral acceleration. Values of the Timoshenko shear coefficient for typical cross-sections can be found in [54]. All of the beam models in this thesis consider a rectangular

cross-section, therefore the shear coefficient used is

$$\kappa = \frac{10(1+\upsilon)}{12+11\upsilon} \tag{3.16}$$

The rotation of the cross-section ψ now includes the rotation due to bending and shear γ_{xy}. The shear stress is

$$\gamma_{xy} = \frac{\partial u}{\partial y} + \frac{\partial v}{\partial x} = \frac{\partial v}{\partial x} - \psi \tag{3.17}$$

and the internal shear force and bending moment are

$$Q = GA\kappa\left(\frac{\partial v}{\partial x} - \psi\right) = \rho I\frac{\partial^2\psi}{\partial t^2} - \frac{\partial M}{\partial x}\ ; \qquad M = EI\frac{\partial\psi}{\partial x} \tag{3.18}$$

EBT is obtained from TBT by assuming the shear angle is zero, differentiating Eq. 3.14 once with respect to x, summing the resulting equation with Eq. 3.15 and neglecting the rotary inertia term $\rho I\partial^2\psi/\partial t^2$.

Omitting the time dependence, the solution to the free vibration problem is sought by assuming that

$$v = ae^{-ikx}\ ; \qquad \psi = \Theta ae^{-ikx}; \tag{3.19}$$

where Θ is an amplitude ratio as yet undefined. It can be shown [52] that there are two general solutions for TBT, given by

$$v = a_+^P e^{-ik_t x} + a_+^N e^{-ik_n x} + a_-^P e^{ik_t x} + a_-^N e^{ik_n x} \tag{3.20}$$

$$\psi = \Theta_t a_+^P e^{-ik_t x} + \Theta_n a_+^N e^{-ik_n x} - \Theta_t a_-^P e^{ik_t x} - \Theta_n a_-^N e^{ik_n x} \tag{3.21}$$

where the Timoshenko wavenumbers are[1]

$$k_t = \frac{k_b}{\sqrt{2}}\sqrt{(\delta^2+\beta^2) + \sqrt{(\delta^2-\beta^2)^2+4}} \tag{3.22}$$

$$k_n = \frac{-k_b}{\sqrt{2}}\sqrt{(\delta^2+\beta^2) - \sqrt{(\delta^2-\beta^2)^2+4}} \tag{3.23}$$

[1]For the derivation, see Appendix § A.

and $\delta = k_0/k_b$ and $\beta = k_s/k_b$, where $k_s = \omega\sqrt{\rho/G\kappa}$ is the shear wavenumber. From Eq. 3.15 it follows that

$$\Theta_t = \frac{k_t^2 - k_s^2}{ik_t} \; ; \Theta_n = \frac{k_n^2 - k_s^2}{ik_n} \tag{3.24}$$

The wavenumber k_t is always real and positive, corresponding to a propagating wave. The wavenumber k_n is imaginary when $\delta\beta < 1$, corresponding to a nearfield wave. When $\delta\beta > 1$, k_n is real and represents a second propagating wave or *second spectrum* [55]. The frequency associated with $\delta\beta = 1$ is the Timoshenko cut-on frequency. Here, it is assumed that the excitation frequency is below this cut-on frequency and k_n is imaginary.

At low frequencies, the longitudinal and shear wavelengths are much longer than the flexural wavelength and as $\omega \to 0$.

$$k_t \approx \pm k_b \quad ; \quad k_n \approx \pm ik_b \tag{3.25}$$

Therefore, at low frequencies the Timoshenko wavenumbers approximate those of EBT.

3.3. Wave reflection and transmission

A structural discontinuity may be thought of as a change in impedance that is unaccounted for by the equation of motion. A discontinuity can be characterised by its wave reflection and transmission coefficients, which describe how incident waves are scattered [56]. The scattering coefficients may depend on frequency, incident wave type and, in a more general sense, they can also depend on the angle of incidence or energy dissipation at the discontinuity.

The wavefield of the beam illustrated in Fig. 3.3, comprises axial, flexural and

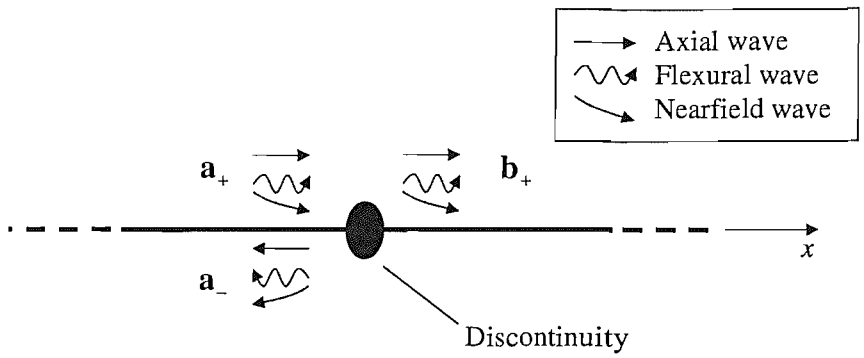

Fig. 3.3: A discontinuity in an infinite rod or beam.

nearfield waves. The wave reflection matrix **R** can be written

$$\mathbf{a}_- = \mathbf{R}\mathbf{a}_+ \;;\; \mathbf{R} = \begin{bmatrix} R^{AA} & R^{AP} & R^{AN} \\ R^{PA} & R^{PP} & R^{PN} \\ R^{NA} & R^{NP} & R^{NN} \end{bmatrix} \;;\; \mathbf{a}_- = \begin{Bmatrix} a_-^A \\ a_-^P \\ a_-^N \end{Bmatrix} \;;\; \mathbf{a}_+ = \begin{Bmatrix} a_+^A \\ a_+^P \\ a_+^N \end{Bmatrix} \tag{3.26}$$

and the transmission matrix **T** as

$$\mathbf{b}_+ = \mathbf{T}\mathbf{a}_+; \;\; \mathbf{T} = \begin{bmatrix} T^{AA} & T^{AP} & T^{AN} \\ T^{PA} & T^{PP} & T^{PN} \\ T^{NA} & T^{NP} & T^{NN} \end{bmatrix} \;;\; \mathbf{b}_+ = \begin{Bmatrix} b_+^A \\ b_+^P \\ b_+^N \end{Bmatrix} \tag{3.27}$$

where $\mathbf{a}_+$, $\mathbf{a}_-$ and $\mathbf{b}_+$ are vectors of incident, reflected and transmitted wave amplitudes and the superscript on each reflection and transmission coefficient denotes the type of the incident and scattered waves, e.g, R^{AP} is the reflection coefficient given an incident propagating flexural wave and a reflected axial wave, whereas R^{PA} is the opposite.

The terms along the diagonal of **R** or **T**, with the superscripts *AA*, *PP* and *NN*, describe scattered waves of the same type as those incident. When the off-diagonal coefficients are non-zero, energy from one wave type (or mode) is transferred to another; a phenomenon referred to as wave-mode conversion. The significance of wave-mode

conversion depends on the discontinuity. One example of such a discontinuity, of interest here, is a one-sided transverse crack.

3.3.1. Power reflection and transmission coefficients

Power scattering coefficients represent the proportions of energy that are reflected and transmitted. These coefficients offer a more physical interpretation of the size of the wave scattering. The power scattering coefficients are defined as

$$r^{ri} = \frac{p^r}{p^i} \; ; \quad t^{ti} = \frac{p^t}{p^i} \tag{3.28}$$

where i, r, and t denote incident, reflected and transmitted wave type, i.e., these are replaced by either A,P or N. Furthermore, p^i is the incident wave power, p^r is the reflected wave power and p^t is the transmitted wave power.

The wave amplitude scattering coefficients in Eq. 3.26 and 3.27 are converted to power scattering coefficients using Eq. 3.28 and the wave power for each wave type is given in Table A.1, which can be found in Appendix A.2.

For example, consider the coefficient R^{AP} where

$$a_-^A = R^{AP} a_+^P \tag{3.29}$$

From Table A.1 (see Appendix, § A.2), if LRT and EBT are used to describe the waves, the reflected wave power is

$$p^A = \frac{1}{2}\rho A c_0 \omega^2 |R^{AP}|^2 \, |a_+^P|^2 \tag{3.30}$$

and the incident wave power is

$$p^P = \rho A c_b \omega^2 |a_+^P|^2 \tag{3.31}$$

where c_0 and c_b are the phase velocities from LRT and EBT, respectively. Therefore, the power reflection coefficient r^{AP} is

$$r^{AP} = \frac{c_0}{2c_b}|R^{AP}|^2 \tag{3.32}$$

In all cases, the condition of conservation of energy should be met. Neglecting nearfield terms and in the case where the discontinuity is undamped, this implies that

$$r^{AA} + r^{AP} + t^{AA} + t^{AP} = 1 \tag{3.33}$$

$$r^{PP} + r^{PA} + t^{PP} + t^{PA} = 1 \tag{3.34}$$

3.4. Estimating scattering coefficients from an analytical model

The scattering coefficients of a discontinuity can be found analytically if its dynamic properties are known analytically. This method is explained in [56] and an example is presented here.

One advantage of an analytical solution is that it can offer an insight into the parameters that control the wave scattering. The main drawback of the method is that the dynamic characteristics of complex discontinuities are not readily described analytically.

3.4.1. Scattering of a point mass

To illustrate the analytical method, the scattering coefficients of a point mass are presented here. A point mass in a beam is illustrated in Fig. 3.4. The wavefield consists of incident, reflected and transmitted axial and flexural waves. There is no wave-mode conversion at the mass so the axial and flexural wave scattering can be treated separately.

For axial waves the compatibility and equilibrium conditions of the mass are

$$u_+ = u_- \;;\; F_+ - F_- = m\frac{\partial^2 u_+}{\partial t^2} \tag{3.35}$$

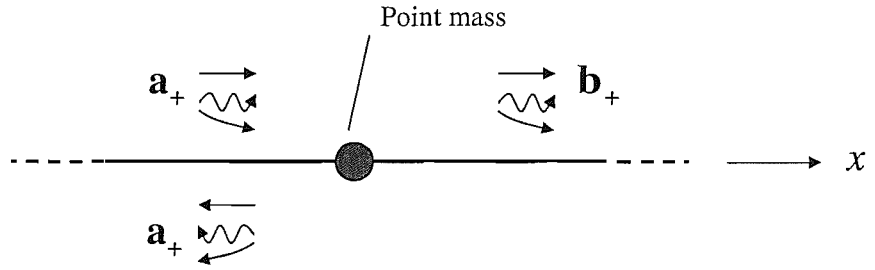

Fig. 3.4: Analytical model of a point mass in a beam.

where m is the mass and the subscripts + and – denote the right and left hand sides of the discontinuity, respectively.

Using LVRT (see § 3.2.2), Eqs. 3.7 and 3.8 can be used to show that

$$\begin{Bmatrix} 1 \\ 1 \end{Bmatrix} a_+^A = \begin{bmatrix} 1 & 1-\hat{m} \\ -1 & 1 \end{bmatrix} \begin{Bmatrix} a_-^A \\ b_+^A \end{Bmatrix} \tag{3.36}$$

where $\hat{m} = \omega^2 m/\{ik_L(EA - \omega^2\rho I\upsilon^2\}$. The reflection and transmission coefficients are found by inverting the matrix on the right-hand side of Eq. 3.36, such that

$$R^{AA} = \frac{a_-^A}{a_+^A} = \frac{\hat{m}}{2-\hat{m}} \;\; ; \;\; T^{AA} = \frac{b_+^A}{a_+^A} = \frac{2}{2-\hat{m}} \tag{3.37}$$

At low frequencies, $|R^{AA}| \rightarrow 0$ and $|T^{AA}| \rightarrow 1$ whilst at high frequencies (as long as $EA > \omega^2\rho I\upsilon^2$) $|R^{AA}| \rightarrow 1$ and $|T^{AA}| \rightarrow 0$.

For flexural waves, the compatibility and equilibrium conditions conditions of the mass are

$$v_+ = v_- \;\; ; \;\; \psi_+ = \psi_- \tag{3.38}$$

$$Q_+ - Q_- = m\frac{\partial^2 v_+}{\partial t^2} \;\; ; \;\; M_+ = M_- \tag{3.39}$$

Using TBT (see § 3.2.4), the compatibility and equilibrium conditions for the

displacement and the moment in Eqs. 3.38 and 3.39, can be used to show that

$$\mathbf{b}_+^P = \mathbf{a}_+^P + \mathbf{a}_-^P \tag{3.40}$$

where $\mathbf{b}_+^P = [b_+^P \; b_+^N]^T$, $\mathbf{a}_+^P = [a_+^P \; a_+^N]^T$ and $\mathbf{a}_-^P = [a_-^P \; a_-^N]^T$.

The compatibility and equilibrium conditions for the rotation and shear force, Eqs. 3.38 and 3.39, can be used to show that

$$\begin{bmatrix} \Theta_t & \Theta_n \\ d_t + m' & d_n + m' \end{bmatrix} \mathbf{b}_+^P = \begin{bmatrix} \Theta_t & \Theta_n \\ d_t & d_n \end{bmatrix} \mathbf{a}_+^P - \begin{bmatrix} \Theta_t & \Theta_n \\ d_t & d_n \end{bmatrix} \mathbf{a}_-^P \tag{3.41}$$

where $m' = \omega^2 m/EI$, $d_t = \Theta_t(k_t^2 - k_0^2)$ and $d_n = \Theta_n(k_n^2 - k_0^2)$, where $\Theta_{t,n}$ are given in Eq. 3.24.

Eq. 3.40 is used to find $\mathbf{a}_-^P$ in terms of $\mathbf{a}_+^P$ and $\mathbf{b}_+^P$ which is then substituted into Eq. 3.41 to find the transmission coefficients. A similar substitution is made to find the reflection coefficients and both sets of scattering coefficients are given as

$$\begin{bmatrix} R^{PP} & R^{PA} \\ R^{AP} & R^{AA} \end{bmatrix} = \frac{1}{\tau} \begin{bmatrix} m'\Theta_n & (2d_n + m')\Theta_n - 2d_n\Theta_n \\ 2d_t\Theta_t - (2d_t + m')\Theta_t & -m'\Theta_t \end{bmatrix} \tag{3.42}$$

$$\begin{bmatrix} T^{PP} & T^{PA} \\ T^{AP} & T^{AA} \end{bmatrix} = \frac{1}{\tau} \begin{bmatrix} (2d_n + m')\Theta_t - 2d_t\Theta_n & (2d_n + m')\Theta_n - 2d_n\Theta_n \\ 2d_t\Theta_t - (2d_t + m')\Theta_t & 2d_n\Theta_t - (2d_t + m')\Theta_n \end{bmatrix} \tag{3.43}$$

where $\tau = \Theta_t(2d_n + m') - \Theta_n(2d_t + m')$.

As an example, Fig. 3.5 shows the power scattering coefficients r^{AA}, t^{AA} r^{PP} and t^{PP} as functions of frequency. In this example, the beam model is mild steel with $E = 210 \times 10^9 \mathrm{Nm}^{-2}$, $\rho = 7850\mathrm{kgm}^{-3}$, $\upsilon = 0.3$, $b = 0.05\mathrm{m}$, $h = 0.006\mathrm{m}$ and the mass is $m = 0.5\mathrm{kg}$.

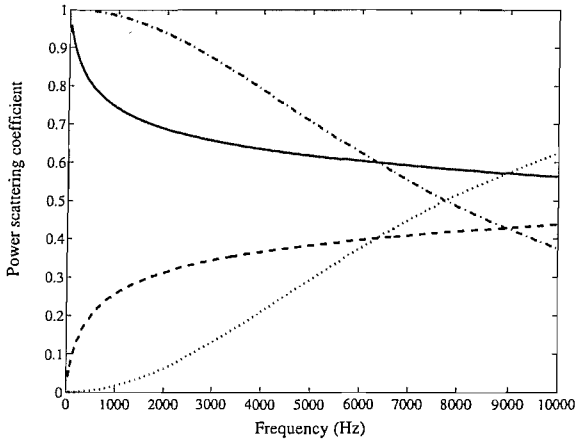

Fig. 3.5: Power scattering coefficients of a point mass with m = 0.5kg: (—), r^{PP}; (– –), t^{PP}; (· · ·), r^{AA}; (– · –), t^{AA}.

3.5. The spectral element method

3.5.1. Overview

Given the difficulties in producing analytical models of discontinuities with complex dynamic properties, over the next three sections a numerical model is considered. The numerical model is developed using the spectral element (SE) method. The SE method is described in detail in [6]. The SE method is a frequency domain approach and, conventionally, SEs are defined using wave analysis. Often, a SE is used to model part of a structure for which an equation of motion is known.

It was shown by Doyle [6] that a FE model can be assembled with SEs. Whereas in [6] the model was used to estimate the FRF and the response in the time-domain, here it is used only in the frequency domain to estimate the scattering coefficients of a discontinuity.

The dynamic properties of the discontinuity are estimated using FE analysis. To estimate the scattering coefficients from the FE model directly is not straightforward, given that the model is finite and waves reflect from both ends. However, assembling the

FE model with semi-infinite SEs effectively imposes semi-infinite boundary conditions at the ends of the model. This step makes estimating the scattering coefficients of the discontinuity more straightforward.

In this section, the SE method is reviewed and the sections that follow (§ 3.6 and § 3.7) consider the assembly of the FE and SE models and a method for estimating the scattering coefficients.

3.5.2. The dynamic stiffness relation

A SE is described by the dynamic stiffness relation

$$\mathbf{p} = \mathbf{D}\boldsymbol{\phi} \tag{3.44}$$

where $\mathbf{p}$ is a vector of nodal forces, $\boldsymbol{\phi}$ is a vector of nodal dofs and $\mathbf{D}$ is the dynamic stiffness matrix (DSM). An example of a SE is illustrated in Fig. 3.6.

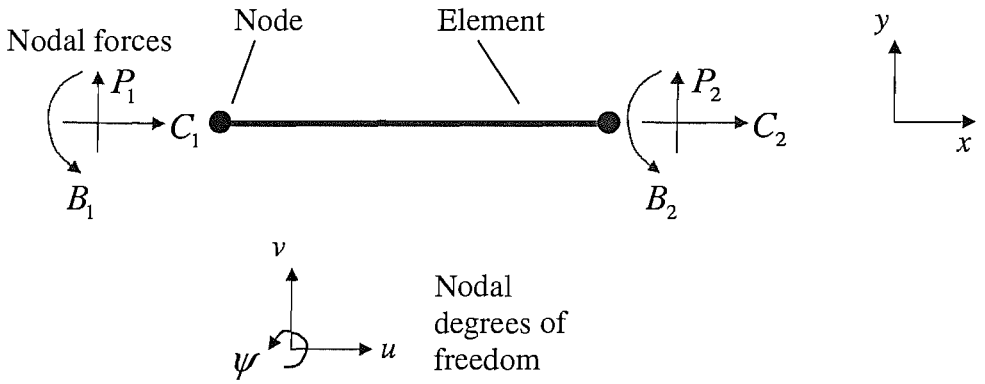

Fig. 3.6: A 1-D spectral element.

The nodal dofs and forces of a SE are described using wave analysis, such that

$$\boldsymbol{\phi} = \boldsymbol{\Psi}\mathbf{a} \;\; ; \;\; \mathbf{p} = \boldsymbol{\Gamma}\mathbf{a} \tag{3.45}$$

where $\boldsymbol{\Psi}$ and $\boldsymbol{\Gamma}$ are matrices of wave terms that depend on the equation of motion and $\mathbf{a} = \{\mathbf{a}_+ \; , \; \mathbf{a}_-\}^T$ is a vector of positive and negative-going wave amplitudes. From Eq. 3.45, the DSM is

$$\mathbf{D} = \boldsymbol{\Gamma}\boldsymbol{\Psi}^{-1} \tag{3.46}$$

3.5.3. Finite and semi-infinite spectral elements

A SE that can be used to describe the axial and flexural motion of a uniform rod or beam is illustrated in Fig 3.6. If the waves are described by LVRT and TBT (or LRT and EBT), each node has three dofs and three forces. The axial displacement and applied axial force are denoted by u and C, respectively. The transverse displacement and rotation are v and ψ, while the applied transverse force and moment are P and B, respectively. In Fig. 3.6, subscripts 1 and 2 are used to denote the node number. The derivations for rod and beam SEs are given in [6]. To illustrate the method, a finite rod SE and two semi-infinite beam SEs are derived in the following.

3.5.3.1. Finite rod

A finite rod SE has its first node at $x = 0$ and node two at $x = L$. Using LVRT (§3.2.2, Eq. 3.8 and Eq. 3.9), the nodal dofs and forces can be written

$$\begin{Bmatrix} u_1 \\ u_2 \end{Bmatrix} = \boldsymbol{\Psi} \begin{Bmatrix} a_+^A \\ a_-^A \end{Bmatrix} , \qquad \boldsymbol{\Psi} = \begin{bmatrix} 1 & 1 \\ e^{-ik_L L} & e^{ik_L L} \end{bmatrix} \tag{3.47}$$

$$\begin{Bmatrix} C_1 \\ C_2 \end{Bmatrix} = \boldsymbol{\Gamma} \begin{Bmatrix} a_+^A \\ a_-^A \end{Bmatrix} , \qquad \boldsymbol{\Gamma} = iEAk_L\left\{1 - (k_0 \upsilon g)^2\right\} \begin{bmatrix} 1 & -1 \\ -e^{-ik_L L} & e^{ik_L L} \end{bmatrix} \tag{3.48}$$

By Eq. 3.46, the DSM of the SE is

$$\mathbf{D} = \frac{EAk_L}{\sin(k_L L)}\left\{1-(k_0 \upsilon g)^2\right\}\begin{bmatrix} \cos(k_L L) & -1 \\ -1 & \cos(k_L L) \end{bmatrix} \tag{3.49}$$

3.5.3.2. Semi-infinite beam

Two semi-infinite beam SEs are illustrated in Fig. 3.7, where one extends to $+\infty$ and the other to $-\infty$. The equations of motion for each element, using TBT, are

$$v(x) = a_+^P e^{-ik_t x} + a_+^N e^{-ik_n x} \; ; \psi(x) = \; \Theta_t a_+^P e^{-ik_t x} + \Theta_n a_+^N e^{-ik_n x} \; ; \quad x \geq 0 \tag{3.50}$$

$$v(x) = a_-^P e^{-ik_t x} + a_-^N e^{-ik_n x} \; ; \psi(x) = -\Theta_t a_+^P e^{-ik_t x} - \Theta_n a_+^N e^{-ik_n x} \; ; \quad x \leq 0 \tag{3.51}$$

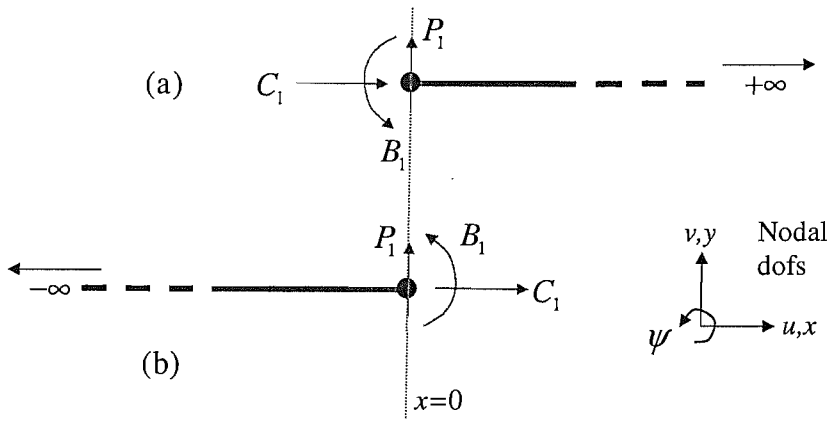

Fig. 3.7: Semi-infinite SEs.

Both elements in Fig. 3.7 are defined in a similar way. For the element that extends to $+\infty$, the nodal dofs and forces, using Eq. 3.45 and Eqs. 3.20 and 3.21, are

$$\boldsymbol{\phi}_+ = \boldsymbol{\Psi}_+ \mathbf{a}_+ \; ; \; \boldsymbol{\Psi}_+ = \begin{bmatrix} 1 & 1 \\ \Theta_t & \Theta_n \end{bmatrix} \; ; \; \boldsymbol{\phi}_+ = \begin{Bmatrix} v_1 \\ \psi_1 \end{Bmatrix}_+ \; ; \; \mathbf{a}_+ = \begin{Bmatrix} a_+^P \\ a_+^N \end{Bmatrix} \tag{3.52}$$

and

$$\mathbf{p}_+ = \mathbf{\Gamma}_+\mathbf{a}_+ \;;\; \mathbf{\Gamma}_+ = EI\begin{bmatrix} \left(k_0^2 - k_t^2\right)\Theta_t & \left(k_0^2 - k_n^2\right)\Theta_n \\ ik_t\Theta_t & ik_n\Theta_n \end{bmatrix} \;;\; \mathbf{p}_+ = \begin{Bmatrix} P_1 \\ B_1 \end{Bmatrix}_+ \tag{3.53}$$

where the subscript + denotes that the element extends to $+\infty$. The DSM for this element is

$$\mathbf{D}_+ = \mathbf{\Gamma}_+\mathbf{\Psi}_+^{-1} = \left(\frac{\Theta_t\Theta_n}{\Theta_n - \Theta_t}\right)EI\begin{bmatrix} (k_n^2 - k_t^2) & (k_0^2 - k_n^2)/\Theta_n - (k_0^2 - k_n^2)/\Theta_t \\ i(k_t - k_n) & (k_n^2 - k_t^2)/\Theta_t\Theta_n \end{bmatrix} \tag{3.54}$$

By a similar approach, the DSM for the element that extends to $-\infty$, denoted by the subscript $-$, can be shown to be

$$\mathbf{D}_- = \mathbf{\Gamma}_-\mathbf{\Psi}_-^{-1} = \left(\frac{\Theta_t\Theta_n}{\Theta_n - \Theta_t}\right)EI\begin{bmatrix} (k_n^2 - k_t^2) & -(k_0^2 - k_n^2)/\Theta_n + (k_0^2 - k_t^2)/\Theta_t \\ -i(k_t - k_n) & (k_n^2 - k_t^2)/\Theta_t\Theta_n \end{bmatrix} \tag{3.55}$$

Furthermore, by adding $\mathbf{D}_+$ and $\mathbf{D}_-$, the resulting DSM is that of an infinite Timoshenko beam.

3.6. Assembling FE and SE models

In this section, the assembly of FE and SE models is reviewed. The elements are assembled much like FEs are in FE analysis. One of the main issues of concern here, however, is the fact that the FE and SE models are not compatible, in general. Therefore an approximate method is used to enforce compatibility and connect the elements together.

3.6.1. The finite element method

The FE method is a well established tool for estimating structural vibration [57]. A structure is modelled using a number of discrete elements for which the deformation is

defined by shape functions. The number and type of elements required in a FE model depends on the complexity of the structure and the frequency range of interest. More elements are needed when the wavelength becomes short. The main advantage of the FE method is that it can be used to model structures with irregular geometries. Importantly, the FE method can be used to estimate the DSM of an arbitrary discontinuity.

The DSM of an FE model without damping is

$$\mathbf{D} = \mathbf{K} - \omega^2\mathbf{M} \tag{3.56}$$

where $\mathbf{K}$ and $\mathbf{M}$ are the global stiffness and mass matrices, respectively. Proportional damping may be included using a complex modulus of elasticity. Alternatively, a viscous damping model can be used and $\mathbf{D} = \mathbf{K} + i\omega\mathbf{C} - \omega^2\mathbf{M}$, where $\mathbf{C}$ is the damping matrix. However, it is assumed that damping in the beams that are tested later in this thesis is very small, and the models that follow are treated as undamped.

3.6.2. Assembling elements

In general, the FE model and SE model are given by the dynamic stiffness relationships

$$\mathbf{p}^{fe} = \mathbf{D}^{fe}\boldsymbol{\phi}^{fe} \;\; ; \;\; \mathbf{p}^{w} = \mathbf{D}^{w}\boldsymbol{\phi}^{w} \tag{3.57}$$

where the superscripts fe denotes the FE model and w the SE (or wave model).

The relationships in Eq. 3.57 can be written as

$$\mathbf{p}^{L} = \mathbf{D}^{L}\boldsymbol{\phi}^{L} \;\; ; \;\; \mathbf{D}^{L} = \begin{bmatrix} \mathbf{D}^{fe} & \mathbf{0} \\ \mathbf{0} & \mathbf{D}^{w} \end{bmatrix} \;\; ; \;\; \boldsymbol{\phi}^{L} = \begin{Bmatrix} \boldsymbol{\phi}^{fe} \\ \boldsymbol{\phi}^{w} \end{Bmatrix} \;\; ; \;\; \mathbf{p}^{L} = \begin{Bmatrix} \mathbf{p}^{fe} \\ \mathbf{p}^{w} \end{Bmatrix} \tag{3.58}$$

Here, Eq. 3.58 is referred to as the local model, so-called because it describes the relationships between the nodal dofs and forces on the individual elements, and this is denoted by the superscript L.

When the FE and SE models are assembled, the resultant model is described as the "global" model and has a dynamic stiffness relationship given by

$$\mathbf{p}^G = \mathbf{D}^G \boldsymbol{\phi}^G \tag{3.59}$$

where G denotes the global model. The local and global dofs and forces are related by a transformation matrix $\boldsymbol{\Omega}$, such that

$$\boldsymbol{\phi}^L = \boldsymbol{\Omega}\boldsymbol{\phi}^G \;\; ; \;\; \mathbf{p}^G = \boldsymbol{\Omega}^T \mathbf{p}^L \tag{3.60}$$

Therefore, from Eq. 3.58 and 3.59, a general form of the dynamic stiffness relationship for the assembled FE and SE models is

$$\mathbf{p}^G = \boldsymbol{\Omega}^T \mathbf{D}^L \boldsymbol{\Omega} \boldsymbol{\phi}^G \tag{3.61}$$

The matrix $\boldsymbol{\Omega}$ contains the compatibility and equilibrium conditions that relate the local dofs and forces to the global dofs and forces. This matrix depends on how both the FE and SE models are defined.

3.6.3. A beam with a discontinuity

In the following, it is shown how a model of a beam with a discontinuity is developed by assembling a FE model of the discontinuity with SEs, as shown in Fig. 3.8.

The FE model consists of a section of the beam that contains the discontinuity and is shown in Fig. 3.9. The FE model used here is two-dimensional and assumes plane stress conditions. Fig. 3.9 details what are referred to as "interface nodes" and "non-interface nodes".

The interface nodes lie along the interface at which the FE and SE models are assembled. The dimensions of the cross section at the interface are equivalent to those of the SE model. In this model, no external forces are applied to the non-interface nodes.

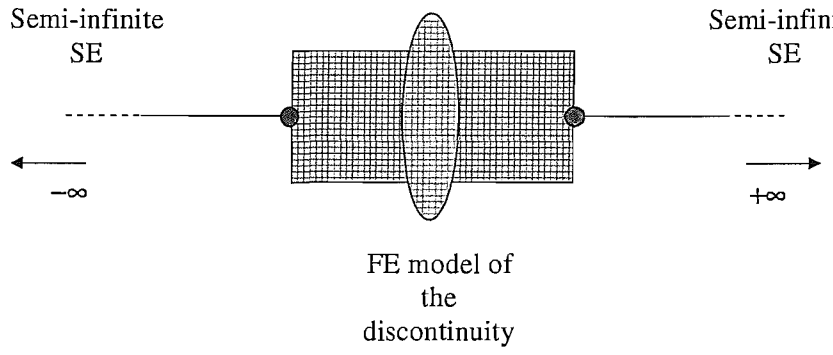

Fig. 3.8: The model of a discontinuity.

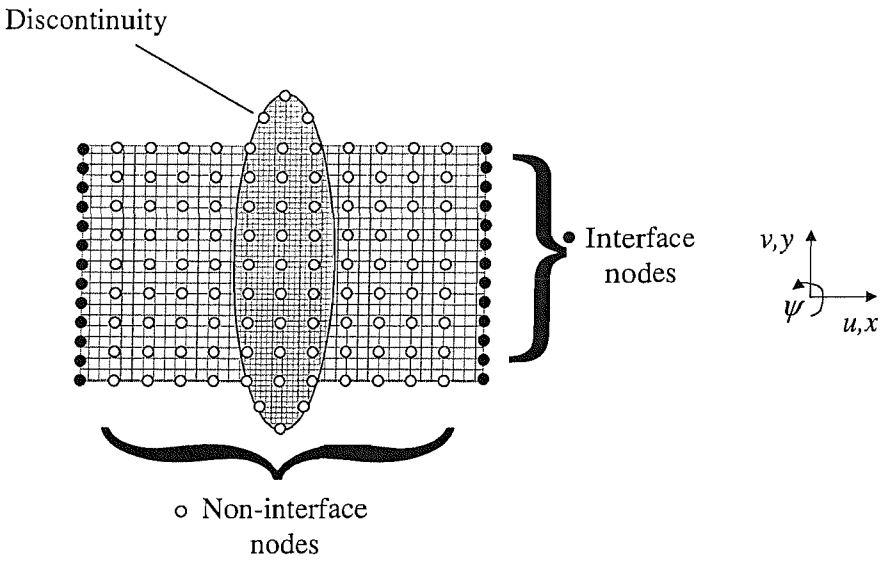

Fig. 3.9: The FE model of a section of beam containing the discontinuity.

As such, the DSM of the FE model can be condensed to reduce its size by removing the dofs associated with non-interface nodes. The DSM of the FE model can be partitioned as

$$\begin{Bmatrix} \mathbf{p}_i^{fe} \\ \mathbf{0} \end{Bmatrix} = \begin{bmatrix} \mathbf{D}_{ii}^{fe} & \mathbf{D}_{in}^{fe} \\ \mathbf{D}_{ni}^{fe} & \mathbf{D}_{nn}^{fe} \end{bmatrix} \begin{Bmatrix} \boldsymbol{\phi}_i^{fe} \\ \boldsymbol{\phi}_n^{fe} \end{Bmatrix} \tag{3.62}$$

where i and n stand for interface and non-interface, respectively. From Eq. 3.62 it can be

shown that

$$\mathbf{p}_i^{fe} = \mathbf{D}_i^{fe}\boldsymbol{\phi}_i^{fe} \; ; \quad \mathbf{D}_i^{fe} = [\mathbf{D}_{ii} - \mathbf{D}_{in}\mathbf{D}_{nn}^{-1}\mathbf{D}_{ni}] \tag{3.63}$$

where $\mathbf{D}_i^{fe}$ is a DSM that describes the interface nodal dofs and forces only.

The reduction of $\mathbf{D}^{fe}$ makes manipulation of the DSM easier but does not offer much improvement in computational time. As explained in [6], approximate methods might be used to reduce the number of dofs more efficiently, such as a modal decomposition of the mass and stiffness matrices for the non-interface dofs. However, as computational time was not found to be significant here, approximate methods are not used.

The process used to connect SE models to the FE model at both interfaces is identical; therefore, in the following it is described for one interface only. Fig. 3.10(a) illustrates the interface at one side of the FE model, the semi-infinite SE and lists the dofs and forces, where the subscript R has been added to denote the interface on the right-hand side of the FE model. Fig. 3.10(b) shows the assembled global model, with one node and its dofs and forces.

To assemble the models in Fig. 3.10(a) requires the transformation matrix $\boldsymbol{\Omega}$, as explained in the previous subsection. Firstly, the global node is defined as having the same number of nodal dofs and forces as the SE, such that

$$\boldsymbol{\phi}_R^G = \begin{Bmatrix} u_R^G \\ v_R^G \\ \psi_R^G \end{Bmatrix} \; ; \quad \mathbf{p}_R^G = \begin{Bmatrix} C_R^G \\ P_R^G \\ B_R^G \end{Bmatrix} \tag{3.64}$$

The dofs on the SE are related to the global model by the compatibility condition

$$\boldsymbol{\phi}_R^G = \boldsymbol{\phi}_R^w \tag{3.65}$$

Relating the dofs and forces on the FE model to the global dofs and forces is not

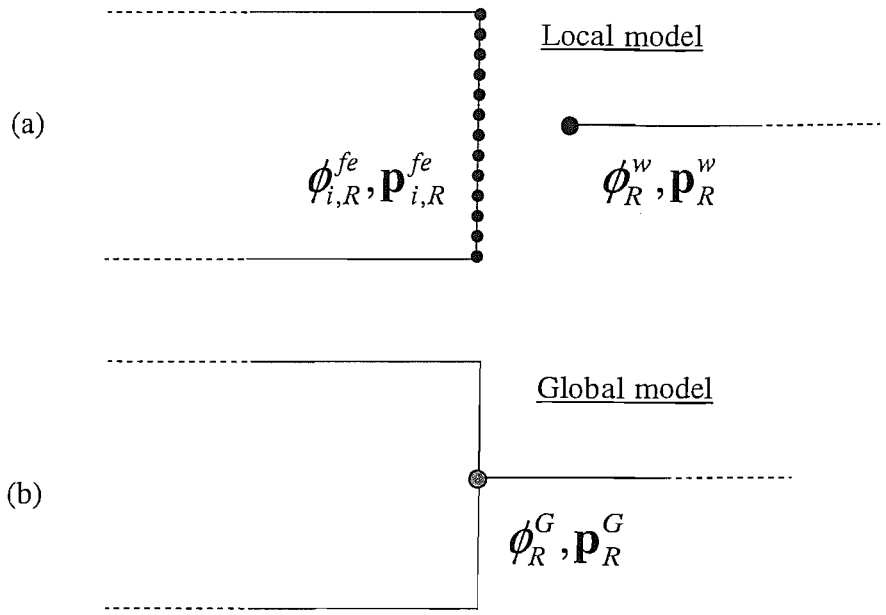

Fig. 3.10: The interface between the FE and SE models.

straightforward because, in general, $\phi_{i,R}^{fe}$ and ϕ_R^G are incompatible. A method for enforcing compatibility is offered in [6,22], however it is described differently here.

The equations that define a relationship between $\phi_{i,R}^{fe}$ and ϕ_R^G depend on the dofs and forces in the FE model. For all the models in this thesis, only the in-plane motion is considered. For conventional plane-stress/strain elements, such as those in commercial FE code, e.g., Ansys, each node in the FE model has two dofs and forces. For the jth node, these are written

$$\left(\phi_{i,R}^{fe}\right)_j = \begin{Bmatrix} u_j^{fe} \\ v_j^{fe} \end{Bmatrix} \; ; \quad \left(\mathbf{p}_{i,R}^{fe}\right)_j = \begin{Bmatrix} F_j^{fe} \\ P_j^{fe} \end{Bmatrix} \tag{3.66}$$

Compatibility between the FE model and the SE model is enforced by applying constraints, which assume that the FE model deforms like a rod/beam at the interface. The dofs on the interface are assumed to be related to the global dofs by

$$u_j^{fe} = u_R^G - y_j \psi_R^G \; ; \qquad v_j^{fe} = v_R^G \tag{3.67}$$

where y_j is the distance from the jth node on the interface of the FE model to the centre-line of the beam. In Eq. 3.67, the rotation is assumed to be small, that the axial waves cause axial displacement and Poisson contraction and that flexural waves cause both transverse displacement and axial displacement as the cross-section rotates. This approach is approximate and the errors will be considered in due course.

The constraints in Eq. 3.67 can be used to describe the relationship between all the dofs on the interface of the FE model and the global dofs, such that

$$\boldsymbol{\phi}_{i,R}^{fe} = \mathbf{G}\boldsymbol{\phi}_R^G \;;\; \mathbf{G} = \begin{bmatrix} \mathbf{G}_1 \\ \mathbf{G}_2 \\ \vdots \\ \mathbf{G}_J \end{bmatrix} \;;\; \mathbf{G}_j = \begin{bmatrix} 1 & 0 & -y_j \\ 0 & 1 & 0 \end{bmatrix} \tag{3.68}$$

where $\mathbf{G}$ is a matrix containing the constraints and J is the total number of nodes along the interface of the FE model. By Eqs. 3.65 and 3.68, the local dofs at the interface relate to the global dofs by

$$\boldsymbol{\phi}_R^L = \begin{bmatrix} \mathbf{G} \\ \mathbf{I} \end{bmatrix} \boldsymbol{\phi}_R^G \;;\; \boldsymbol{\phi}_R^L = \begin{Bmatrix} \boldsymbol{\phi}_{i,R}^{fe} \\ \boldsymbol{\phi}_R^w \end{Bmatrix} \tag{3.69}$$

Eq. 3.69 enforces compatibility at one interface. As mentioned earlier, semi-infinite SE models are connected at both interfaces as shown in Fig. 3.8. In this case, local dofs and forces can be written

$$\mathbf{p}^L = \mathbf{D}^L\boldsymbol{\phi}^L \;;\; \mathbf{D}^L = \begin{bmatrix} \mathbf{D}_i^{fe} & \mathbf{0} \\ \mathbf{0} & \mathbf{D}^w \end{bmatrix} \;;\; \mathbf{p}^L = \begin{Bmatrix} \mathbf{p}_{i,L}^{fe} \\ \mathbf{p}_{i,R}^{fe} \\ \mathbf{p}_L^w \\ \mathbf{p}_R^w \end{Bmatrix} \;;\; \boldsymbol{\phi}^L = \begin{Bmatrix} \boldsymbol{\phi}_{i,L}^{fe} \\ \boldsymbol{\phi}_{i,R}^{fe} \\ \boldsymbol{\phi}_L^w \\ \boldsymbol{\phi}_R^w \end{Bmatrix} \tag{3.70}$$

where the subscript L denotes the interface on the left-hand side of the model. The dynamic stiffness relationship for the assembled/global model is similar to Eq. 3.61 and

given by

$$\mathbf{p}^G = \boldsymbol{\Omega}^T \mathbf{D}^L \boldsymbol{\Omega}\, \boldsymbol{\phi}^G \;\; ; \;\; \boldsymbol{\Omega} = \begin{bmatrix} \mathbf{G} & \mathbf{0} \\ \mathbf{0} & \mathbf{G} \\ \mathbf{I} & \mathbf{0} \\ \mathbf{0} & \mathbf{I} \end{bmatrix} \tag{3.71}$$

The assembled model is a combination of FEs and SEs, and this model is referred to here as a FESE model.

3.7. Estimating scattering coefficients from a numerical model

To estimate the scattering coefficients from a FESE model, the model must include incident, reflected and transmitted waves, as illustrated in Fig. 3.11.

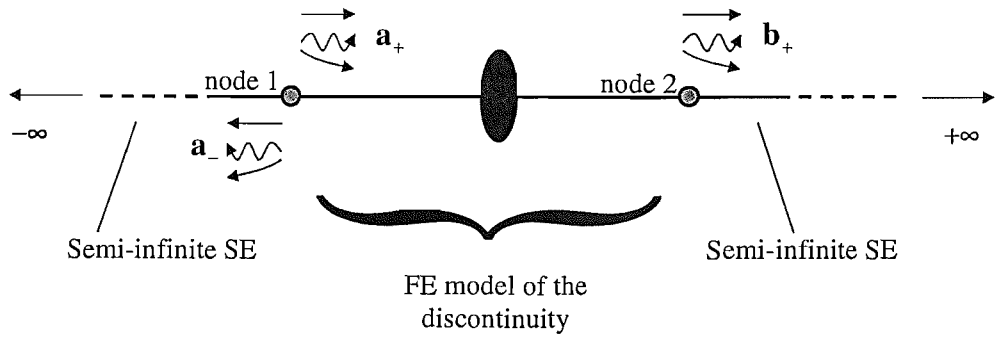

Fig. 3.11: Model required for estimating scattering coefficients.

The FESE model described in the previous section does not include the incident waves $\mathbf{a}_+$ because they are undefined in the semi-infinite SE that extends to $-\infty$ (see § 3.5.3.2, Eq. 3.55).

In order to create the model in Fig. 3.11 using a FESE model, a wave superposition method is used. This method is similar to that in [58] where it is used to determine the scattering of acoustic waves from structures. For this method, two models are created. The first is a model of a semi-infinite SE, fixed at its node, as shown in Fig. 3.12. This model represents the FESE model fixed (or blocked) at the left-hand interface. This model is used to calculate the forces at the fixed node, assuming that there is an incident and reflected wave field. Equal but opposite forces are then applied to the FESE model. By superposition of the nodal dofs and forces in the SE model, with a fixed node, and the FESE model, it is shown here that the model in Fig. 3.11 can be created.

To apply the condition that incident waves are present in the FESE model, node 1 is fixed and the wavefield is assumed to include the incident waves $(\mathbf{a}_+)_f$ and the reflected waves $(\mathbf{a}_-)_f$, as illustrated in Fig. 3.12, where f denotes the fixed node model.

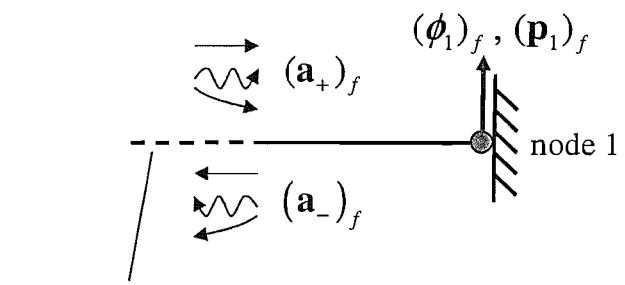

Fig. 3.12: FESE model fixed at the first node.

The dofs and forces at the fixed node in Fig. 3.12 are

$$(\boldsymbol{\phi}_1)_f = \mathcal{E}_+(\mathbf{a}_+)_f + \mathcal{E}_-(\mathbf{a}_-)_f = \mathbf{0} \tag{3.72}$$

$$(\mathbf{p}_1)_f = \mathcal{P}_+(\mathbf{a}_+)_f + \mathcal{P}_-(\mathbf{a}_-)_f \tag{3.73}$$

where $\mathcal{E}_{+,-}$ and $\mathcal{P}_{+,-}$ are matrices that relate the dofs and forces to the wave amplitudes, which are derived from the equation of motion. As node 1 is fixed, Eq. 3.72 reduces to

$$(\mathbf{a}_-)_f = \mathbf{R}_f(\mathbf{a}_+)_f \;\; ; \;\; \mathbf{R}_f = [-\mathcal{E}_-^{-1}\mathcal{E}_+] \tag{3.74}$$

where $\mathbf{R}_f$ is the reflection coefficient of the fixed end. From Eq. 3.73, the forces at the fixed node are

$$(\mathbf{p}_1)_f = (\mathcal{P}_+ + \mathcal{P}_-\mathbf{R}_f)\mathbf{a}_+ \tag{3.75}$$

Forces that are equal and opposite to Eq. 3.75 are applied to the first node of the FESE model, as shown in Fig. 3.13. When the force is applied, two sets of waves are created $(\mathbf{a}_-)_s$ and $(\mathbf{b}_+)_s$, where s denotes waves in the FESE model.

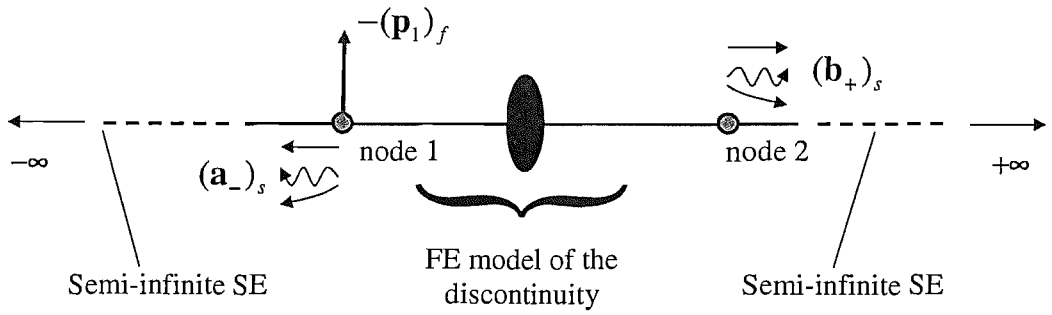

Fig. 3.13: FESE model of the discontinuity.

The global dynamic stiffness relation for the FESE model was given in Eq. 3.71. The global receptance matrix of the FESE model in Fig 3.13 is $\mathbf{H}^G = [\mathbf{D}^G]^{-1}$, such that

$$\begin{Bmatrix} \boldsymbol{\phi}_1^G \\ \boldsymbol{\phi}_2^G \end{Bmatrix} = \begin{bmatrix} \mathbf{H}_{11}^G & \mathbf{H}_{12}^G \\ \mathbf{H}_{21}^G & \mathbf{H}_{22}^G \end{bmatrix} \begin{Bmatrix} -(\mathbf{p}_1)_f \\ \mathbf{0} \end{Bmatrix} \tag{3.76}$$

In the FESE model, $\boldsymbol{\phi}_1^G = \mathcal{E}_-(\mathbf{a}_-)_s$, $\boldsymbol{\phi}_2^G = \mathcal{E}_+(\mathbf{b}_+)_s$ and $(\mathbf{p}_1)_f$ is given by Eq. 3.75. Therefore the receptance relation in Eq. 3.76 can be written

$$\begin{Bmatrix} \boldsymbol{\phi}_1^G \\ \boldsymbol{\phi}_2^G \end{Bmatrix} = \begin{bmatrix} \mathbf{H}_{11}^G \\ \mathbf{H}_{12}^G \end{bmatrix} \left[-(\mathcal{P}_+ + \mathcal{P}_-\mathbf{R}_f)\mathbf{a}_+ \right] \; ; \; \begin{Bmatrix} \boldsymbol{\phi}_1^G \\ \boldsymbol{\phi}_2^G \end{Bmatrix} = \begin{Bmatrix} \mathcal{E}_-(\mathbf{a}_-)_s \\ \mathcal{E}_+(\mathbf{b}_+)_s \end{Bmatrix} \tag{3.77}$$

To create the model in Fig. 3.11 the fixed node model in Fig. 3.12 and the FESE model in Fig. 3.13 are superposed. In doing so, the net nodal forces are zero while the nodal dofs in Fig. 3.11, $\boldsymbol{\phi}_1$ and $\boldsymbol{\phi}_2$, are given by

$$\boldsymbol{\phi}_1 = \boldsymbol{\phi}_1^G + (\boldsymbol{\phi}_1)_f \; ; \; \boldsymbol{\phi}_2 = \boldsymbol{\phi}_2^G \tag{3.78}$$

Therefore,

$$\begin{Bmatrix} \boldsymbol{\phi}_1 \\ \boldsymbol{\phi}_2 \end{Bmatrix} = \begin{bmatrix} \mathcal{E}_+\mathbf{a}_+ + \mathcal{E}_-\mathbf{a}_- \\ \mathcal{E}_+\mathbf{b}_+ \end{bmatrix} = \begin{bmatrix} \mathbf{H}_{11}^G \\ \mathbf{H}_{12}^G \end{bmatrix} \left[-(\mathcal{P}_+ + \mathcal{P}_-\mathbf{R}_f)\mathbf{a}_+ \right] \tag{3.79}$$

where $\mathbf{a}_+ = (\mathbf{a}_+)_f$, $\mathbf{a}_- = (\mathbf{a}_-)_f + (\mathbf{a}_-)_s$ and $\mathbf{b}_+ = (\mathbf{b}_+)_s$.

Finally, using the value of $(\mathbf{p}_1)_f$ from Eq. 3.75, the reflection and transmission matrices are

$$\mathbf{R} = -\mathcal{E}_-^{-1}\left[\mathbf{H}_{11}^G(\mathcal{P}_+ + \mathcal{P}_-\mathbf{R}_f) + \mathcal{E}_+\right] \tag{3.80}$$

$$\mathbf{T} = -\mathcal{E}_+^{-1}\,\mathbf{H}_{12}^G(\mathcal{P}_+ + \mathcal{P}_-\mathbf{R}_f) \tag{3.81}$$

3.8. Numerical examples

When the scattering coefficients of a discontinuity are estimated using a FESE model, a number of factors affect the accuracy of the result. Perhaps the most significant is the definition of the FE model and the choice of variables such as the number of elements/dofs in the model or the chosen element type.

To illustrate the accuracy of the method, a number of examples are presented in which the scattering coefficients of a uniform beam are estimated. In theory, the power reflection and transmission coefficients of a uniform beam are zero and one, respectively.

A FE model of the uniform beam is treated as a discontinuity and parameters such as element type and number are altered to show how they affect the accuracy of the results. From these results, one can suggest the most appropriate element type and number for future models. To illustrate the method further, the estimated scattering coefficients of an FESE model of a point mass are also presented and compared with analytical solutions.

All of the FE models were generated in Ansys and a plane-stress analysis performed. The beam model has $E = 210 \times 10^9$ Nm^{-2}, $\rho = 7850$ kgm^{-3} (mild steel), $\upsilon = 0.3$ and $h = 0.006$ m. These properties were chosen for their similarity to the experimental work in chapters 5 and 6. The results are presented as functions of non-dimensional axial or flexural wavenumbers, depending on the wave type under consideration. In both cases the wavenumbers are multiplied by the thickness of the beam to make them

non-dimensional. In Figs. 3.14 and 3.15 the non-dimensional wavenumbers are plotted against frequency. Given that the wavenumbers in the following numerical examples are very similar to the experiment, these values also give an indication of the frequency ranges that are used in the experimental results presented in chapter 5 onwards.

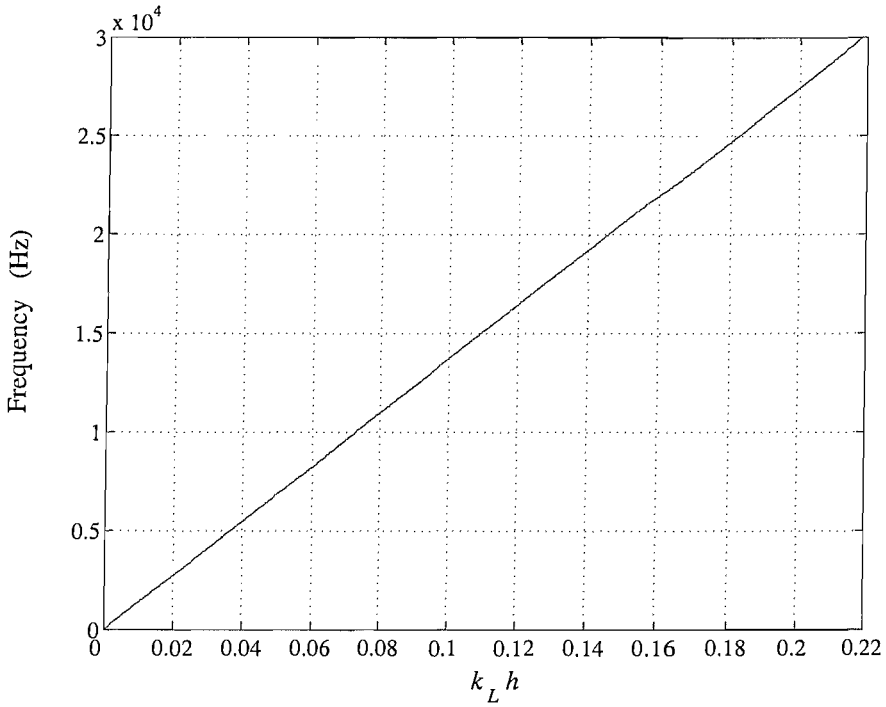

Fig. 3.14: Non-dimensional Love wavenumber, $k_L h$, plotted as a function of frequency.

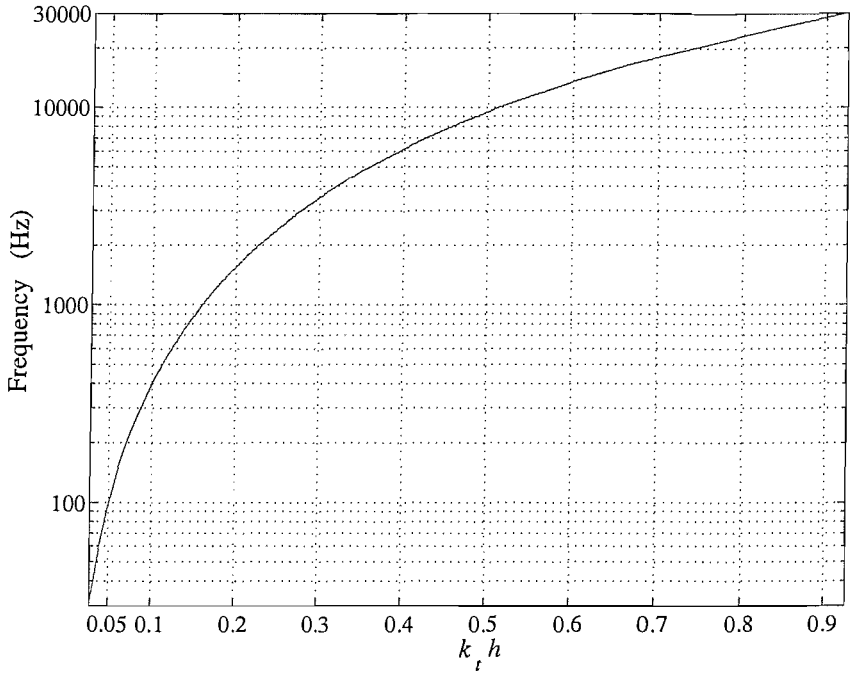

Fig. 3.15: Non-dimensional Timoshenko wavenumber, $k_t h$, plotted as a function of frequency.

3.8.1. Effect of the number of elements in the FE model

A FE model of the uniform beam is shown in Fig. 3.16. The model was meshed with triangular elements that have quadratic shape functions (plane2 in Ansys). The length of the model is $L = 10h$. If the number of elements prescribed along the interface boundary is J then the number of elements prescribed along the upper and lower boundaries are LJ/h. Defining the elements in such a way, results in a roughly uniform mesh.

To illustrate how changing the number of elements affects the estimated scattering coefficients, four FE models were generated in which $J = 2$, 5, 7 and 10. The numerical results in Fig. 3.17 show the estimated value of the axial power reflection coefficient r^{AA} as a function of non-dimensional Love wavenumber. It can be seen that $r^{AA} \neq 0$ but the accuracy of the estimate improves as J increases. Furthermore, there seems to be a

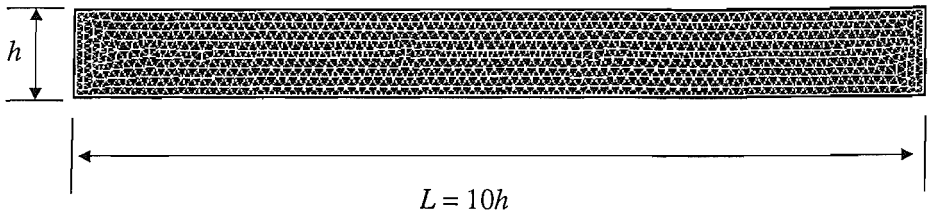

Fig. 3.16: The FE mesh of the uniform rod/beam.

non-zero reflection coefficient even for large J. It is thought that this error is due to differences between the FE and SE models.

In all the results presented, it was found that the power scattering coefficients sum to unity and, therefore, the transmission coefficient has not been given.

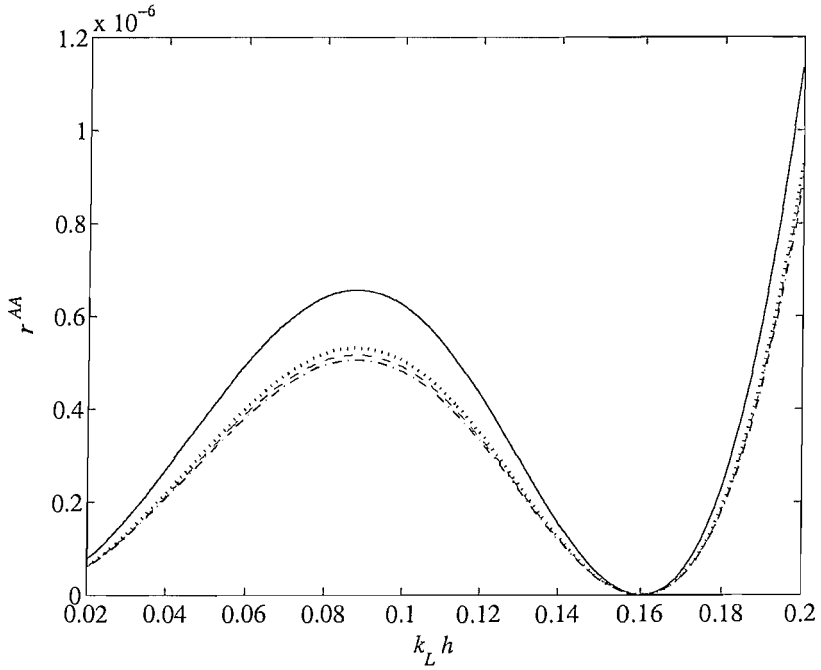

Fig. 3.17: Axial power reflection coefficients r^{AA} for models with different numbers of dofs: (—), $J = 2$; (· · ·), $J = 5$; (– –), $J = 7$; (-·-), $J = 10$.

The results in Fig. 3.18 also show that $r^{PP} \neq 0$ and that the model is more accurate for flexural waves as J is increased. There are noticeable differences between the models with $J = 2$ and $J = 5$ and only small differences between models with higher values of J. At higher frequencies, these differences are most clearly seen in Fig. 3.18 at the minima in r^{PP}. It is believed that the minima occur at different wavenumbers partly because the FE models are likely to have different wavenumbers.

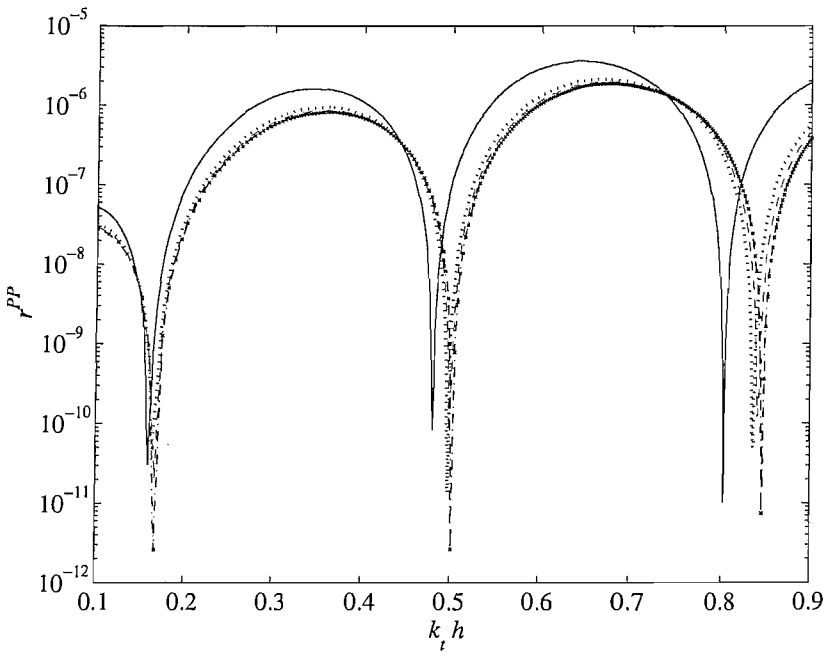

Fig. 3.18: Flexural power reflection coefficients r^{PP} for models with different numbers of dofs: (—), $J = 2$; (· · ·), $J = 5$; (––), $J = 7$; (-×-), $J = 10$.

In both Fig. 3.17 and Fig. 3.18 the reflection coefficients exhibit an undulatory behaviour and this is most noticeable in r^{PP}, in this frequency range. This behaviour is similar to that found in [59] for the reflection and transmission coefficients of beam inserts. It is believed that differences between the FE and SE models cause reflections at

the interfaces. The interference of the incident waves and waves reflected from the interfaces is thought to cause the undulant appearance of the results.

3.8.2. Effect of the element type in the FE model

A number of element types may be chosen to produce a plane-stress FE model. The numerical results presented here illustrate how the accuracy of the estimated scattering coefficients is affected by changing the element type.

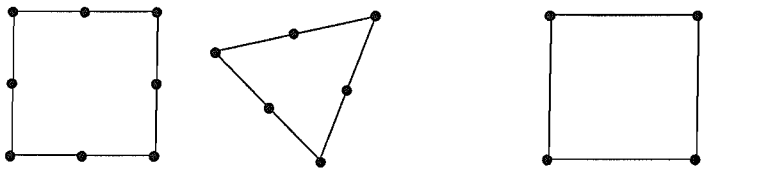

Fig. 3.19: Plane2 and Plane42 elements in Ansys.

Three FE models of the uniform beam were generated using different types of plane-stress element. In Ansys, these are plane2, rectangular shaped; plane2, triangular shaped; and plane42, rectangular shaped. The elements are illustrated in Fig. 3.19. The Plane2 elements have quadratic shape functions and mid-sidenodes, whereas the plane42 element has linear shape functions and no mid-sidenodes. The FE models were meshed so that the total number of dofs in each was approximately the same ($\approx$ 15000). This number equated to a mesh with approximately ten elements along the interface boundary for Plane2 and twenty elements for Plane42.

The numerical result in Fig. 3.20 shows r^{AA} for each model, where the largest

difference between the models is of the order of 10^{-7}. Fig. 3.21 shows a similar result for r^{PP}.

In Figs. 3.20 and 3.21 the plane42 element gives the better estimate of r^{AA} and r^{PP}. However, the plane42 element is less appropriate for models that have an irregular geometry, for which it is usually better to use triangular shaped elements. For example, a crack model requires triangular elements in order to model the shape of the crack, particularly around the crack tip.

As in the previous subsection, the results have a similar undulatory appearance, which is attributed to the mis-match between the FE and SE models. There are small differences between the results for plane2 and plane42 elements and, for versatility, plane2 is used in further models.

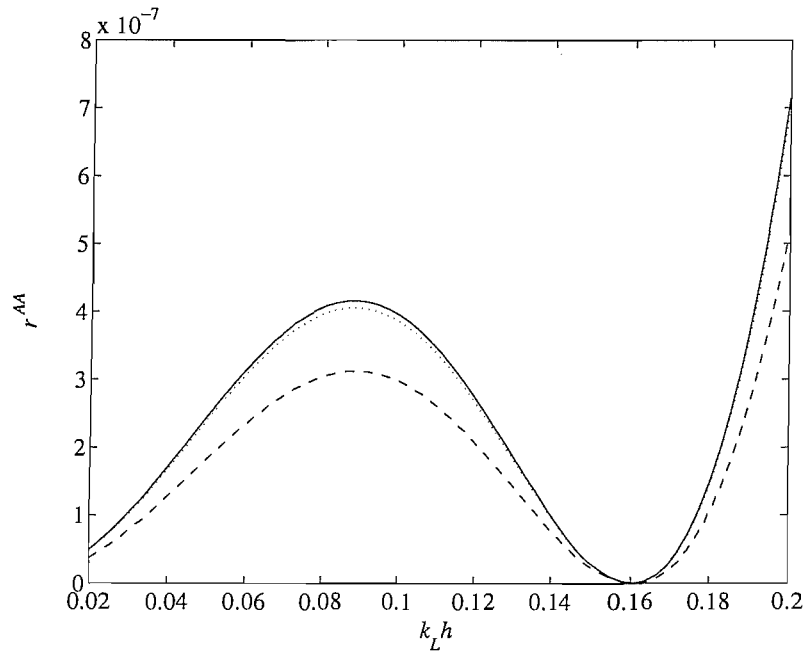

Fig. 3.20: Axial power reflection coefficients r^{AA} for models with different element types: (—), plane2 rectangular; (· · ·), plane2 triangular; (– –), plane42 rectangular.

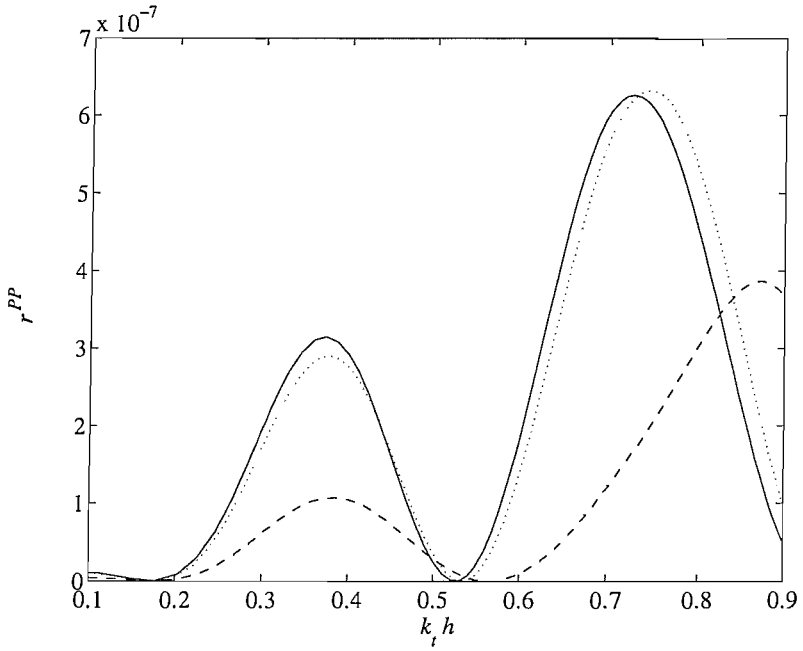

Fig. 3.21: Flexural power reflection coefficients r^{PP} for models with different element types: (—), plane2 rectangular; (· · ·), plane2 triangular; (– –), plane42 rectangular.

3.8.3. Estimating the scattering coefficients using different SE models

In the examples given so far, LVRT and TBT have been used to model the SEs. In this example, the scattering coefficients of the uniform beam are estimated for the case when LRT and EBT are used to define the SEs.

The numerical result in Fig. 3.22 shows the comparison of r^{AA} when LRT and LVRT are used. As the wavenumbers are different, r^{AA} is plotted as a function of frequency. In Fig. 3.22, it appears that there is a slight difference between the models. Again, the minimum in the results is attributed to the mis-match between the FE and SE models.

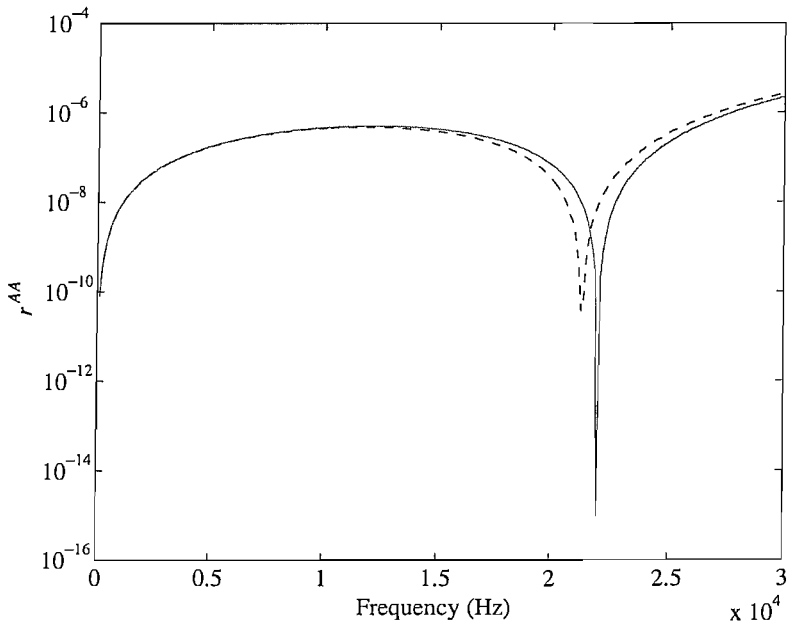

Fig. 3.22: Axial power reflection coefficients r^{AA} for models with different spectral elements: (—), LVRT; (– – –), LRT.

Fig. 3.23 shows r^{PP}, again as a function of frequency, for two models in which the SE is defined by either EBT or TBT. In Fig. 3.23, the model using TBT is much more accurate than when EBT is used.

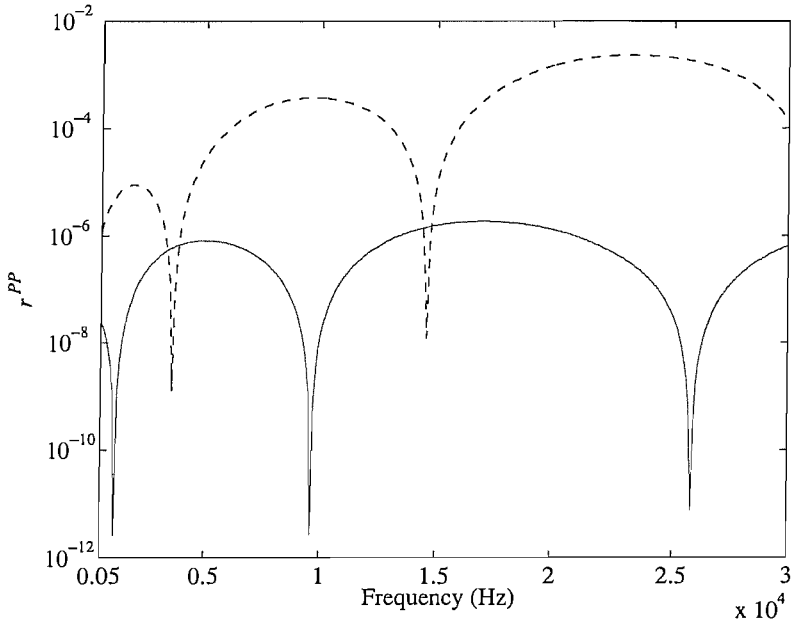

Fig. 3.23: Flexural power reflection coefficients r^{PP} for models with different spectral elements: (—), TBT; (– – –), EBT.

3.8.4. The scattering coefficients of a point mass

Estimating the scattering coefficients of a uniform beam illustrates the accuracy of the FESE model. From the results, it is clear that error exists but this is small. In the following, the scattering coefficients of a point mass are estimated using a FESE model to illustrate how the errors affect the estimates.

The model used to estimate the scattering coefficients of a point mass is shown in Fig. 3.24. The model comprises two uniform beam FE models to which semi-infinite

SEs are connected at one end, while the other ends are connected to either side of a point mass.

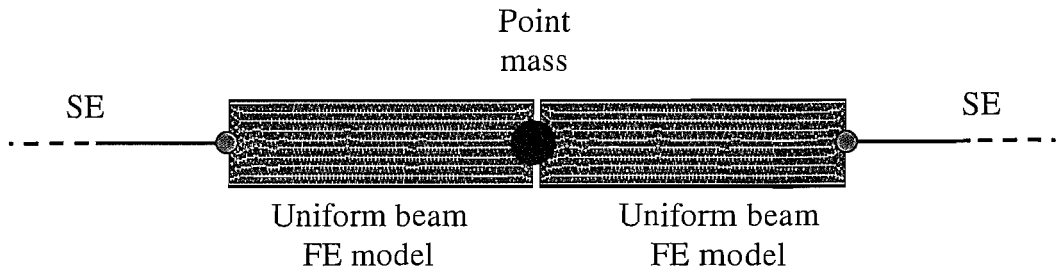

Fig. 3.24: FESE model of a point mass.

The dynamic stiffness relation for a point mass is

$$\mathbf{p}_m = -\omega^2 \begin{bmatrix} m & 0 \\ 0 & m \end{bmatrix} \boldsymbol{\phi}_m \; ; \; \boldsymbol{\phi}_m = \begin{Bmatrix} u_m \\ v_m \end{Bmatrix} \; ; \; \mathbf{p}_m = \begin{Bmatrix} C_m \\ P_m \end{Bmatrix} \tag{3.82}$$

where the subscript m denotes the local dofs and forces on the mass. The point mass does not have any rotational inertia and does not have a rotational dof.

The uniform beam FE models were described in the previous subsections. The FE models used here have ten elements along the interface and plane2 triangular elements were used in the analysis. The FE model, the mass and the SEs are assembled as described in § 3.6. The dofs on the interfaces of the FE models that connect to the mass are denoted $\left(\boldsymbol{\phi}_R^{fe}\right)_1$ and $\left(\boldsymbol{\phi}_L^{fe}\right)_2$, where the subscripts denote the FE beam model 1 and 2 that are located either side of the mass and the subscripts L and R denote the left and right-hand sides of the FE models. The compatibility conditions at the mass are

$$\left(u_R^{fe}\right)_1 = u_m = \left(u_L^{fe}\right)_2 \; ; \; \left(v_R^{fe}\right)_1 = v_m = \left(v_L^{fe}\right)_2 \tag{3.83}$$

whilst the rotation is continuous,

$$\left(\psi_R^{fe}\right)_1 = \left(\psi_L^{fe}\right)_2 \tag{3.84}$$

The scattering coefficients were estimated for three different masses equal to m = 0.05, 0.25, and 0.50 kg. Given that each model is plane stress, the width of the beam is treated as 1m, thus the mass per unit width in each case is m' = 0.05, 0.25, and 0.50 kg/m. The mass can also be considered in terms of a non-dimensional mass ratio, which is the added mass divided by the product of the mass per unit length of the beam and the wavelength. As such, the mass ratio is

$$m_R = \frac{m}{\rho A \lambda} \tag{3.85}$$

where λ is the wavelength for the particular wave type, i.e., axial or flexural. Fig. 3.25 shows the mass ratios for each mass as a function of non-dimensional wavenumber.

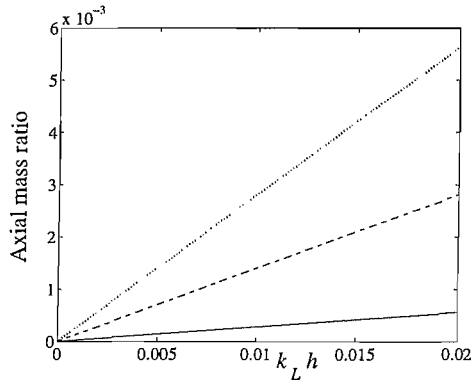

(a) Mass ratios as a function of non-dimensional axial wavenumber: (—), m = 0.05; (– –), m = 0.25; (· · ·), m = 0.5.

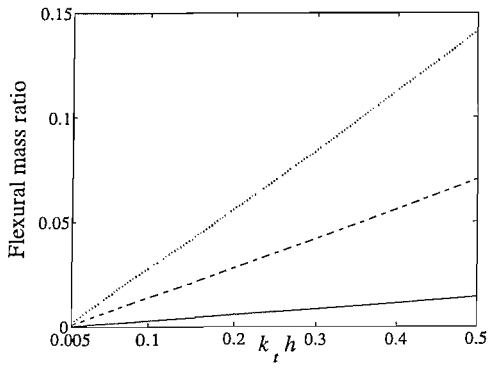

(b) Mass ratios as a function of non-dimensional flexural wavenumber: (—), m = 0.05; (– –), m = 0.25; (· · ·), m = 0.5.

Fig. 3.25: Mass ratios of the point masses.

The numerical results presented in the following, compare the reflection coefficients estimated from the FESE model with with the analytical result given in §. 3.4.1. The reflection coefficient r^{AA} is shown in Fig. 3.26. For each mass, the numerical result is inaccurate at very low frequencies. This error is believed to be caused by the mis-match between the FE and SE models. At higher frequencies for the larger masses, the error does not appear to be as significant, and the numerical and analytical results are very similar.

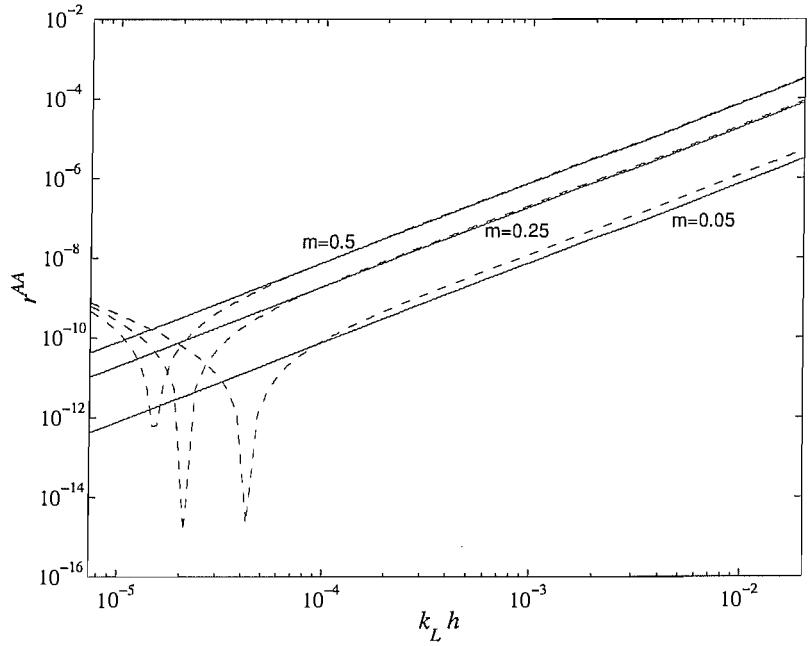

Fig. 3.26: Axial power reflection coefficients r^{AA} of a point mass: (—), analytical; (−−), numerical.

The reflection coefficient r^{PP} is shown in Fig. 3.26. Again, the numerical result is inaccurate at low frequencies when the reflection coefficient is of the order of the errors in the FESE model. Otherwise, the numerical and analytical results are very similar.

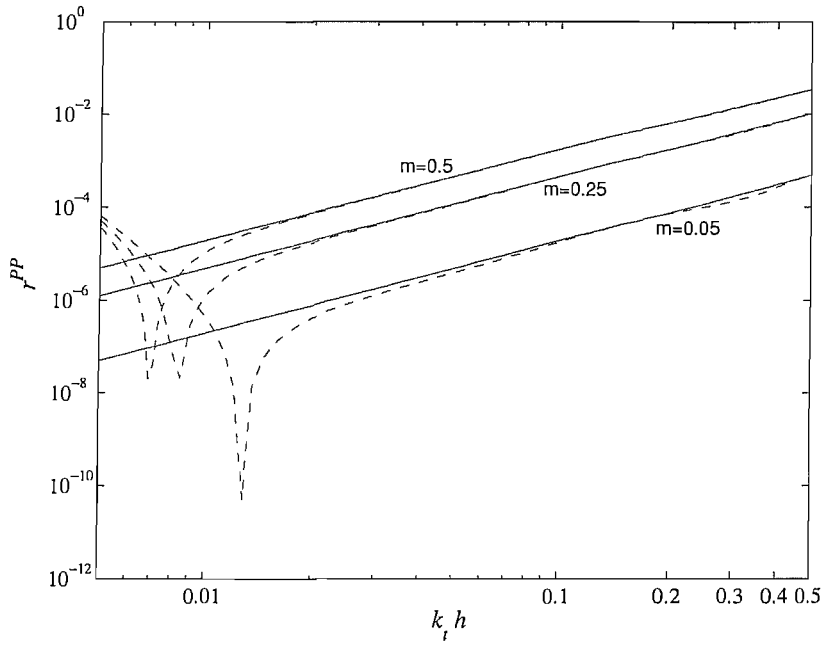

Fig. 3.27: Flexural power reflection coefficients r^{PP} of a point mass: (—), analytical; (– –), numerical.

3.9. Summary

The aim of this chapter was to describe a method that can be used to estimate the scattering coefficients of a discontinuity that may have complex dynamic characteristics, such as a crack.

Analytical wave methods for estimating the scattering coefficients are restricted to discontinuities where the compatibility and equilibrium conditions can be written analytically. When the discontinuity has complex dynamic characteristics, these can be estimated using a FE model.

Here, the SE method is used to impose infinite boundary conditions at the ends of a FE model. This is done by assembling semi-infinite SEs to the FE model using methods similar to those in [6]. From such a model, it is more straightforward to estimate the scattering coefficients of the discontinuity. The scattering coefficients are found using a

wave superposition method, similar to that in [58].

This method was used to estimate the scattering coefficients of a uniform beam and a point mass. It is clear from these numerical results that there is a mismatch between the FE and wave-based SE models, which results in wave reflection at the interfaces between the two.

The accuracy of the estimates of the scattering coefficients also depend on how the FE model is defined and parameters, such as the number of dofs in the model and the element type. The numerical results given here show that improving the FE model, for example by increasing the number of dofs, improves the estimates. However, it is not necessarily the case that continual refinement of the FE model results in continual improvement in the estimates. It is believed that the accuracy of the model is limited by the mismatch between the FE and SE models and the assumptions about the behaviour made when assembling the two.

From the numerical examples, the following remarks can be made as to how to develop a FESE model:

- The SEs should be defined by Love rod theory and Timoshenko beam theory.
- Triangular elements with quadratic shape functions are often more appropriate and appear no less accurate than other plane-stress elements.
- The number of elements chosen for the FE model depends on the frequency range of interest. For the frequency range considered here, in which the minimum wavelength is approximately $7h$, it was found that ten elements along the interface gave accurate results for both axial and flexural waves.

4. Modelling a beam with a notch or slot

4.1. Introduction

It is often the case that damage is assessed by comparing experimental results to a reference model (see chapter 2) [7]. In chapter 3, analytical and numerical methods for modelling a discontinuity and estimating the scattering coefficients have been considered in general terms. In this chapter, these methods are used to model a beam with a notch or slot and to predict the scattering coefficients of such damage cases. This is done with a view to comparing these predictions to experimental results and hence estimating the notch or slot depth (see chapters 6 and 7).

Two models are considered here. The first is an analytical lumped-spring model that can be found in a number of studies, for example [4] and [5]. The spring model is based on an analogy that relates the strain energy stored in a linear elastic spring to the strain energy local to the notch.

The second model considered is a FESE model, in which a section of the beam containing the notch is modelled using FE analysis. While still being elastic and linear, the FESE model includes a more detailed description of the notch than the lumped-spring model. In this chapter the two models are described and compared.

4.2. Background

In fracture mechanics, the behaviour of damage such as notches and slots is often is described by one of two methods: linear elastic fracture mechanics (LEFM) or

elastic-plastic fracture mechanics (EPFM) [11]. LEFM describes the stress field near to the notch tip in terms of the linear theory of elasticity, whereas EPFM uses non-linear elasticity to describe the stresses. Assuming that the plastic deformation close to the tip does not extend further than a small fraction of the dimensions of the fracture, the material may be described as brittle [10] and LEFM used to estimate the stresses around the tip. This approach is described in more detail by Tada et al. [11]. Here, only the LEFM case is considered.

4.2.1. Fracture modes

Three modes of fracture behaviour are illustrated in Fig. 4.1. Mode *I* is the opening mode, mode *II* is the in-plane shearing mode, and mode *III* is the out-of-plane tearing mode. Here, it is assumed that the depth of the fracture does not increase when loads are applied to the beam.

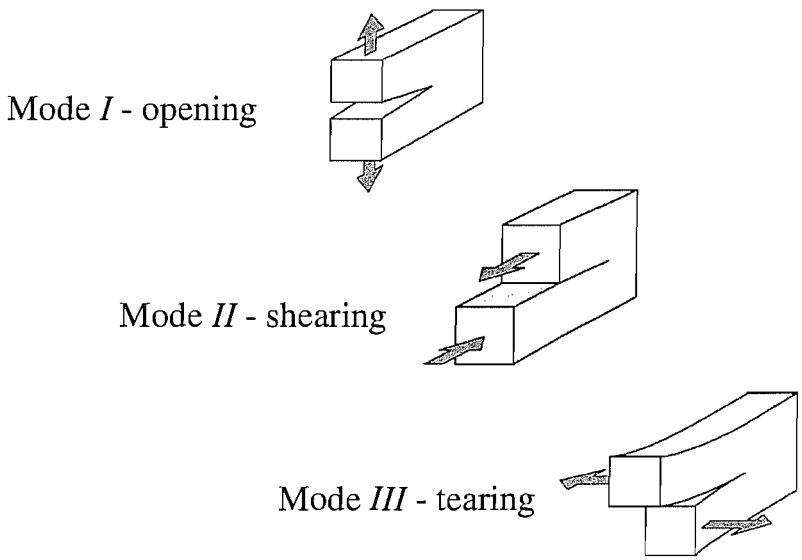

Fig. 4.1: Fracture modes.

The stresses at the fracture tip in each mode are characterised by a stress intensity factor (SIF) [11]. The SIF can be interpreted as a measure of the size of the stress singularity at the tip and depends upon the loading and the geometry. The SIF, $\mathcal{K}_N$, can be written [11] as

$$\mathcal{K}_N = \left[\hat{\sigma}\sqrt{\pi D}\right] F_N\left(\frac{D}{h}\right) \tag{4.1}$$

where $F_N(D/h)$ is a non-dimensional function based on the geometry of the fracture and the fracture mode, N denotes the fracture mode (I, II, or III), D is the depth of the fracture and $\hat{\sigma}$ is the maximum stress applied to the fracture in the given mode. The SIF is calculated in a number of ways that are described in [11].

4.2.2. Energy changes local to the fracture

In LEFM, as a fracture forms, potential energy stored in the beam is supplied to the fracture faces. The change in local strain energy at the fracture is described by the strain energy release rate, $\mathcal{G}_N$, which is the rate of change of potential energy per unit area of the fracture face (dU_c/dA_c) [10], where A_c is the area of the face. The strain energy local to the fracture, U_c, is given by the sum of the strain energies for each fracture mode. Here, only the in-plane behaviour is considered (modes I and II) and

$$U_c = \int_0^{A_c} \{\mathcal{G}_I + \mathcal{G}_{II}\}\ dA_c \tag{4.2}$$

where $\mathcal{G}_N = \frac{\mathcal{K}_N^2}{E}$ (for plane-stress). The relationship in Eq. 4.2 is used to derive the stiffness in the lumped-spring notch model.

4.3. Lumped-spring model for a beam with a notch

A beam notch fracture is illustrated in Fig. 4.2. Assuming the beam is excited both axially and flexurally, both the opening and shearing modes are of interest. In the lumped-spring notch model, the variation in strain energy associated with each mode is modelled as a localised stiffness variation [5]. The lumped-spring notch model is used often in the literature as a model for low frequency vibration-based damage assessment, e.g., [4,26,35].

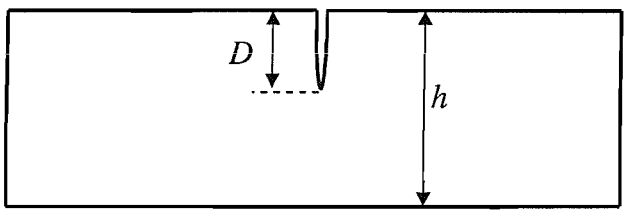

Fig. 4.2: Beam with a notch.

The notch model comprises three springs and is illustrated in Fig. 4.3. This model is similar to the model described in [35]. The opening mode is modelled using two springs. A rotational spring K_P is used to model the opening of the notch caused by flexural motion and a translational spring K_A is used to model the opening caused by axial waves. The shear mode is modelled with a translational spring K_S. In general, the shear crack mode may be excited by axial and flexural waves. However, when using LVRT and TBT to model the axial and flexural behaviour, only the flexural waves affect the shear spring as the shear stresses in LVRT are assumed to be zero.

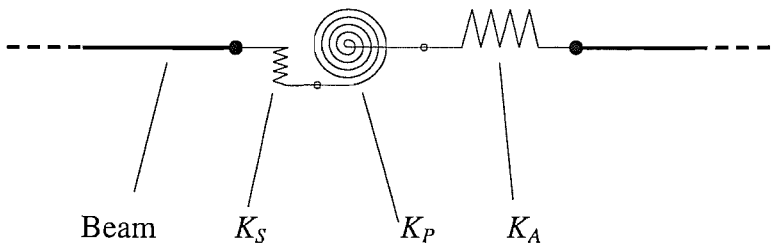

Fig. 4.3: The lumped-spring notch model.

The notch in Fig. 4.2 is not symmetric about the neutral axis, which causes wave-mode conversion as waves scatter from the notch. The lumped-spring model is considered to be symmetrically located with respect to the neutral axis of the beam and does not account for wave-mode conversion. The significance of wave-mode conversion is investigated in a later section of this chapter using FESE models. The wave-mode conversion might be included in the spring model using an eccentric spring and, although this is not considered here, it might be considered for future work.

4.3.1. Stiffness of the springs

An example of how the stiffnesses of the springs are derived is given in [5]. Aside from assuming that the notch behaves linearly and elastically, it is assumed that the it is

always open. Each spring has a frequency independent value of stiffness that is derived by equating the change in the local elastic energy caused by the existence of damage to the strain energy of a spring. The stiffnesses of each spring depend on the SIF (which are given in [11]). For each spring the values are given as

$$K_P = \frac{EI}{6\pi h \int_0^\gamma \gamma\,[X_P(\gamma)]^2\, d\gamma} \tag{4.3}$$

$$K_A = \frac{Eb}{2\pi \int_0^\gamma \gamma\,[X_A(\gamma)]^2\, d\gamma} \tag{4.4}$$

$$K_S = \frac{Eb}{2\pi \int_0^\gamma \gamma\,[X_S(\gamma)]^2\, d\gamma} \tag{4.5}$$

where $\gamma = D/h$ is the non-dimensional notch depth and the non-dimensional functions $X_{P,A,S}(\gamma)$ are specific to the fracture mode and derived from the SIF. The functions X_A, X_P and X_S are given by [11] as

$$X_A(\gamma) = \sqrt{\frac{\tan(\pi\gamma/2)}{\pi\gamma/2}}\,\frac{0.752 + 2.02\gamma + 0.37[1 - \sin(\pi\gamma/2)]^3}{\cos(\pi\gamma/2)} \tag{4.6}$$

$$X_P(\gamma) = \sqrt{\frac{\tan(\pi\gamma/2)}{\pi\gamma/2}}\,\frac{0.923 + 0.199[1 - \sin(\pi\gamma/2)]^4}{\cos(\pi\gamma/2)} \tag{4.7}$$

$$X_S(\gamma) = \frac{1.30 - 0.65\gamma + 0.37\gamma^2 + 0.28\gamma^3}{\sqrt{1-\gamma}} \tag{4.8}$$

Figs. 4.4 and 4.5 show the variation of the stiffnesses for the lumped-spring model as a function of γ. These values are calculated from Eqs. 4.3 to 4.5. At small values of γ the springs are stiff and, as γ approaches unity, the springs become more flexible.

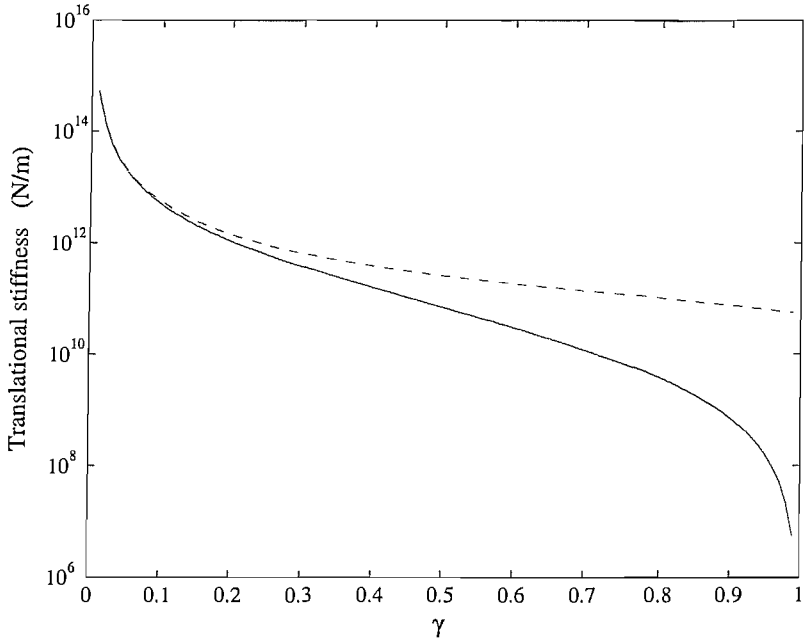

Fig. 4.4: Translational notch stiffnesses: (—), K_A; (– –), K_S.

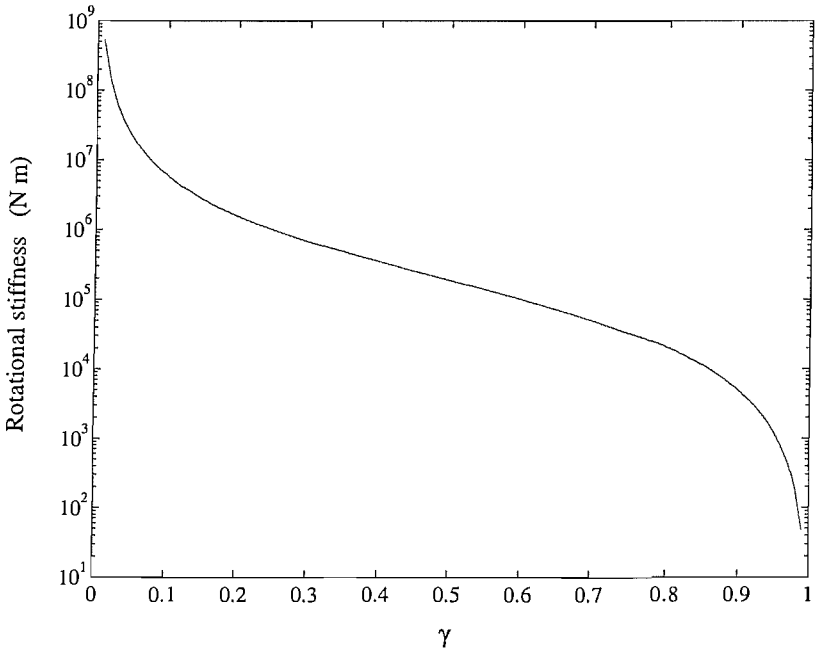

Fig. 4.5: Rotational notch stiffness K_P.

4.4. Wave scattering from the lumped-spring notch model

The dynamic behaviour of the lumped-spring model can be characterised in terms of its scattering coefficients, which can be found analytically from the compatibility and equilibrium conditions of the spring, as in § 3.4. This problem has also been considered in [15] for axial behaviour in a Timoshenko beam.

4.4.1. Axial wave scattering

The axial scattering coefficients R^{AA} and T^{AA} are calculated using Love rod theory. As there is no wave-mode conversion in the model, in reference to chapter 3 (Eqs. 3.26 and 3.27), $R^{AP,PA} = 0$ and $T^{AP,PA} = 0$. The compatibility and equilibrium conditions that describe the axial behaviour at the springs are

$$F_+ = K_A \frac{\partial}{\partial x}(u_+ - u_-) \;\; ; \;\; F_+ = F_- \tag{4.9}$$

where the subscripts + and – denote the left and right-hand sides of the discontinuity. From Eq. 4.9, the scattering coefficients can be shown to be

$$R^{AA} = \frac{i\tilde{C}_A}{i\tilde{C}_A + 2} \;\; ; \;\; T^{AA} = \frac{2}{i\tilde{C}_A + 2} \tag{4.10}$$

where $\tilde{C}_A$ is the non-dimensional compliance, given by

$$\tilde{C}_A = 2\pi(k_L h)\left[1 - (k_0 g\upsilon)^2\right] \int_0^{\gamma} \gamma\,[X_A(\gamma)]^2 \, d\gamma \tag{4.11}$$

Other than at very high frequencies, $(k_0 g\upsilon)^2 << 1$, therefore the non-dimensional stiffness in Eq. 4.11 is a function of non-dimensional wavenumber and the integrated term $\gamma[X_A(\gamma)]^2$.

The scattering coefficients in Eq. 4.10 depend on the stiffness and, therefore, the notch depth. As the depth increases, the stiffness decreases. In the frequency range of interest, at a given frequency, the magnitude of the reflection coefficient increases with notch

depth. As $\omega \rightarrow 0$, $R^{AA} \rightarrow 0$ and $T^{AA} \rightarrow 1$; while at high frequencies (providing that $(k_0 g\upsilon)^2 < 1$) $R^{AA} \rightarrow 1$ and $T^{AA} \rightarrow 0$.

The numerical results presented in Fig. 4.6 show the power reflection coefficient r^{AA} as a function of non-dimensional Love wavenumber, for a number of different notch depths. A mild steel beam was used for the model, with material properties and dimensions equal to $E = 210\text{GNm}^{-2}$, $\rho = 7850\text{kgm}^{-3}$, $h = 0.006\text{m}$ and $\upsilon = 0.3$. The result in Fig. 4.6 confirms that, for a given frequency in this range, the value of r^{AA} is larger for larger depths.

The transmission coefficient has not been given but, by conservation of energy, it is such that $t^{AA} = 1 - r^{AA}$.

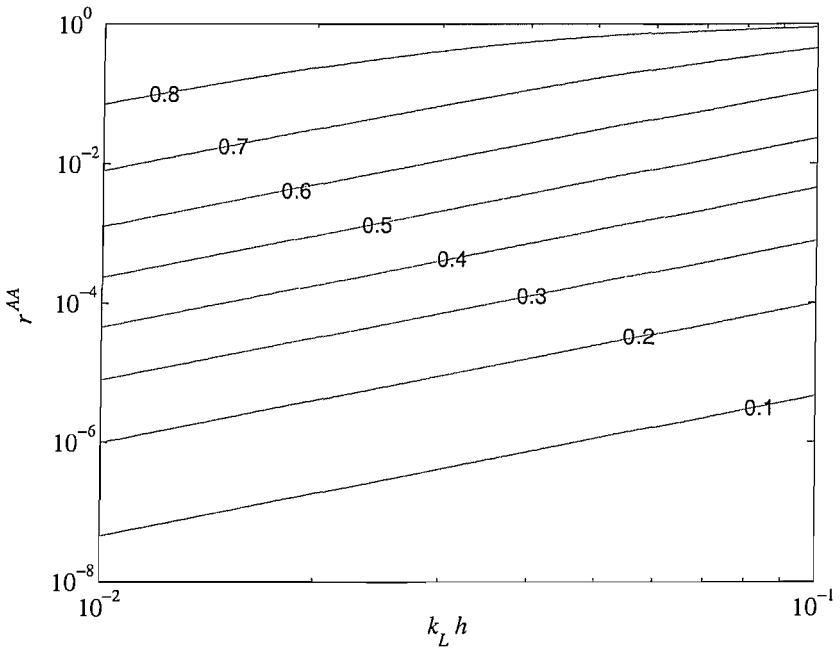

Fig. 4.6: Axial power reflection coefficients r^{AA} for various γ.

4.4.2. Flexural wave scattering

For flexural motion, the equilibrium and compatibility conditions of the lumped-spring model are

$$Q_+ = K_S(v_+ - v_-) \;\; ; \;\; M_+ = K_P(\psi_+ - \psi_-) \tag{4.12}$$

$$Q_+ = Q_- \;\; ; \;\; M_+ = M_- \tag{4.13}$$

The variables in Eqs. 4.12 and 4.13 are defined in chapter 3, § 3.2.4.

The analytical solution for the scattering coefficients using TBT is cumbersome and this result is not given here. To illustrate how the model behaves, the scattering coefficients are given for EBT. It can be shown that the scattering coefficients calculated from EBT and TBT are very similar over the frequency range used here.

From Eqs. 4.12 and 4.13, the scattering coefficients for propagating and nearfield flexural waves can be shown to be

$$\begin{bmatrix} R^{PP} & R^{PN} \\ R^{NP} & R^{NN} \end{bmatrix} = \frac{1}{\tau} \begin{bmatrix} i(1-\tau) - \tilde{C}_P - \tilde{C}_S & (1+i)(\tau-1) + \tilde{C}_S - i\tilde{C}_P \\ (1-i)(\tau-1) - \tilde{C}_P - i\tilde{C}_S & -i(\tau-1) + i(\tilde{C}_S - \tilde{C}_P) \end{bmatrix} \tag{4.14}$$

$$\begin{bmatrix} T^{PP} & T^{PN} \\ T^{NP} & T^{NN} \end{bmatrix} = \frac{1}{\tau} \begin{bmatrix} 1 + \tilde{C}_P - \tilde{C}_S & \tilde{C}_S + i\tilde{C}_P \\ \tilde{C}_P - i\tilde{C}_S & 1 + i(\tilde{C}_P + \tilde{C}_S) \end{bmatrix} \tag{4.15}$$

where

$$\tau = \left\{(1+i)\tilde{C}_P + 1\right\}\left\{(-1+i)\tilde{C}_S + 1\right\} \tag{4.16}$$

The parameters $\tilde{C}_P$ and $\tilde{C}_S$ are non-dimensional compliances, given by

$$\tilde{C}_P = 24\pi(k_b h) \int_0^\gamma \gamma\,[X_P(\gamma)]^2 \, d\gamma \tag{4.17}$$

$$\tilde{C}_S = \frac{2\pi}{3}(k_b h)^3 \int_0^\gamma \gamma\,[X_S(\gamma)]^2 \, d\gamma \tag{4.18}$$

where, in Eq. 4.18, it has been assumed that the beam has a rectangular cross-section, such that $I = bh^3/12$. The non-dimensional compliances, as in Eq. 4.11, are functions of non-dimensional wavenumber and the integrals of $\gamma\,[X_P(\gamma)]^2$ or $\gamma\,[X_S(\gamma)]^2$.

At more than half a wavelength from the spring, the nearfield wave is negligible, therefore the scattering terms of most interest are R^{PP} and T^{PP}. The stiffnesses of the springs are calculated using Eq. 4.7 and 4.8. For all values of γ, the stiffnesses of the springs are such that $K_P < K_S$. At low frequencies it can be shown that $\tilde{C}_P >> \tilde{C}_S$ and, therefore, the rotational spring dominates the scattering.

Fig. 4.7 shows the power reflection coefficient r^{PP} for a number of different notch depths, as a function of non-dimensional Euler-Bernoulli wavenumber. The beam model is the same as that used in the previous subsection. Again, the power transmission coefficient, by conservation of energy, is $t^{PP} = 1 - r^{PP}$.

Over the frequency range shown in Fig. 4.7, the rotational spring dominates the scattering properties of the lumped spring model and the results shown in Fig. 4.7. As a result, the power reflection coefficient tends to 0.5 over this frequency range: the value it would asymptote to if only the rotational spring was present in the model. Were we to consider the behaviour at higher frequencies, the translational spring becomes more significant and at much higher frequencies this dominates the scattering and the power reflection coefficient asymptotes to unity. Such high frequencies are not considered in this thesis.

EBT has been used here to find the scattering coefficients of the model. However, for the remainder of this thesis, any result that is derived from the lumped-spring model uses TBT in the calculation.

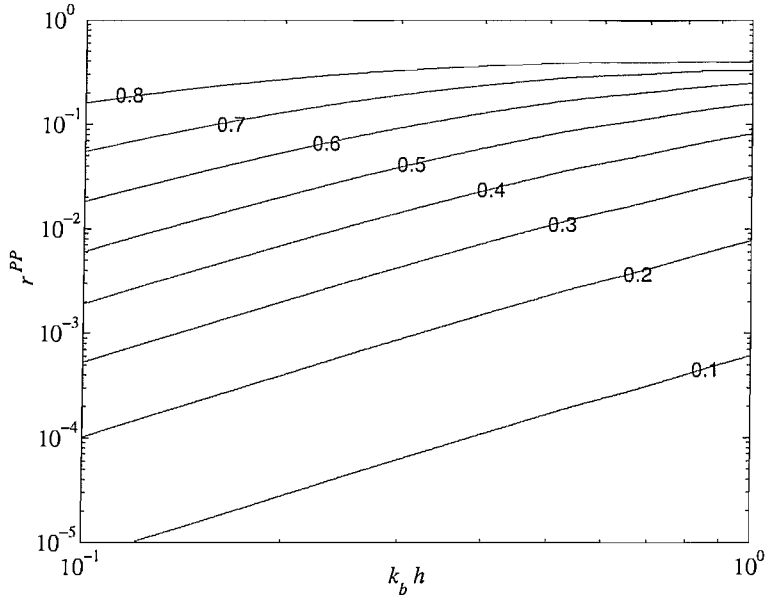

Fig. 4.7: Flexural power reflection coefficients r^{PP} for selected values of γ.

4.4.3. Remarks

The results from the lumped-spring notch model suggest that the scattering coefficients depend on frequency and notch depth. In the frequency range of interest, the reflection coefficients are largest when the frequency and notch depth are large also. For all depths, the scattering is small at low frequencies, and in the limit $\omega \rightarrow 0$ then $r^{AA} \rightarrow 0$ and $r^{PP} \rightarrow 0$. The results given here also show that $r^{PP} > r^{AA}$ in this frequency range.

4.5. A numerical model of a beam with a notch

The accuracy of the damage model is important if it is to be compared with experimental results, in order to estimate, for example, notch depth. The lumped-spring model involves various assumptions, does not include behaviour such as wave-mode conversion or the exact shape of the damage.

In this section, an FESE model of the beam is considered, in which a section of the

beam including the notch is modelled with FE analysis. The FESE model provides a more detailed description of the dynamic behaviour of the notch than the lumped-spring model, by inclusion of wave-mode conversion and the notch shape. Various numerical examples are presented here to illustrate the differences between the models.

4.5.1. Defining the model

Details of the model are shown in Fig. 4.8, where L is the length of the section, and an example of the FE model is given in Fig. 4.9.

In the FE model, the size of the notch opening/width must be defined. The width of the notch at the opening, W, is described by the non-dimensional parameter $\tilde{W} = W/h$. From numerical examples, it was found that there were no significant differences between estimates of the scattering coefficients from models with notch widths smaller than $\tilde{W} = 1/300$. In this case, it is assumed that the more important parameter that defines the scattering is the notch depth. This may not be the case at very high frequencies and when the stresses around the edges of the opening become important. In the models that follow, the width is set to $\tilde{W} = 1/300$, unless otherwise stated.

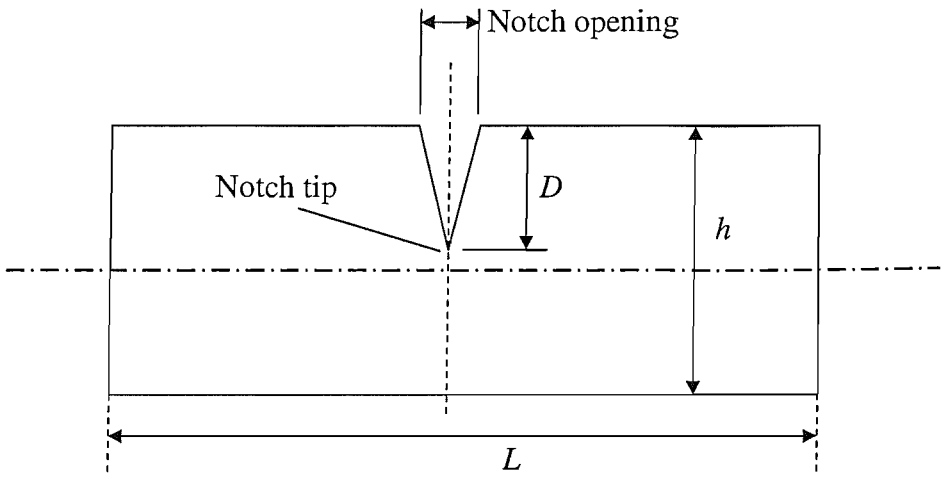

Fig. 4.8: Schematic of the beam with a notch.

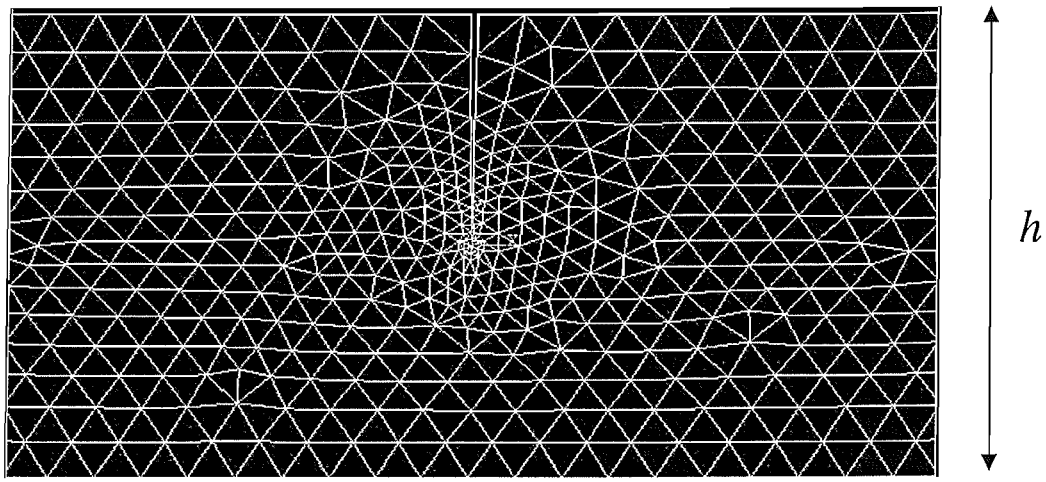

Fig. 4.9: FE mesh of the notch.

In the FE model, plane-stress triangular elements with quadratic shape functions (plane2 in Ansys) were used. The mesh was concentrated around the notch tip and, local to the tip, isosceles triangles were used, as illustrated in Fig. 4.9. The number of elements was prescribed along the upper, lower and interface boundaries of the model. The number of elements is such that there are the same number of elements prescribed per

unit length of the boundary, e.g., if there are 10 elements prescribed along the interface which has a length h and $L = 10h$ (see Fig. 4.8) then there are 100 elements prescribed along the upper and lower boundaries. This gives a more even mesh away from the notch tip. In the results that follow, the models had 10 elements along the interfaces and the beam is mild steel with $E = 210\text{GNm}^{-2}$, $\rho = 7850\text{kgm}^{-3}$, $h = 0.006$ and $\upsilon = 0.3$.

In the FE model, the notch faces are unconstrained and the crack can open and close but it is assumed the notch faces do not come into contact. Therefore it is assumed that the relative displacements of the nodes along the faces of the notch are comparatively small.

4.5.2. Effect of number of dofs in the model

The number of dofs in the FE model has a bearing on the accuracy of the FESE model, as explained in chapter 3. In the examples that follow, the scattering coefficients were estimated for four FESE models with $\gamma = 0.50$, in which the number of elements along the interface between the FE and SE regions was 10, 12, 15 and 20, respectively. Each model was of length $L = 10h$, so that the number of elements prescribed along the upper and lower boundaries was 10 times the number of elements along the interface.

The numerical results in Fig. 4.10 show r^{AA} as a function of non-dimensional wavenumber. It is not possible over this range to distinguish between the predictions of each model. The results in Fig. 4.11 shows that this is also true of r^{PP}.

The transmission coefficients are not shown. In each model it was found that conservation of energy was met, namely that $r^{AA} + t^{AA} + r^{AP} + t^{AP} = 1$ and $r^{PP} + t^{PP} + r^{PA} + t^{PA} = 1$ to within machine accuracy.

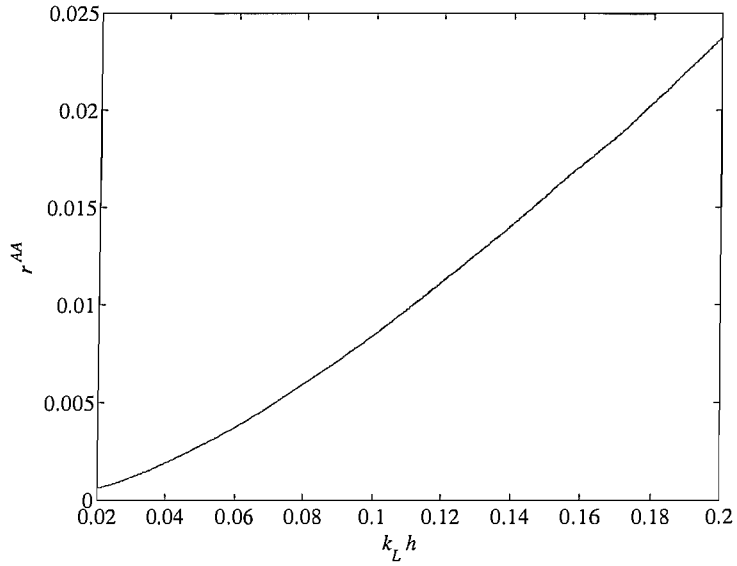

Fig. 4.10: Axial power reflection coefficients r^{AA} for models with 10, 12, 15 and 20 elements along the interface boundary and $\gamma = 0.50$.

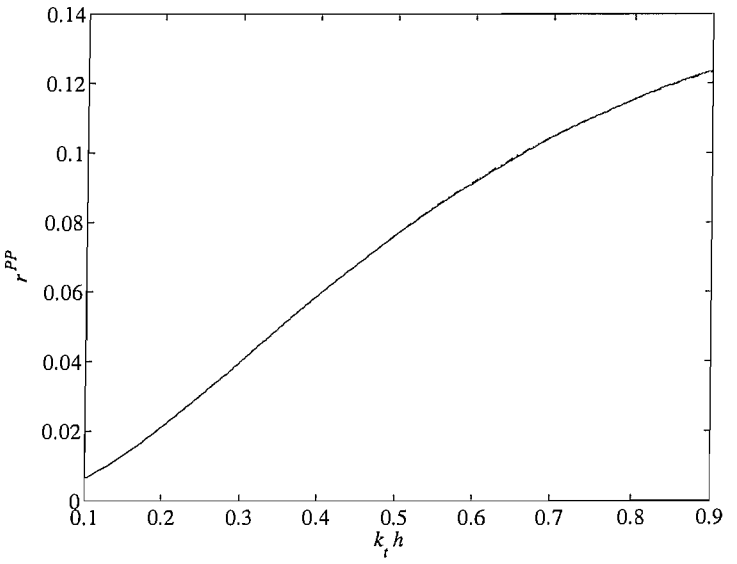

Fig. 4.11: Flexural power reflection coefficients r^{PP} for models with 10, 12, 15 and 20 elements along the interface boundary and $\gamma = 0.50$.

The FESE notch model includes wave-mode conversion that occurs when waves are scattered by the notch. The total energy that is transferred from an incident flexural wave to reflected and transmitted axial waves is illustrated in Fig. 4.12. Again, there are no distinguishable differences between the models with different numbers of dofs. The results in Fig. 4.12 shows that the amount of energy being transferred to axial waves is significant, making up around 10% of the total scattered energy at the higher frequencies.

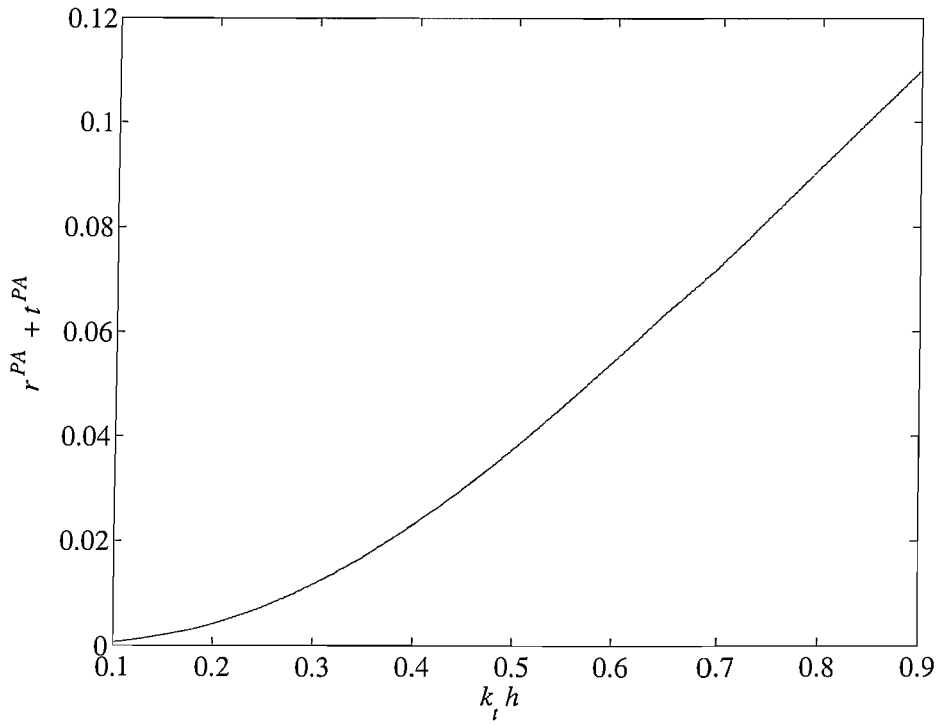

Fig. 4.12: Sum of the wave-mode conversation terms $r^{PA} + t^{PA}$ for models with 10, 12, 15 and 20 elements along the interface boundary and $\gamma = 0.50$.

These examples have been repeated for a number of other notch depths. Over the frequency range of interest, there were no significant differences when the number of dofs is increased, therefore, the number of elements along the interface is chosen as 10 for all FESE models that follow.

4.5.3. Effect of the length of the model

The large stresses at the notch tip are localised and, by the Saint-Venant's principle [60], it is assumed that details of the complicated stress field are insignificant at a length equal to 'a few' beam thicknesses from the notch. If the FE model is too short and the stress field at the interface includes the effects of the tip, the mis-match between the FE model and SEs is likely to be worse, making estimates of the scattering coefficients less accurate.

Five FE models, with $\gamma = 0.50$, are used here to illustrate how changing the length of the FE model affects the estimated scattering coefficients. The lengths of the models are $L = 10h$, $15h$, $20h$, and $25h$, respectively.

Figs. 4.13 and 4.14 show the power reflection coefficients r^{AA} and r^{PP} for each model. In both figures, it is difficult to discern between the models at low frequencies and there are only small differences at higher frequencies. Changing the length of the model alters the stress distribution at the interface and the wave interference that occurs due to reflections from the interface. It is believed that the differences seen in the results in Figs. 4.13 and 4.14, are caused by these changes rather than L being too small. Therefore, in all FESE crack models that follow, the length chosen is $10h$.

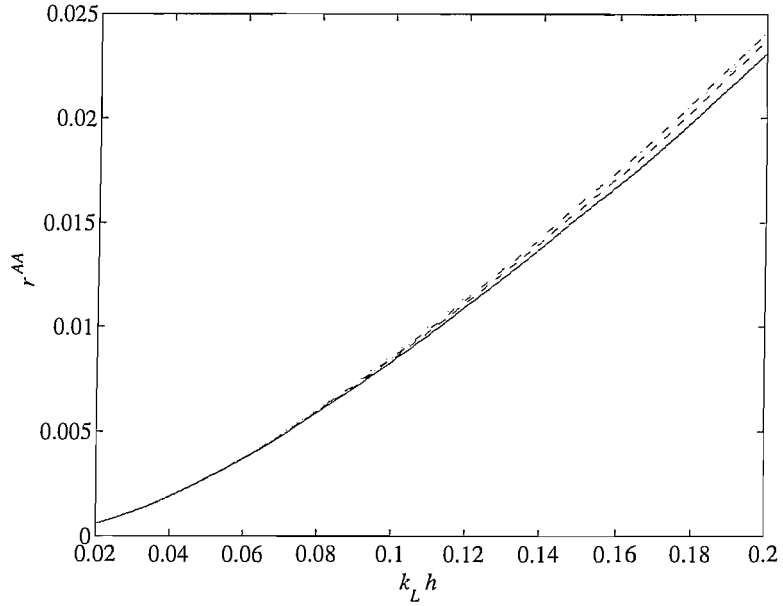

Fig. 4.13: Axial power reflection coefficient r^{AA} for FE models with various lengths:(—), $L = 10h$; (– –), $L = 15h$; (– · –), $L = 20h$; (· · ·), $L = 25h$.

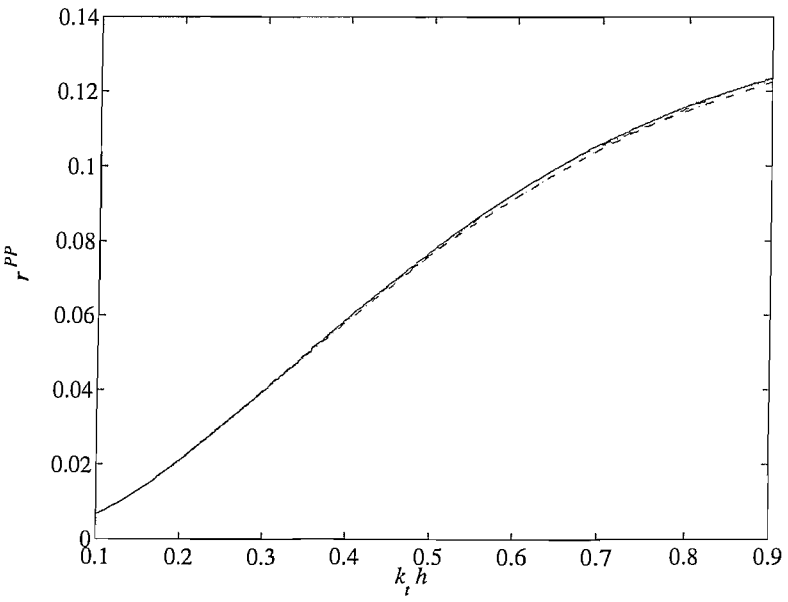

Fig. 4.14: Flexural power reflection coefficient r^{PP} for FE models with various lengths.:(—), $L = 10h$; (– –), $L = 15h$; (– · –), $L = 20h$; (· · ·), $L = 25h$.

4.5.4. Effect of the notch width

The FESE models thus far have considered a notch (see Fig. 4.8). In the experimental work described in chapter 6, the beam is damages by cutting a slot in the beam, which is like the model shown in Fig. 4.15. The slot is modelled in a similar manner to the notch. Given that there is no tip, the mesh density is increased around the base of the slot.

Fig. 4.16 shows r^{AA} for various widths and compares the slot model to the notch model where $\gamma = 0.50$. In the results, it would appear that the reflection coefficient depends on the width of the slot. Over this frequency range, larger slot widths cause larger reflection coefficients. When the width of the slot is small, up to $\tilde{W} = 1/30$, there are only small differences between the results.

Fig. 4.17 shows r^{PP} for each model. At low frequencies, for a given frequency, the reflection coefficient is larger for larger slot widths. However at high frequencies, for the larger slot widths, the reflection coefficient reaches a peak and then decreases. From the numerical model, it is difficult to explain the exact cause of this, though it may be due to changes in the transverse and rotary inertia at the slot.

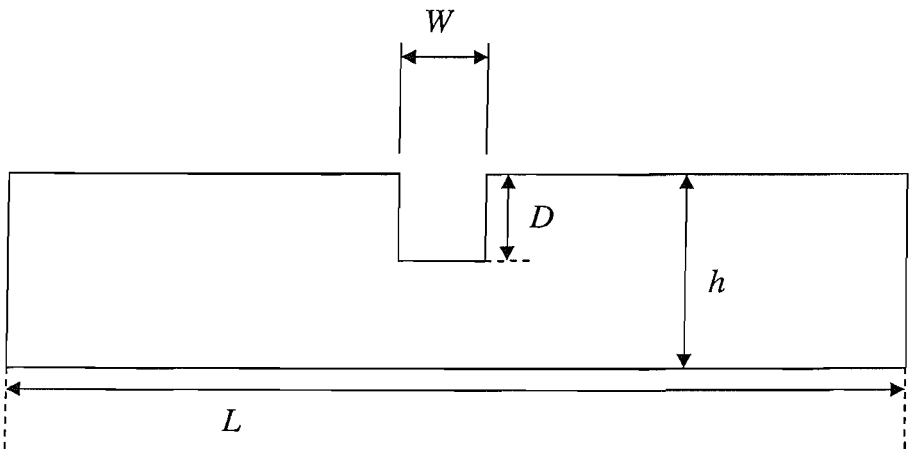

Fig. 4.15: A slot in a beam.

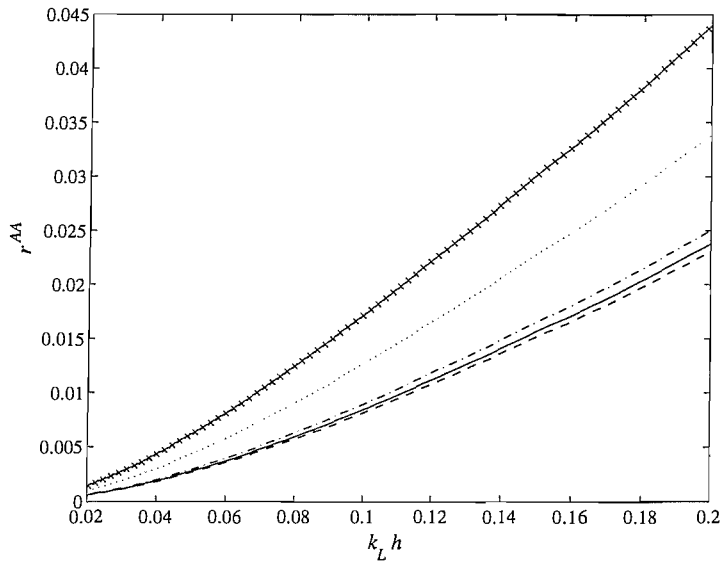

Fig. 4.16: Axial power reflection coefficients r^{AA} for different slot widths: (—), notch with $\tilde{W} = 1/300$; (––), slot with $\tilde{W} = 1/300$; (– · –), slot with $\tilde{W} = 1/30$; (· · ·), slot with $\tilde{W} = 1/6$;(-×-), slot with $\tilde{W} = 1/3$.

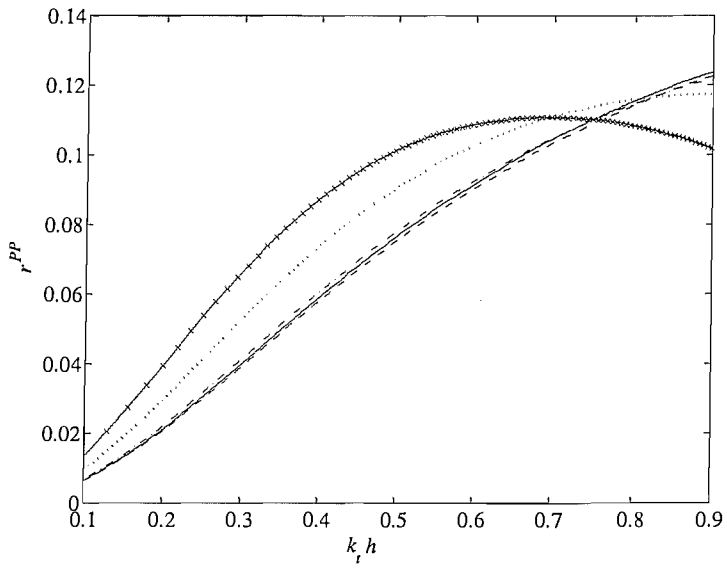

Fig. 4.17: Flexural power reflection coefficients r^{PP} for different slot widths: (—), notch with $\tilde{W} = 1/300$; (––), slot with $\tilde{W} = 1/300$; (– · –), slot with $\tilde{W} = 1/30$; (· · ·), slot with $\tilde{W} = 1/6$;(-×-), slot with $\tilde{W} = 1/3$.

4.5.5. Remarks

The examples given in this section have considered how changes to the FESE model can affect the estimates of the scattering coefficients. The numerical results suggest that scattering coefficients depend on frequency, notch/slot depth and width. Furthermore, wave-mode conversion is significant for large notches/slots at high frequencies.

4.6. Numerical results

4.6.1. Reflection coefficients of a notch

In this section, numerical results for a number of FESE notch models are presented. Fig. 4.18 shows r^{AA} for depths ranging from $\gamma = 0$ to $\gamma = 0.40$ (the values of γ are shown in the figure). When $\gamma = 0$ the model is equivalent to a uniform beam, for which $r^{AA} = 0$. However, as explained in chapter 3, the mis-match between the FE model and SEs causes reflections at the interface boundary, such that $r^{AA} > 0$.

In Fig. 4.18, at low frequencies and when $\gamma = 0.05, 0.10$, the estimated reflection coefficients are of similar order to the errors caused by the mis-match at the interface between the FE and SE models. Above $\gamma = 0.15$, r^{AA} is approximately a factor of 10 larger than when $\gamma = 0$ and it is assumed that the errors are relatively less significant for larger notch depths.

Fig. 4.19 shows r^{AA} for notch depths above $\gamma = 0.40$. In this frequency range, as the depth increases, r^{AA} appears to increase monotonically.

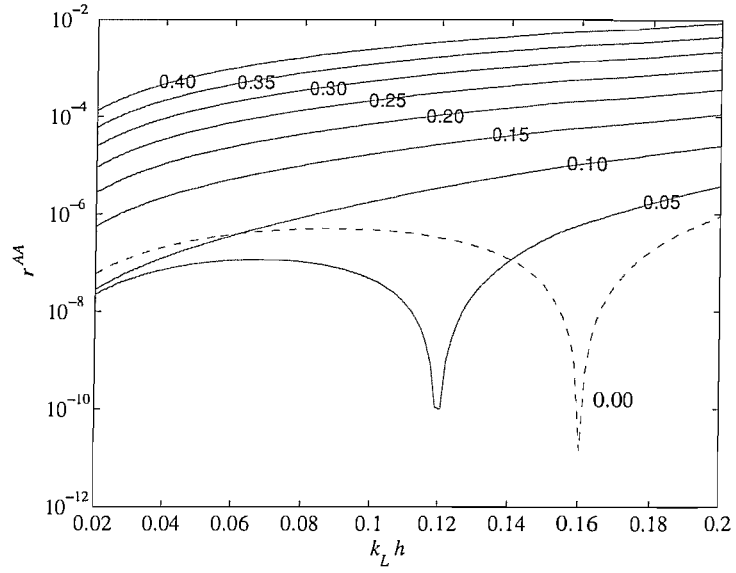

Fig. 4.18: Axial power reflection coefficients r^{AA} for $\gamma = 0.05$ to $\gamma = 0.40$.

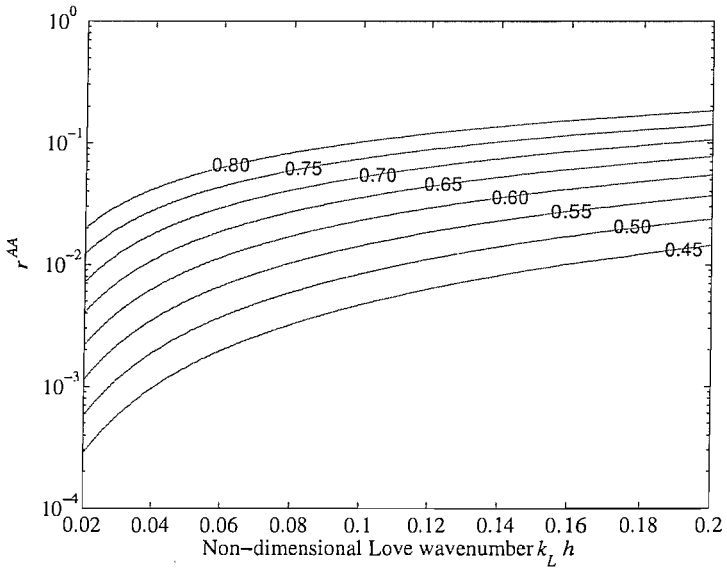

Fig. 4.19: Axial power reflection coefficients r^{AA} for $\gamma = 0.45$ to $\gamma = 0.80$.

Figs. 4.20 and 4.21 show r^{PP} for various notch depths. The values of r^{PP} are larger at any given frequency than r^{AA}. For $\gamma = 0.05$, r^{PP} is again of a similar order to when $\gamma = 0$ and it would appear that the estimate is affected by the mis-match between the models. For $\gamma > 0.10$, the estimates of r^{PP} are a factor of 100 or more larger than those when $\gamma = 0$ and it is assumed that the results from the larger notches are not significantly affected by the modelling errors.

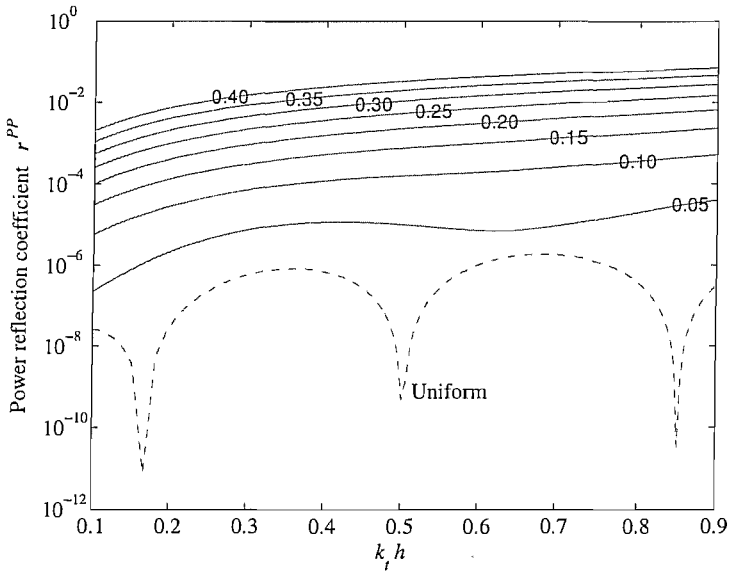

Fig. 4.20: Flexural power reflection coefficients r^{PP} for $\gamma = 0.05$ to $\gamma = 0.40$.

For notches with $\gamma > 0.65$ (Fig. 4.21), it can be seen that r^{PP} noticeably decreases at higher frequencies. A similar result was found in the previous section for slot models with large widths. However, this last example shows that it is difficult to gain insight into the dynamic characteristics that govern the scattering, when using a numerical model. It is difficult to draw conclusions about the parameters that control the scattering of the notch from a FESE model, without further modelling and experimental work.

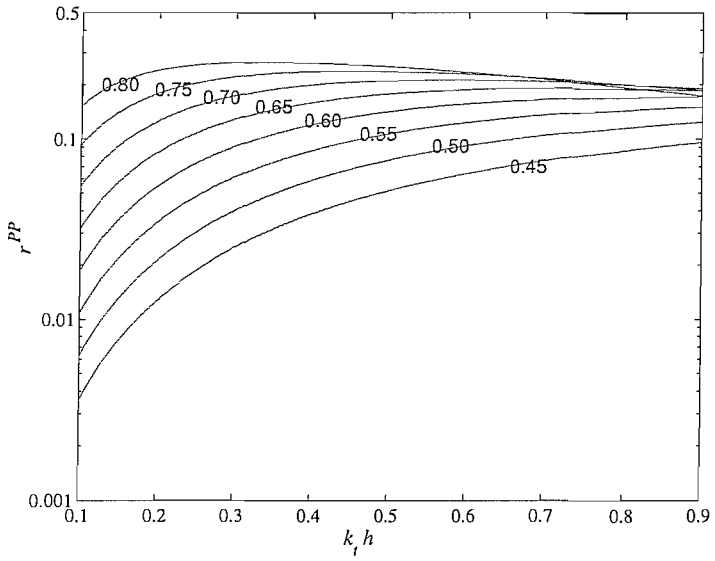

Fig. 4.21: Flexural power reflection coefficients r^{PP} for $\gamma = 0.45$ to $\gamma = 0.80$.

4.6.2. Comparison between notch models

A number of examples have been chosen to illustrate the differences between the lumped spring and FESE notch models. Fig. 4.22 shows that the trend of r^{AA} is similar in both models. However, it is clear that the estimate of r^{AA} from the lumped-spring model is larger than in the FESE model for this frequency range. The lumped-spring does not include wave-mode conversion, such that $r^{AA} + t^{AA} = 1$. However, including wave-mode conversion implies that $r^{AA} + t^{AA} < 1$ (i.e., $r^{AA} + t^{AA} + r^{AP} + t^{AP} = 1$) and it is hence not suprising that the estimates of the reflection coefficients using the lumped-spring model are larger than those of the FESE model.

Fig. 4.23 shows r^{PP} for the lumped-spring and FESE notch models. At low frequencies and for small depths, especially for $\gamma < 0.5$, the predicted reflection coefficients are very similar. For crack depths $\gamma > 0.5$, the estimates of r^{PP} from the spring model appear to increase monotonically with frequency, while the estimates from the FESE models decrease at high frequencies.

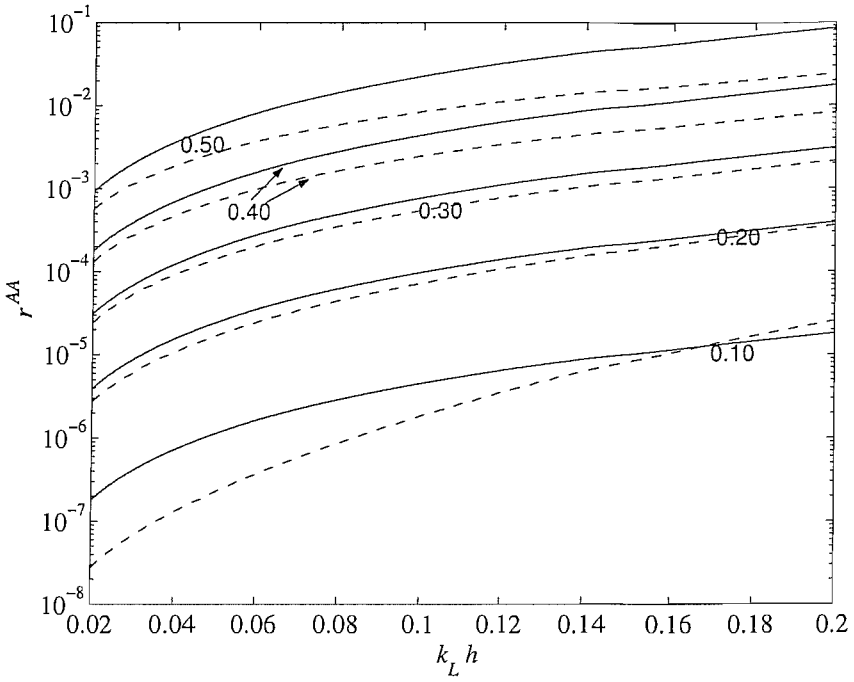

Fig. 4.22: Axial power reflection coefficients r_{AA} for various notch depths.: (—), lumped-spring; (−−), FESE model.

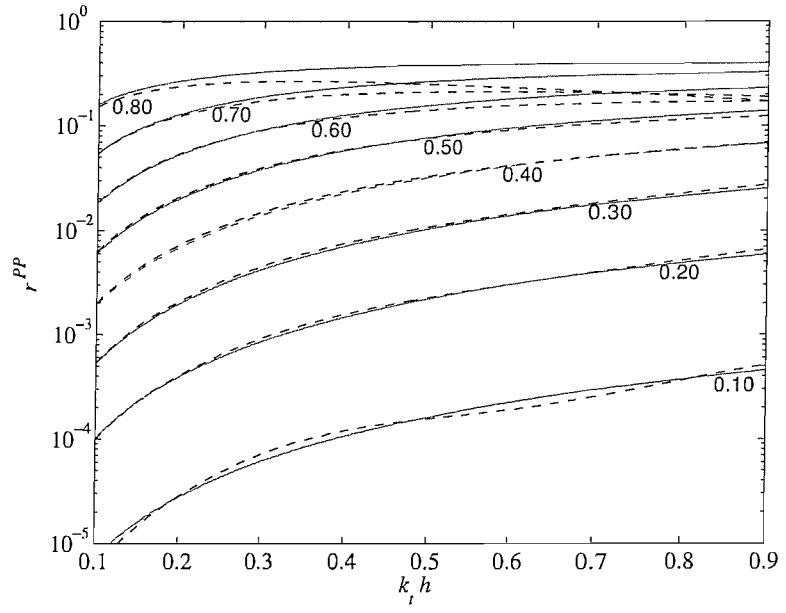

Fig. 4.23: Flexural power reflection coefficients r^{PP} for various notch depths: (—), lumped-spring; (−−), FESE model.

The estimates of r^{PP} from the lumped-spring and FESE models agree reasonably well. However, the lumped-spring model does not include wave-mode conversion (i.e. non-zero $r^{PA,AP}$ and $t^{AP,PA}$), which become particularly significant at high frequencies and large notch depths. In some respects, the similarity between the results of the lumped-spring and FESE notch models might be considered to be coincidental.

4.7. Summary

In this chapter, models for estimating the scattering coefficients of a notch and slot have been considered. The purpose of this modelling is to provide a reference model to which experimental results can be compared. With an accurate model, it might be possible to estimate parameters such as slot depth from experimental measurements.

The analytical lumped-spring notch model has been reviewed and used to predict the scattering coefficients. The lumped-spring model is linear, elastic and the stiffness of each spring is derived from analysis of the strain energy local to the notch. These stiffnesses are derived from the SIF of the notch, assuming that the notch is always open. Furthermore, it was assumed that the depth does not increase as the beam deforms.

Here, a more detailed model has been developed using the FESE method that was described in the previous chapter. The geometry of the notch/slot can be modelled in more detail and the FESE model provides a more accurate description of the wavefield by including behaviour such as wave-mode conversion.

The FESE model is linear, elastic, does not include notch growth and assumes that the notch is open. Numerical results from the FESE models showed that the scattering coefficients depend on frequency, notch depth and width. Furthermore, the FESE model shows that wave-mode conversion is significant, particularly at high frequencies and for

large notch depths. Estimates from the lumped-spring and FESE models are similar at lower frequencies, but noticeable differences arise as the frequency or notch depth increases. However, the advantage of the lumped-spring notch model is that it is a more simple model than the FESE models and might be used as a first estimate of the scattering coefficients.

5. Measuring the scattering coefficients

5.1. Introduction

In this chapter, methods for measuring scattering coefficients on a beam are reviewed. An experiment is described which uses these methods to estimate the scattering coefficients of various attached masses and the results are compared to numerical estimates from FESE models. In the next chapter, these methods are applied to measuring the scattering coefficients of slots in beams.

As in the numerical approach, the scattering coefficients are estimated from the incident, reflected and transmitted waves. Experimentally, the waves are decomposed from the measured response. Methods for wave decomposition are well known and are reviewed here. To decompose the waves, the wavenumber must be known or estimated. The wavenumber can be estimated from theory but the material properties and dimensions are not always known accurately and it is often more reliable to estimate the wavenumber experimentally. Again, there are established ways of doing this and one method is reviewed here.

The experiment comprises a uniform beam, the ends of which are placed in sand to reduce reflections at the boundaries. The beam is excited using an instrumented hammer and accelerometers are used to measure the response. To this beam are attached various masses and the scattering coefficients are estimated.

Measurement errors, such as sensor mis-calibration, affect the accuracy of the results. It is difficult to analyse the effect of error, given the number of variables. Therefore, numerical examples are presented to illustrate some of the issues that can arise.

5.2. Estimating wave number and wave amplitudes

In this section, methods for estimating the wavenumber and wave amplitudes are reviewed. In principle, these methods might be used to decompose axial, flexural and torsional waves, although, the experimental approaches may differ in each case.

From the numerical results given in the previous chapter, the flexural wave reflection coefficients of a crack are larger than those for axial waves. Therefore, the methods described herein focus on the flexural wave motion.

5.2.1. Estimating the flexural wavenumber

The wavenumber can be estimated either by theory or experiment. The material properties of the beam are not always known accurately and a more reliable estimate can be found experimentally.

The wavenumber is estimated using three or more sensors (here, three were used) as illustrated in Fig. 5.1, where Δ is the sensor spacing. Using this method, it is assumed that the damping across the span of the sensors and the contribution of nearfield waves is negligible. To satisfy the latter point, a *rule-of-thumb* is used and, for a given frequency, the sensors are situated at least half a wavelength from any discontinuities in the beam.

The displacement at each sensor in Fig. 5.1 is

$$v_1 = a_+ e^{ik_e\Delta} + a_- e^{-ik_e\Delta} \tag{5.1}$$

$$v_2 = a_+ + a_- \tag{5.2}$$

$$v_3 = a_+ e^{-ik_e\Delta} + a_- e^{ik_e\Delta} \tag{5.3}$$

where v_n is the displacement at the nth sensor, k_e is the experimental flexural wavenumber and a_+ and a_- are the propagating flexural wave amplitudes at $x = 0$ (the superscript p, which was used to denote propagating flexural wave, has been omitted).

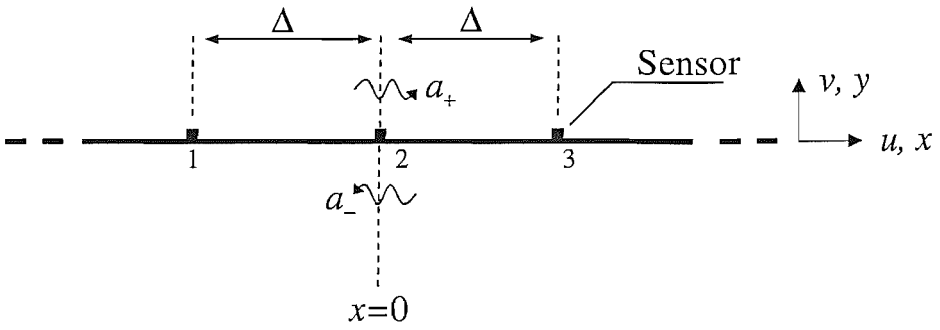

Fig. 5.1: Wavenumber estimation on a beam using three sensors.

By summing Eqs. 5.1 and 5.3, then dividing by Eq. 5.2, it can be shown that

$$\cos(k_e\Delta) = \frac{v_1 + v_3}{2v_2} \tag{5.4}$$

such that the wavenumber is

$$k_e = \frac{1}{\Delta}\cos^{-1}\left(\frac{v_1 + v_3}{2v_2}\right) \tag{5.5}$$

Issues that arise when this method is used in practice will be discussed later.

5.2.2. Wave decomposition

Wave decomposition methods are well established (for example, [61]). In general, the response measured at a set of sensors is described by the wave amplitudes in the form

$$\mathbf{s} = \mathbf{E}\mathbf{a} \tag{5.6}$$

where **s** is a vector of measurements taken at a number of sensors, **a** is a vector of wave amplitudes and **E** is a matrix of terms that describe the wave propagation. If the matrix **E** is square, the wave amplitudes can be estimated from

$$\mathbf{a} = \mathbf{E}^{-1}\mathbf{s} \tag{5.7}$$

If the matrix **E** is over-determined, a pseudo-inverse (in a least-squares sense) can be used to estimate the wave amplitudes by

$$\mathbf{a} = (\mathbf{E}^T\mathbf{E})^{-1}\mathbf{E}^T\mathbf{s} \tag{5.8}$$

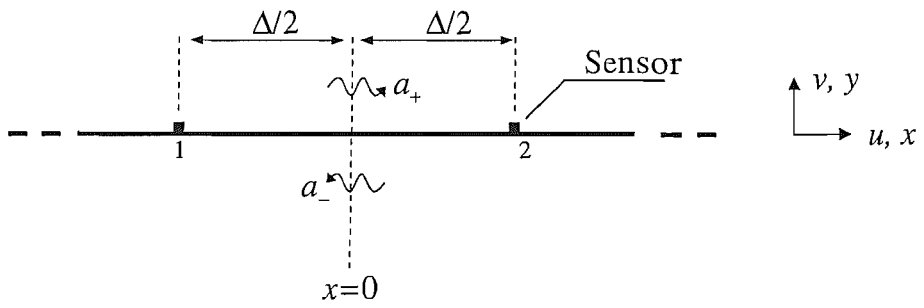

Fig. 5.2: Two sensor setup for wave decomposition.

The propagating flexural waves in a beam can be decomposed using a minimum of two sensors, as illustrated in Fig. 5.2. Again, the nearfield waves and damping are neglected. The displacement at sensors 1 and 2 can be written

$$\begin{Bmatrix} v_1 \\ v_2 \end{Bmatrix} = \mathbf{E}\begin{Bmatrix} a_+ \\ a_- \end{Bmatrix} \quad ; \quad \mathbf{E} = \begin{bmatrix} e^{ik_e\Delta/2} & e^{-ik_e\Delta/2} \\ e^{-ik_e\Delta/2} & e^{ik_e\Delta/2} \end{bmatrix} \tag{5.9}$$

From Eq. 5.9, $\mathbf{a} = \mathbf{E}^{-1}\mathbf{v}$ and the wave amplitudes are

$$a_+ = \frac{1}{2i\sin(k_e\Delta)}\left\{v_1 e^{ik_e\Delta/2} - v_2 e^{-ik_e\Delta/2}\right\} \tag{5.10}$$

$$a_- = \frac{1}{2i\sin(k_e\Delta)}\left\{v_2 e^{ik_e\Delta/2} - v_1 e^{-ik_e\Delta/2}\right\} \tag{5.11}$$

The matrix **E** is singular when $k_e\Delta = \pi$. To avoid the singularity either the spacing or the frequency range must be chosen so that $k_e\Delta < \pi$. The reader is directed to [62] for more discussion about conditioning problems that are encountered with this approach.

5.3. Estimating scattering coefficients

The scattering coefficients are calculated from the incident, reflected and transmitted waves. In a beam, waves can be incident on both sides of the discontinuity and, in general, the scattering coefficients for waves incident on one side of the discontinuity are not equal to those for waves incident on the other side. Considering only the propagating flexural waves, there are two reflection coefficients, R_{11} and R_{22}, and two transmission coefficients T_{12} and T_{21}, where the first number in the subscript denotes which side of the discontinuity the wave is incident upon and the second number denotes the side on which the scattered wave propagates. If $R_{11} = R_{22}$ and $T_{12} = T_{21}$, the discontinuity is said to be symmetric.

To measure the scattering coefficients, the propagating waves are decomposed on either side of the discontinuity using two sensor pairs, as illustrated in Fig. 5.3.

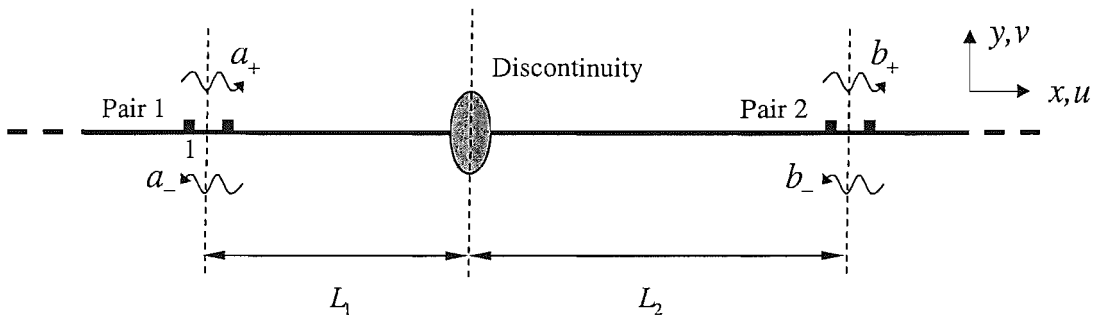

Fig. 5.3: Using two sensor pairs to measure the scattering coefficients.

Neglecting the contribution of nearfield waves and damping, the incident, reflected and transmitted waves are related by

$$a_- = R_{11}e^{-2ik_e L_1}a_+ + T_{21}e^{-ik_e(L_1+L_2)}b_- \tag{5.12}$$

$$b_+ = T_{12}e^{-ik_e(L_1+L_2)}a_+ + R_{22}e^{-2ik_e L_2}b_- \tag{5.13}$$

where L_1 and L_2 are the distances from the centre of the sensor pairs to the centre of the discontinuity and the wave amplitudes are estimated at the centre of each sensor pair. Furthermore, Eqs. 5.12 and 5.13 do not include any effects of wave mode conversion.

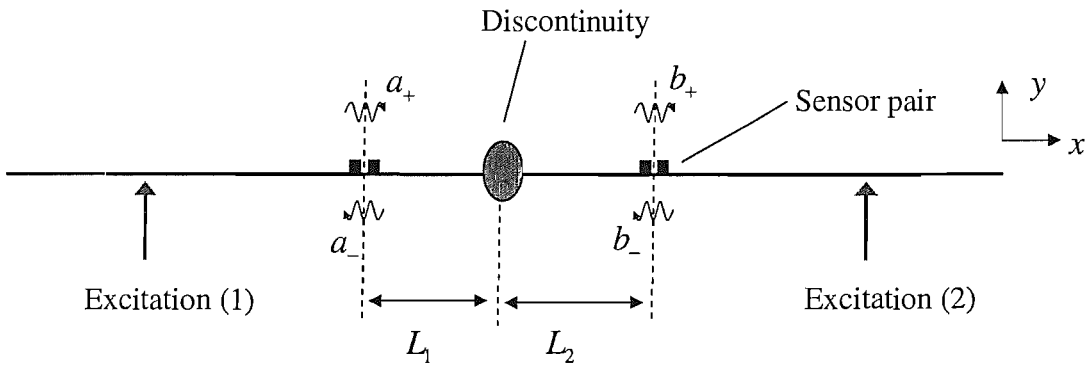

Fig. 5.4: Estimating the scattering coefficients using two excitations.

To estimate the scattering coefficients, the beam is excited on both sides of the discontinuity, as illustrated in Fig. 5.4. The forces must be located outside the span of the sensor pairs and the excitations are not applied at the same time, rather they are applied in turn.

For each excitation we find two equations, in the form of Eqs. 5.12 and 5.13, and these can be written as

$$\begin{bmatrix} a_-^{(1)}e^{ik_eL_1} & b_+^{(1)}e^{ik_eL_2} \\ a_-^{(2)}e^{ik_eL_1} & b_+^{(2)}e^{ik_eL_2} \end{bmatrix} = \begin{bmatrix} a_+^{(1)}e^{-ik_eL_1} & b_-^{(1)}e^{-ik_eL_2} \\ a_+^{(2)}e^{-ik_eL_1} & b_-^{(2)}e^{-ik_eL_2} \end{bmatrix} \begin{bmatrix} R_{11} & T_{12} \\ T_{21} & R_{22} \end{bmatrix} \tag{5.14}$$

where the superscripts (1) and (2) denote the wave amplitudes measured for excitation (1) and (2), respectively. By pre-multiplying the matrix on the left-hand side of Eq. 5.14 by the inverse of the matrix of wave amplitudes on the right-hand side, the measured scattering coefficients can be shown to be

$$R_{11} = \left(\frac{a_-^{(1)}b_-^{(2)} - a_-^{(2)}b_-^{(1)}}{a_+^{(1)}b_-^{(2)} - a_+^{(2)}b_-^{(1)}}\right)e^{2ik_eL_1} \quad ; \quad R_{22} = \left(\frac{a_+^{(1)}b_+^{(2)} - a_+^{(2)}b_+^{(1)}}{a_+^{(1)}b_-^{(2)} - a_+^{(2)}b_-^{(1)}}\right)e^{2ik_eL_2} \tag{5.15}$$

$$T_{12} = \left(\frac{b_+^{(1)}b_-^{(2)} - b_-^{(1)}b_+^{(2)}}{a_+^{(1)}b_-^{(2)} - a_+^{(2)}b_-^{(1)}}\right)e^{ik_e(L_1+L_2)} \quad ; \quad T_{21} = \left(\frac{a_-^{(1)}a_+^{(2)} - a_-^{(2)}a_+^{(1)}}{a_-^{(1)}b_-^{(2)} - a_+^{(2)}b_-^{(1)}}\right)e^{ik_e(L_1+L_2)} \tag{5.16}$$

Eq. 5.14 is poorly-conditioned when $a_+^{(2)}$ and $b_-^{(1)}$ have a similar amplitude to $a_+^{(1)}$ and $b_-^{(2)}$. This can occur when strong reflectors exist outside the span of the sensor pairs, such as the ends of the beam. In this case it is difficult to estimate the scattering coefficients accurately. The problem of conditioning depends on the structure being tested and has been considered in more depth in [62]. Treatment, such as tapered damping, might be applied to the beam to reduce the amplitude of the waves reflecting from discontinuities outside the sensor pairs.

If the location of the discontinuity is unknown, as is usually the case in crack detection, the measured scattering coefficients can be estimated at the sensor pairs. This

is equivalent to letting $L_{1,2} = 0$ in Eqs. 5.15 and 5.16, such that the estimates are

$$\widehat{R}_{11} = R_{11}e^{-2ik_bL_1} \quad ; \quad \widehat{R}_{22} = R_{22}e^{-2ik_bL_2} \tag{5.17}$$

$$\widehat{T}_{12} = T_{12}e^{-ik_b(L_1+L_2)} \quad ; \quad \widehat{T}_{21} = T_{21}e^{-ik_b(L_1+L_2)} \tag{5.18}$$

where $\widehat{\cdot}$ denotes the scattering coefficient estimated at the sensor pairs. It can be seen in Eqs. 5.17 that the difference between $\widehat{R}_{11,22}$ and $R_{11,22}$ is a phase term. Similarly, this is true for the transmission coefficients. The existence of phase terms in the measured scattering coefficients does not affect estimates of the power scattering coefficients, given that

$$r_{11} = |\widehat{R}_{11}|^2 = |R_{11}|^2 \quad ; \quad r_{22} = |\widehat{R}_{22}|^2 = |R_{22}|^2 \tag{5.19}$$

$$t_{12} = |\widehat{T}_{12}|^2 = |T_{12}|^2 \quad ; \quad t_{21} = |\widehat{T}_{21}|^2 = |T_{21}|^2 \tag{5.20}$$

5.4. Experimental setup

A beam that is assumed to be nominally uniform and homogeneous along its length was arranged such that the ends of the beam were partially buried in sand, as illustrated in Fig. 5.5. The sand acts to damp waves that propagate near the ends of the beam. This reduces the amplitude of waves that are reflected from the ends and lessens problems that are associated with ill-conditioning when estimating the scattering coefficients.

Approximately 1m of beam was placed in the sand at each end. The sand is most effective when the wavelength is short compared to this length and, at high frequencies, the response is similar to that of an infinite beam. At low frequencies, when the wavelength is longer than 1m, the waves are not as strongly attenuated by the sand and conditioning problems might persist. Fig. 5.6 shows a diagram of the sandbox from above. The foam wedges were used to keep the sand in place.

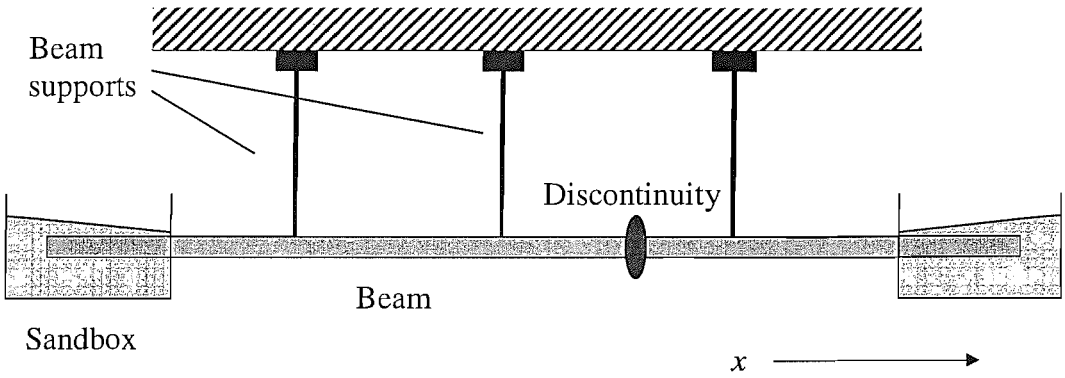

Fig. 5.5: Experimental rig for estimating scattering coefficients on a beam.

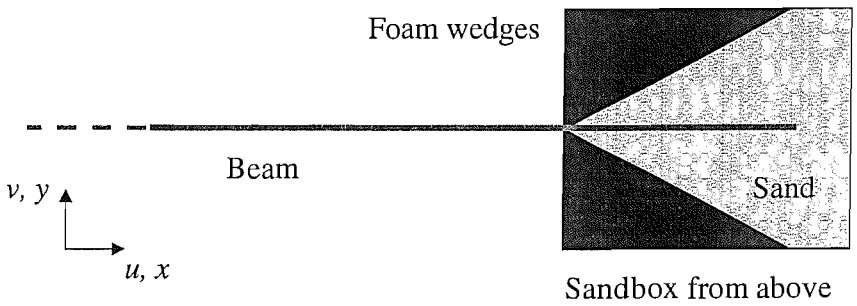

Fig. 5.6: View of the sandbox from above.

Over time, the sand moves as the beam settles. This makes it practically impossible to obtain consistent reflection coefficients from the sandboxes. However, provided that the waves reflecting from the ends of the beam are reduced, the fact that the amount of reflection may vary between experiments should not be a concern.

The reflected wave field from the sand boxes may include axial and torsional waves, as well as flexural waves, because of wave-mode conversion. Furthermore, the sand may introduce some non-linear behaviour. One way to assess the linearity is to measure the coherence between the excitation and the sensor outputs. In all the experimental results given in this chapter, the coherence was found to be close to 1, except at low frequencies where resonances and anti-resonances occur. From this result, it is assumed that any non-linear behaviour caused by the sandboxes is insignificant.

The beam was supported by the sand and three nylon wires, equally spaced along the length of the beam, as illustrated in Fig. 5.5. The nylon wires were tied to the beam through a small hole made at the edge. The holes had a diameter less than 1mm and are much smaller than the discontinuities that were measured. It is assumed that the errors caused by the holes are small in comparison with other sources of error.

Using sandboxes to lessen conditioning problems is not usually a practical solution. Further work could consider other more practical means of reducing these problems.

A number of beams were used in the experiments that are described later. All were mild steel, with the dimensions $b = 0.05$m and $h = 0.006$m. These values are nominally constant over the length of the beam, and the beam was 6m long.

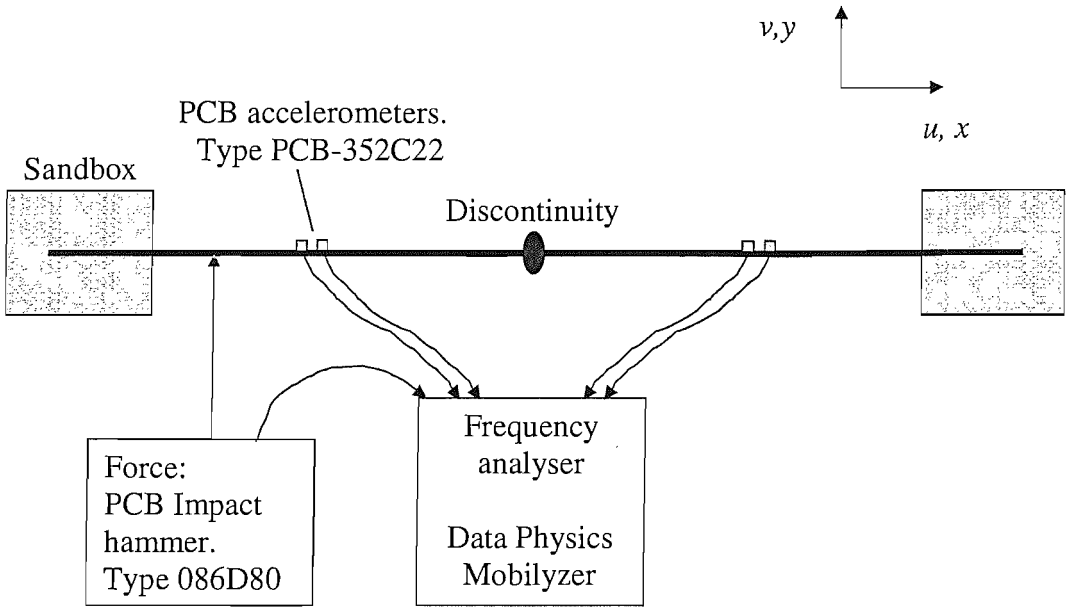

Fig. 5.7: Experimental equipment setup for measuring the vibration on the beam.

Fig. 5.7 shows the experimental equipment used to measure the vibration on the beam. All the signals were processed using the Data Physics analyser and the vibration is measured on the beam using accelerometers PCB-352C22. For a given frequency, the sensors are located at least half a wavelength from any discontinuity so that the nearfield waves are negligible. The beam was excited using a PCB-086D80 impact hammer with a steel tip. Although every effort was made to excite only flexural waves in the beam, it is possible that other wave modes were excited, such as torsion. This may cause some errors in the measured results given that these waves may contribute to the measured response but are not accounted for in the calculations.

5.5. Experimental error

Experimental errors affect the accuracy of the estimated wavenumber, the wave decomposition and the estimates of scattering coefficients. The following lists some of the possible sources of error that are thought to affect the accuracy of the experimental work:

- sensor mis-calibration;
- noise;
- estimation of wavenumber;
- conditioning problems;
- measurement errors (errors in the experimental setup);
- assumptions in the formulation;
- inhomogeneity in the beams;
- nylon wire support holes; and
- non-linear response of the sandboxes.

Some of these sources of error have been mentioned earlier, such as conditioning problems, assumptions in the formulations (i.e., negligible nearfields and damping), the non-linear response of the sandboxes and the support holes.

5.5.1. The effect of sensor mis-calibration errors

It is impossible to analyse the overall effect that all possible causes of experimental error have on the estimates of the scattering coefficients. In the following, the specific issue of

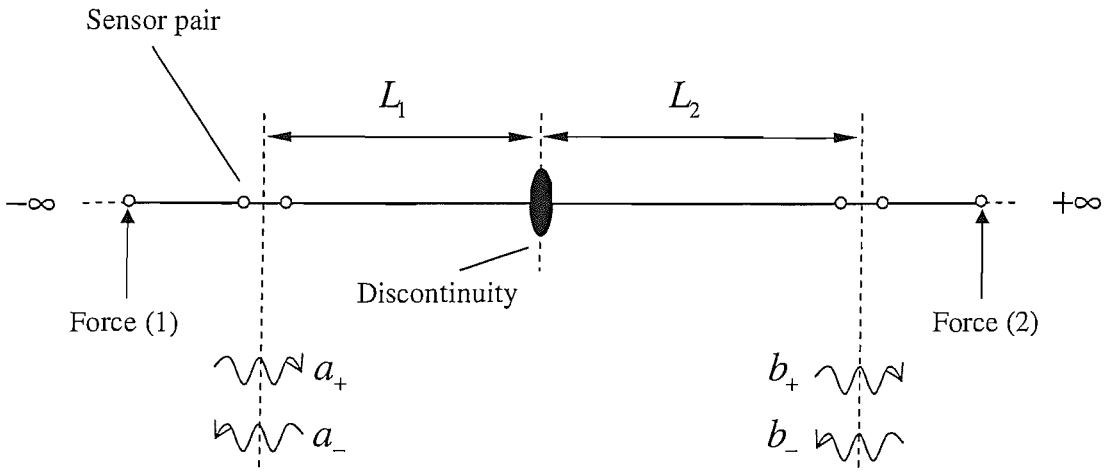

Fig. 5.8: Beam model of an infinite uniform beam.

mis-calibration error is illustrated. This example offers some insight into the result of having errors on the measured response when estimating the scattering coefficients.

Fig. 5.8 shows an infinite beam with a discontinuity, two forces and two sensor pairs This model is used to simulate the experiment in noise free conditions. For this example, it is assumed that k_e is known exactly.

Suppose that the beam is excited by force (1) and there are no errors in the estimation. Given that the beam is infinite, $b_-^{(1)} = 0$ and the displacement at each sensor is

$$v_1 = a_+^{(1)} e^{ik_e\Delta/2} + a_-^{(1)} e^{-ik_e\Delta/2} \;\; ; \;\; v_2 = a_+^{(1)} e^{-ik_e\Delta/2} + a_-^{(1)} e^{ik_e\Delta/2} \tag{5.21}$$

$$v_3 = b_+^{(1)} e^{ik_e\Delta/2} \;\; ; \;\; v_4 = b_+^{(1)} e^{-ik_e\Delta/2} \tag{5.22}$$

Therefore, by Eq. 5.9, the wave amplitudes at the sensor pairs are

$$a_+^{(1)} = \frac{v_1 e^{ik_e\Delta/2} - v_2 e^{-ik_e\Delta/2}}{2i\sin(k_e\Delta)} \;\; ; \;\; a_-^{(1)} = \frac{v_2 e^{ik_e\Delta/2} - v_1 e^{-ik_e\Delta/2}}{2i\sin(k_e\Delta)} \tag{5.23}$$

$$b_+^{(1)} = \frac{v_3 e^{ik_e\Delta/2} - v_4 e^{-ik_e\Delta/2}}{2i\sin(k_e\Delta)} \;\; ; \;\; b_-^{(1)} = 0 \tag{5.24}$$

The reflection and transmission coefficients of the discontinuity, measured at the sensor pairs, are

$$\widehat{R}_{11} = \frac{a_-^{(1)}}{a_+^{(1)}} \;;\; \widehat{T}_{12} = \frac{b_+^{(1)}}{a_+^{(1)}} \tag{5.25}$$

To simulate a mis-calibration error on sensor 1, v_1 is multiplied by a factor $(1 + \epsilon_1)$, where ϵ_1 is the error and may be complex. For excitation by force (1), only $a_+^{(1)}$ and $a_-^{(1)}$ are affected by the error. From Eq. 5.23, the erroneous wave amplitude estimates are

$$\tilde{a}_+^{(1)} = \frac{v_1(1+\epsilon_1)e^{ik_e\Delta/2} - v_2 e^{-ik_e\Delta/2}}{2i\sin(k_e\Delta)} = a_+^{(1)} + \epsilon_1\left(\frac{[a_-^{(1)} + a_+^{(1)}e^{ik_e\Delta}]}{2i\sin(k_e\Delta)}\right) \tag{5.26}$$

$$\tilde{a}_-^{(1)} = \frac{v_2 e^{ik_e\Delta/2} - v_1(1+\epsilon_1)e^{-ik_e\Delta/2}}{2i\sin(k_e\Delta)} = a_-^{(1)} - \epsilon_1\left(\frac{[a_+^{(1)} + a_-^{(1)}e^{-ik_e\Delta}]}{2i\sin(k_e\Delta)}\right) \tag{5.27}$$

where $\tilde{}$ denotes a variable subjected to error.

Having included the error, the estimates of the reflection and transmission coefficients in Eq. 5.25 are

$$\tilde{R}_{11} = \frac{\tilde{a}_-^{(1)}}{\tilde{a}_+^{(1)}} \;;\; \tilde{T}_{12} = \frac{b_+^{(1)}}{\tilde{a}_+^{(1)}} \tag{5.28}$$

From Eqs. 5.26, 5.27, and 5.24, the reflection and transmission coefficients in Eq. 5.28 can be shown to be

$$\tilde{R}_{11} = \widehat{R}_{11} - \epsilon_1\left(\frac{1 + \widehat{R}_{11}\left[2\cos(k_e\Delta) + \widehat{R}_{11}\right]}{2i\sin(k_e\Delta) + \epsilon_1\left[e^{ik_e\Delta} + \widehat{R}_{11}\right]}\right) \tag{5.29}$$

$$\tilde{T}_{12} = \widehat{T}_{12} - \epsilon_1\left(\frac{\widehat{T}_{12}\left[e^{ik_e\Delta} + \widehat{R}_{11}\right]}{2i\sin(k_e\Delta) + \epsilon_1\left[e^{ik_e\Delta} + \widehat{R}_{11}\right]}\right) \tag{5.30}$$

Eqs. 5.29 and 5.30 show that the inclusion of error creates a second term that depends on the size of the error, the wavenumber and the correct values of the scattering

coefficients. At low frequencies, the true behaviour of the scattering coefficients is often such that $\left|\widehat{R}_{11}\right| \to 0$ and $\left|\widehat{T}_{21}\right| \to 1$ as $\omega \to 0$. However, with the error included, as $\omega \to 0$, $\left|\tilde{R}_{11}\right| \to 1$ and $\left|\tilde{T}_{12}\right| \to 0$. This result suggests that the effect of the mis-calibration error is very significant at low frequencies.

The errors are different when exciting the beam with force (2). In theory, $a_+^{(2)} = 0$ for the infinite beam. However, by including errors on sensor 1, it is found that

$$\tilde{a}_+^{(2)} = a_+^{(2)} + \epsilon_1 \left(\frac{[a_-^{(2)} + a_+^{(2)} e^{ik_e\Delta}]}{2i \sin(k_e\Delta)} \right) \tag{5.31}$$

Setting $a_+^{(2)} = 0$, it follows that

$$\tilde{a}_+^{(2)} = \frac{\epsilon_1 a_-^{(2)}}{2i \sin(k_e\Delta)} \tag{5.32}$$

This is only equal to zero, when $\epsilon_1 = 0$, i.e., no error, or $a_-^{(2)} = 0$, i.e., when the transmission coefficient of the discontinuity is equal to zero.

It can also be shown that errors in wavenumber or Δ have some similarity with the effects seen for mis-calibration. A more complex scenario, for example where the beam is finite and errors exist on all sensor outputs and on the wavenumber estimate, can be expected to produce similar but compounded inaccuracies.

5.5.2. Numerical example

The infinite beam model, shown in Fig. 5.8, is used to simulate the experiment, in which the discontinuity is a point mass with $m = 0.5$kg (chapter 3, § 3.4.1) and the simulation does not include noise. The response of the beam is modelled using TBT, where $E = 210 \times 10^9 \text{Nm}^{-2}$, $\rho = 7850\text{kgm}^{-3}$, $\upsilon = 0.3$ and $h = 0.006$m. The point mass is symmetric and $L_1 = L_2$, so that $\widehat{R}_{11} = \widehat{R}_{22}$ and $\widehat{T}_{12} = \widehat{T}_{21}$. A calibration error is simulated by multiplying v_1 by a factor of 1.05. The estimated power scattering coefficients are presented in Fig. 5.9 as a function of non-dimensional Timoshenko wavenumber.

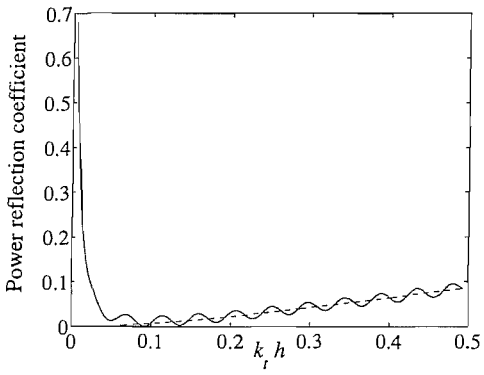

(a) Estimated reflection coefficients: (––), $r_{11,22}$ exact; (—), r_{11} with error; (– · –), r_{22} with error.

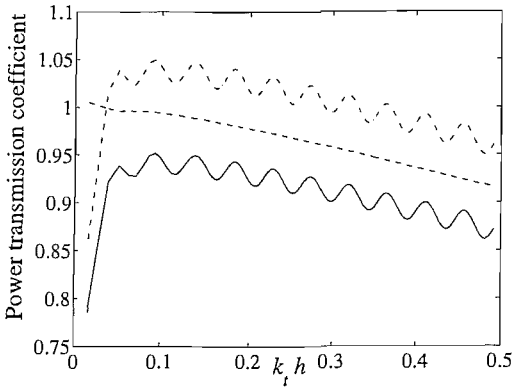

(b) Estimated transmission coefficients: (––), $r_{11,22}$ exact; (—), r_{11} with error; (– · –), r_{22} with error.

Fig. 5.9: Estimated reflection and transmission coefficients with a simulated mis-calibration error on the output of sensor 1.

The results in Fig. 5.9 clearly show that the error in the estimates is significant at low wavenumbers. Also, there would appear to be no difference between the erroneous estimates of r_{11} and r_{22} when $L_1 = L_2$ and the scatterer is symmetric. Two other important features are the modulation apparent in all the estimated scattering coefficients and the fact that the coefficients do not satisfy the conditions of conservation of energy, i.e., $r_{11} + t_{12} \neq 1$ and $r_{22} + t_{21} \neq 1$. The modulation in the results is related to the second terms on the right-hand side of Eqs. 5.29 and 5.30. The frequency of the modulation is related to the distances L_1 and L_2. From these results it appears that the reflection coefficient provides the better estimate, as it appears to modulate approximately about the exact value, except at low wavenumbers.

5.6. Experimental results

In this section, results are presented to give experimental examples of wavenumber estimation, wave decomposition, and the estimation of scattering coefficients. Using the experimental setup, described earlier in this chapter, the scattering coefficients are estimated for various masses that were attached to the beam. The measured scattering coefficients are then compared to numerical estimates that have been found using FESE models of the masses.

5.6.1. Estimating the wavenumber

The wavenumber was estimated using the method described in § 5.2.1. Three accelerometers were placed along the centre-line of a uniform section of beam. The response was measured in terms of accelerence μ (acceleration per unit force). Therefore, replacing displacement in Eq. 5.5 with accelerence, the wavenumber estimate is

$$\widehat{k_e} = \frac{1}{\Delta}\cos^{-1}\left(\frac{\mu_1 + \mu_3}{2\mu_2}\right) \tag{5.33}$$

where the subscript on the variable μ denotes the accelerometer number, $\widehat{k_e}$ is the experimental estimate of the wavenumber k_e and $\Delta = 0.02\text{m}$.

The wavelengths in the experiment were much longer than the dimensions of the cross-section. From EBT it is expected that $\widehat{k_e} \propto \sqrt{f}$. The real part of the measured wavenumber is shown as a function $\sqrt{f}$ in Fig. 5.10. As can be seen from Fig. 5.10, at higher frequencies, the estimate appears to be a linear function of $\sqrt{f}$ as expected. At lower frequencies it is thought that experimental errors affect the wavenumber estimate. From numerical simulations, not given here, it was found that errors caused by sensor mis-calibration are significant when $(\mu_1 + \mu_3)/2\mu_2$ is close to 1 and when the wavelength is much longer than the sensor spacing.

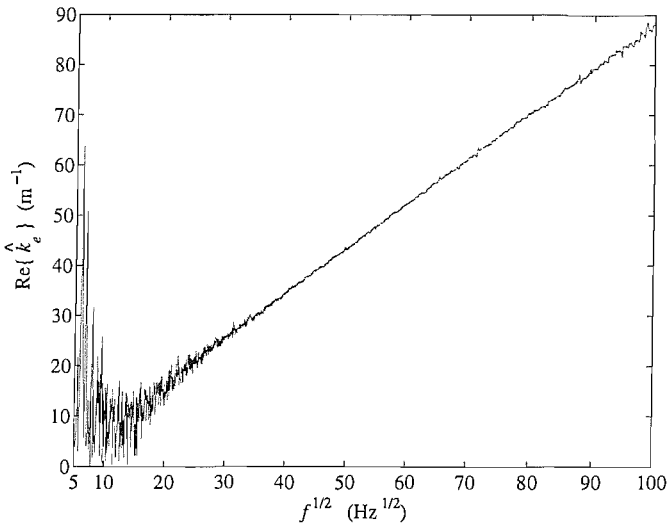

Fig. 5.10: Estimated wavenumber $\widehat{k_e}$.

The imaginary part of the experimental estimate might suggest damping but it was found to be much larger than would be expected were it solely a result of damping. Numerical calculation of the inverse cosine in Eq. 5.33 can lead to a complex result if $(\mu_1 + \mu_3)/2\mu_2 > 1$ and this can result from errors such as sensor mis-calibration. This issue is a particular problem if $\cos(\widehat{k_e}\Delta)$ is close to unity. As a result, errors in the imaginary part can be more prominent when Δ is very much smaller than the wavelength at a given frequency. The level of damping can be assessed by considering the attenuation per unit length, which is calculated from the imaginary part of the estimated wavenumber and given by

$$Atten. = 20\log_{10}\left(\frac{e^{\widehat{k}_{IM}}}{e^0}\right) \tag{5.34}$$

where the reference e^0 denotes no attenuation and $\widehat{k}_{IM}$ is the imaginary part of the experimental wavenumber. The attenuation is shown in Fig. 5.11. It can be seen that at low frequencies the attenuation is positive and this type of error can occur whenever the $(\mu_1 + \mu_3)/2\mu_2 > 1$. Furthermore, there is a noticeable modulation that occurs above

1000Hz. Modulation can occur in the accelerence as a result of wave interference that occurs due to waves reflecting from the slot and from the ends of the beam. It is thought that this effect contributes to the modulation seen in Fig. 5.11 but, without further investigation into the experimental errors, it can not be considered to be the sole cause.

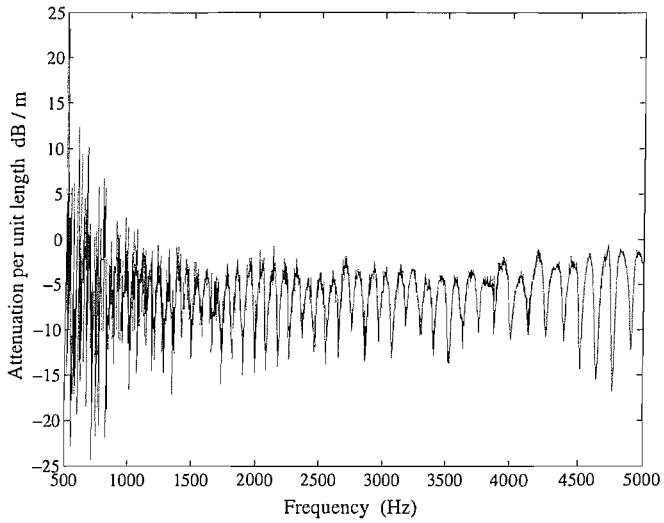

Fig. 5.11: Attenuation per unit length.

Any experimental error in $\widehat{k_e}$ will increase the errors in the wave decomposition. In an attempt to reduce the possible effects that errors in the wavenumber estimate may have on further calculations, a curve was fitted to the estimate $\widehat{k_e}$ to find an expression for the wavenumber. From EBT, it is assumed that

$$k_e = B_e \sqrt{f} \tag{5.35}$$

The constant B_e can be estimated from $\widehat{k_e}$ by applying a least-squares fit to the measured

data, such that

$$B_e = \frac{\sum_{j=1}^{J} w_j \, \widehat{k}_{e,j} \sqrt{f_j}}{\sum_{j=1}^{J} w_j^2 \, f_j} \tag{5.36}$$

where w_j is a weighting of the data at the jth frequency. The weighting can be used to discard results at certain frequencies (by setting $w_j = 0$) and might be used to increase the significance of the results at other frequencies. Doing so may improve the estimate of B_e. For the result in Fig. 5.10, all frequencies below $\sqrt{f} = 20$ are discarded, to reduce some of the the errors in $\widehat{k}_e$, and B_e is calculated from the remaining data. It is then assumed that the value of B_e is true for all frequencies.

From this point forward, the terms "measured wavenumber" or "experimental wavenumber" refer to k_e as calculated from the least-squares fit to the experimental data.

5.6.2. Uniform beam

The scattering coefficients of a uniform length of beam were measured experimentally and the results are presented here. Theoretically, the power reflection and transmission coefficients of a uniform section of beam are $r_{11,22} = 0$ and $t_{12,21} = 1$.

The waves are decomposed from measurements of the accelerance, with a sensor spacing of $\Delta = 0.02$m. Eq. 5.9 can be written in terms of accelerance as

$$\begin{Bmatrix} \mu_1 \\ \mu_2 \end{Bmatrix} = -\omega^2 \begin{bmatrix} e^{ik_e\Delta/2} & e^{-ik_e\Delta/2} \\ e^{-ik_e\Delta/2} & e^{ik_e\Delta/2} \end{bmatrix} \begin{Bmatrix} a_+ \\ a_- \end{Bmatrix} \tag{5.37}$$

Fig 5.12 shows the power reflection coefficients $r_{11,22}$ of the uniform length. As a result of experimental errors and noise, $r_{11,22} \neq 0$. The errors appear worse at low frequencies, perhaps resulting from sensor mis-calibration errors and conditioning errors

that are caused by large reflections from outside the span of the sensor pairs. In this example, r_{22} appears less accurate than r_{11}.

The result in Fig. 5.12 can be considered to be the noise floor in future measurements. If a discontinuity has reflection coefficients that are of a similar order to the noise floor, these measurements may be less accurate and more susceptible to the effects of error.

Fig. 5.13 shows the power transmission coefficients for the uniform beam. Both results are close to 1 at lower frequencies, although they are inaccurate at very low frequencies owing to errors caused by strong resonances and conditioning problems. At higher frequencies the transmission coefficients deviate about 1 though, on the whole, the estimates appear to be less than 1. Again, the accuracy of the measurement appears to be worse at low frequencies for the reasons given previously. Given the effect that errors such as sensor mis-calibration have on the transmission coefficients, as shown by these measured results and the numerical example in § 5.5.2, it is decided to concentrate on the reflection coefficients for all further measurements.

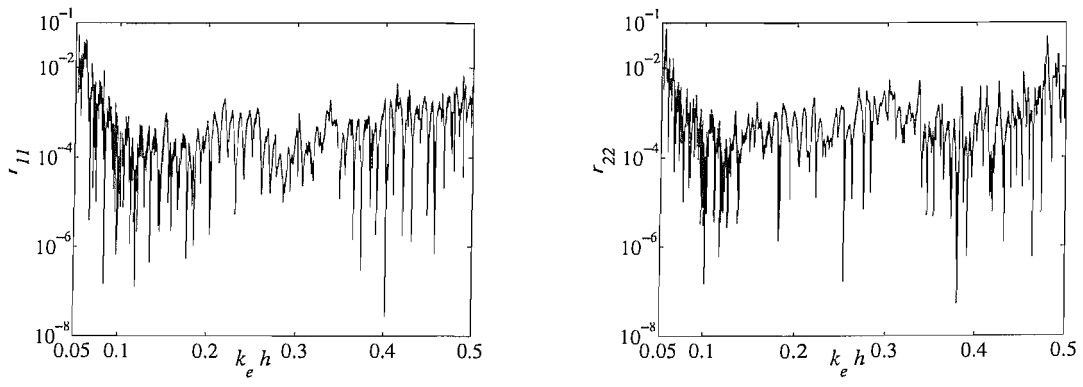

(a) r_{11}. *(b)* r_{22}.

Fig. 5.12: Measured reflection coefficients for a uniform length of beam.

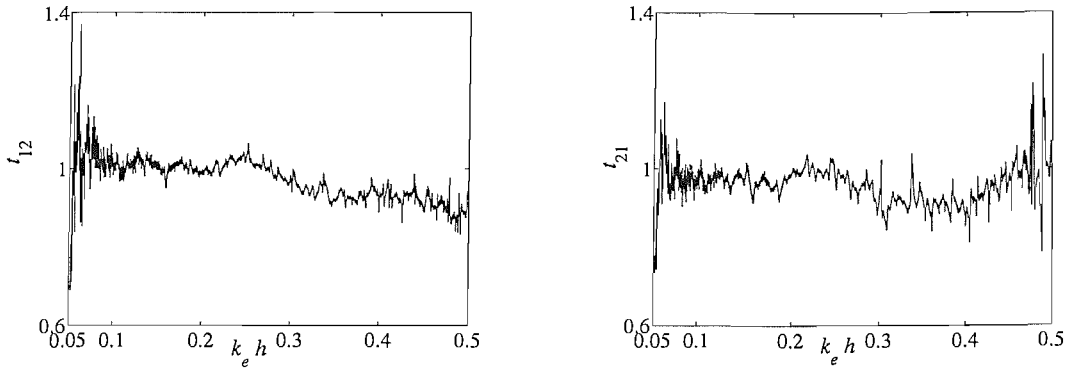

(a) t_{12}. *(b)* t_{21}.

Fig. 5.13: Measured transmission coefficients for a uniform beam.

5.6.3. Attached mass

A number of experiments were performed to estimate the scattering coefficients of various masses that were attached to the uniform beam and the results are presented here. For each mass the scattering coefficients were predicted numerically using a FESE model for comparison with the measured values.

The masses were made from mild steel and the density was estimated to be approximately ρ = 7800kgm^{-3}. In each experiment, two masses with the same dimensions were bonded, using superglue, to the surface on each side of the beam, as shown in Fig. 5.14. Three experiments were performed with three different sizes of mass and their dimensions are given in Table 5.1 and depicted in Fig. 5.14.

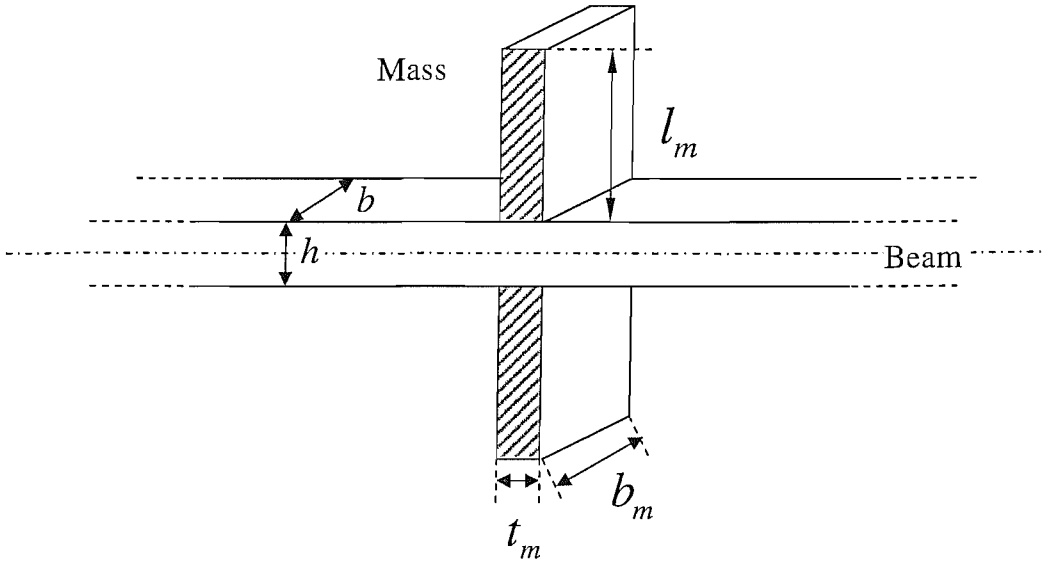

Fig. 5.14: Schematic of the mass discontinuity.

Mass number	(l_m, b_m, t_m)(mm)
1	(40, 50, 10)
2	(30, 50, 10)
3	(30, 50, 20)

Table 5.1: Dimensions of the mass discontinuites.

5.6.4. FESE model of the attached masses

The SE model of the mass was developed using a plane-stress FE model of a section of the beam containing the mass, as shown in Fig. 5.15. Given that this is a plane-stress model, $b_m = 1$.

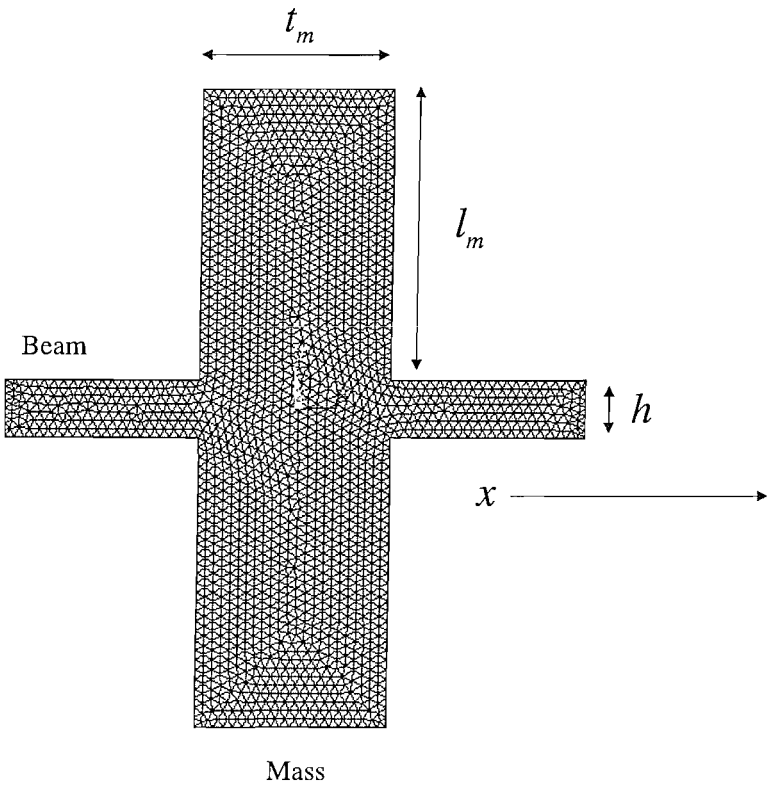

Fig. 5.15: FE model of a beam section with an attached mass.

The Young's modulus of the mass is taken to be that of the beam. In the frequency range of interest, the mass is effectively rigid and its translational and rotational inertia are thought to be important.

In order to create the FESE model, the material properties of the beam must be known, so that the numerical and experimental wavenumbers are approximately equal.

By taking a sample of the beam and measuring its mass and dimensions, the density was estimated. This was found to be approximately 7700kgm^{-3}. The value of E was then estimated from the wavenumber. From EBT, the wavenumber is

$$k_e = \sqrt[4]{\left(\frac{\rho A}{EI}\right)}\sqrt{\omega} \tag{5.38}$$

Using Eq. 5.35, it can be shown that the estimate of E is

$$E = \frac{4\pi^2 \rho A}{I B_e^4} \tag{5.39}$$

where B_e is given by Eq. 5.36. This approach depends on the availability of a sample. For the beam specimens, E was found to be approximately 185GNm^{-2}.

5.6.5. Results and discussion

The scattering coefficients of each mass were estimated using the approach described in § 5.3. The results in Figs. 5.16 to 5.18 show the measured power reflection coefficients for each mass alongside the value predicted by the FESE models.

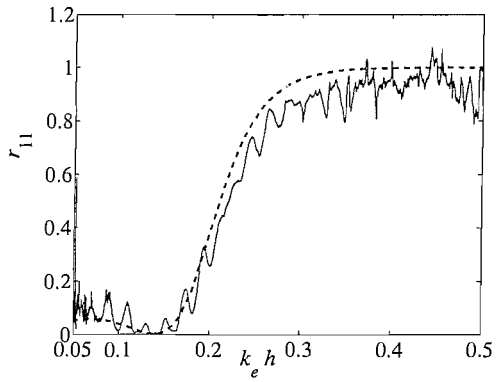

(a) Power reflection coefficient r_{11}: (––), FESE model; (—), r_{11} measured.

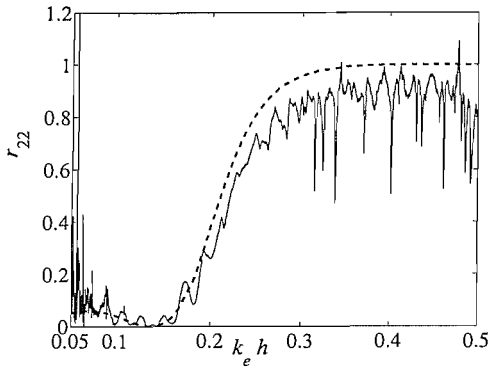

(b) Power reflection coefficient r_{22}: (––), FESE model; (—), measured.

Fig. 5.16: Measured and predicted power reflection coefficients of mass 1.

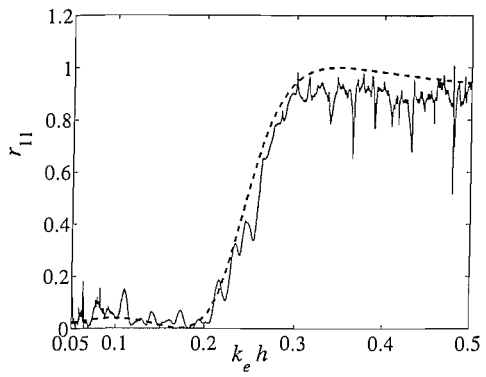

(a) Power reflection coefficient r_{11}: (−−), FESE model; (—), r_{11} measured.

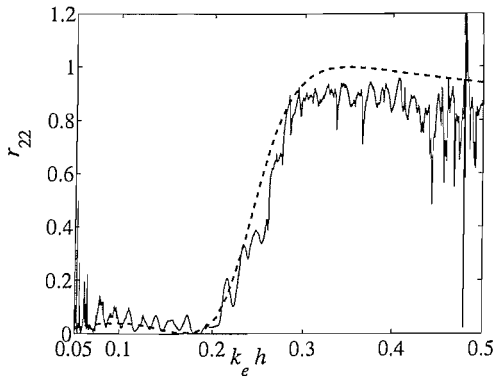

(b) Power reflection coefficient r_{22}: (−−), FESE model; (—), measured.

Fig. 5.17: Measured and predicted power reflection coefficients of mass 2.

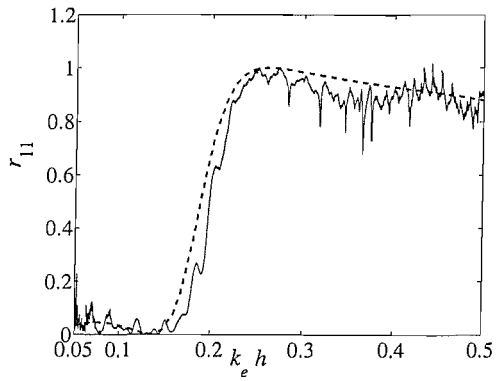

(a) Power reflection coefficient r_{11}: (−−), FESE model; (—), r_{11} measured.

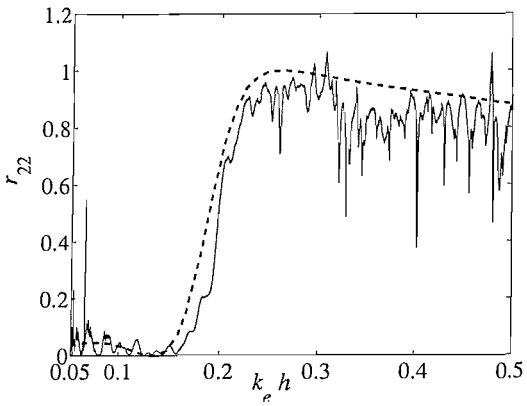

(b) Power reflection coefficient r_{22}: (−−), FESE model; (—), measured.

Fig. 5.18: Measured and predicted power reflection coefficients of mass 3.

Figs. 5.16 to 5.17 show good agreement between the estimates of the FESE models at low and mid-frequencies in the range of interest. At higher frequencies the experimental results have a "jagged" appearance which may be due to the manner in which the masses are glued to the beam. Moreover, although the masses were mounted so that the discontinuity was roughly symmetrical, some error in the mounting is likely to exist, which may cause wave-mode conversion at the mass. The effects of wave-mode conversion are thought to be more significant at higher frequencies. At low frequencies, ill-conditioning causes errors in the results due to strong resonances in the beam. Also, the results show a noticeable modulation, similar to that seen in the numerical example considered in § 5.5.2, and this is thought to result from sensor mis-calibration and possibly errors in wavenumber estimation.

5.7. Summary

Methods for measuring the wavenumber, wave amplitudes and scattering coefficients have been reviewed. An experimental beam rig has been described and used to measure the scattering coefficients of a uniform length of beam and various masses that were attached to the beam.

Experimental error plays a significant role in the accuracy of the estimated scattering coefficients. The accuracy is, for example, affected by sensor mis-calibration, errors in the estimate of wavenumber, conditioning problems caused by large reflections from outside the sensor pairs, and noise.

It is difficult to quantify the errors as there are many sources and variables to consider. However, some numerical examples were used here to illustrate how the results can be affected. At low frequencies, the estimates of the scattering coefficients are less accurate

due to noise, sensor mis-calibration and conditioning problems. From mid-high frequencies, the estimates exhibit modulation, which is believed to be caused by mis-calibration and errors in the wavenumber estimation.

Noise can cause significant error whenever the scattering coefficient is comparatively small. This was illustrated in the estimates of the scattering coefficients for a uniform length of beam.

The experimental results for the masses compare well with the FESE models, particularly at low-mid frequencies. This result offers some validation of the FESE method as a tool for predicting the scattering coefficients.

In the following chapter, the experimental methods that were described here are used to measure the scattering coefficients of a number of beams with slots.

6. Measuring the scattering coefficients of slots

6.1. Introduction

In this chapter, the scattering coefficients of a number of damaged beams are measured and the results presented. The beams are damaged by cutting narrow slots through the width. The experimental method follows that described in chapter 5 and the beams have slots in the range $\gamma = 0.10$ to $\gamma = 0.70$. If the scattering from the slots can be distinguished, the results might be used to suggest the existence of the damage and possibly to estimate the depth of the slot.

The measured scattering coefficients are compared with FESE models, which were described in chapter 4. The comparison is used to illustrate how the FESE models might be used to estimate the slot depth. This approach is expanded in chapter 7.

6.2. Experimental setup

6.2.1. Making the slot

The beams used for the slot experiments have similar material properties and dimensions to those used for the attached masses (chapter 5 § 5.6.3). The undamaged beams are assumed to be homogeneous and isotropic, with uniform dimensions along the length. Seven beams were damaged by cutting a single slot through the cross section. The slots were cut by hand using a mitre saw with a blade that was 1mm thick. The blade of the mitre saw was set normal to the edge of the beam and the cut made across the width of

the beam, as illustrated in Fig. 6.1.

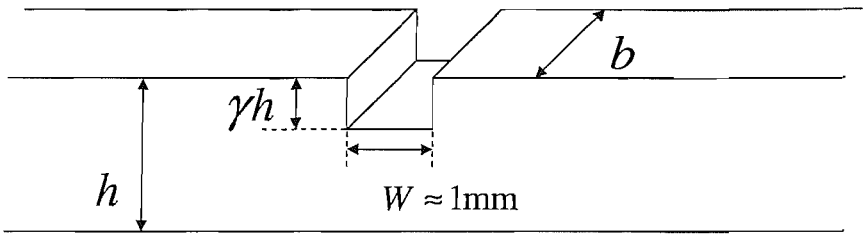

Fig. 6.1: Illustration of the slot that was cut in the beam.

A more uniform depth may have been achieveable by machining the slot; however, the length of the beams made this impractical and the available machine saw widths were larger than 1mm.

It was difficult to cut the slot to a specific depth. Every effort was made to ensure that the depth of the slot was uniform along the width of the cross section, although undoubtedly some non-uniformities arose.

6.2.2. Measuring slot depth

In total, 7 specimens were created, with a single slot cut in each, where the depths ranged from $\gamma = 0.10$ to $\gamma = 0.70$. The slot was not wide enough to measure using standard vernier depth gauges, therefore an *ad hoc.* method was used.

A thin steel ruler was inserted into the slot as illustrated in Fig. 6.2. Two steel blocks lay flush to the beam on either side of the ruler and, when in place the blocks were clamped to the ruler. This assembly was then removed from the slot and the depth of the slot was estimated by measuring the distance from the end of the ruler to the steel blocks

with a vernier gauge, which had an accuracy of ±0.02mm. The depth of the slot was measured at 6 points along the width of the cross-section. Each measurement was repeated 3 times and the average of all values was taken to find a single value for the depth. It was found that the depth of the slot varied slightly over the width. The variation was typically less than 0.15mm (or $\gamma = 0.025$) and often the error was worse towards the edges, owing to the cutting technique.

The average slot depth for each specimen is given in Table 6.1. The values of γ in Table 6.1 are approximate but, in the following, the specimens are referred to by these values, e.g. *'...specimen with* $\gamma = 0.22$*.'*.

6.3. Results

The scattering coefficients of the slots were measured for each specimen in Table 6.1 and the results are presented in this section. Each result is plotted alongside numerical

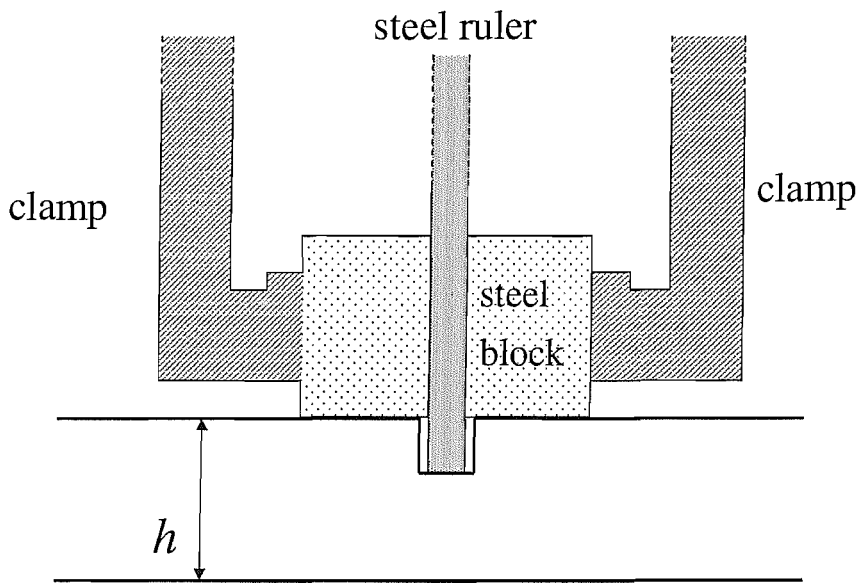

Fig. 6.2: Measuring the depth of the slot.

Specimen	(1)	(2)	(3)	(4)	(5)	(6)	(7)
Average γ	0.13	0.22	0.34	0.39	0.50	0.55	0.62

Table 6.1: Measured slot depths.

predictions from FESE models of the slot, modelled with a width of $W/h = 1/6$ (or $W = 1\text{mm}$). The wavenumber of each specimen was estimated as described in chapter 5, § 5.6.1. The wavenumber estimates of all the specimens were roughly $k_e = 0.86\sqrt{f}$. Samples of the beams were taken to estimate the densities and these were found to be approximately $\rho = 7700\text{kgm}^{-3}$ for each specimen. The Youngs modulus E was estimated from the wavenumbers, using Eq. 5.39 (chapter 5), and was found to be around $E = 185\text{GNm}^{-2}$ for each specimen.

In the interests of clarity, only the power reflection coefficients, r_{11}, for waves incident from the left-hand side of the slot, are plotted for each specimen given that it was found that r_{22} was very similar. The main difference between the two is that the modulation in each result has a different frequency and this is due to the difference in the distance from each of the sensor pairs to the slot.

Fig. 6.3 shows a comparison between measured values of r_{11} for a uniform undamaged length of beam (see chapter 5, § 5.6.2) and those measured on a damaged specimen with $\gamma = 0.13$. It is difficult to discern between the measurements, which shows that the reflections from the slot are of the same order as the errors and noise in the experiment. The slot is perhaps noticeable at higher frequencies, though this is not clear. Experimental errors make it difficult to learn much from this result and one can not be sure that a slot is present.

The measured reflection coefficients for the other specimens are presented in Figs. 6.4

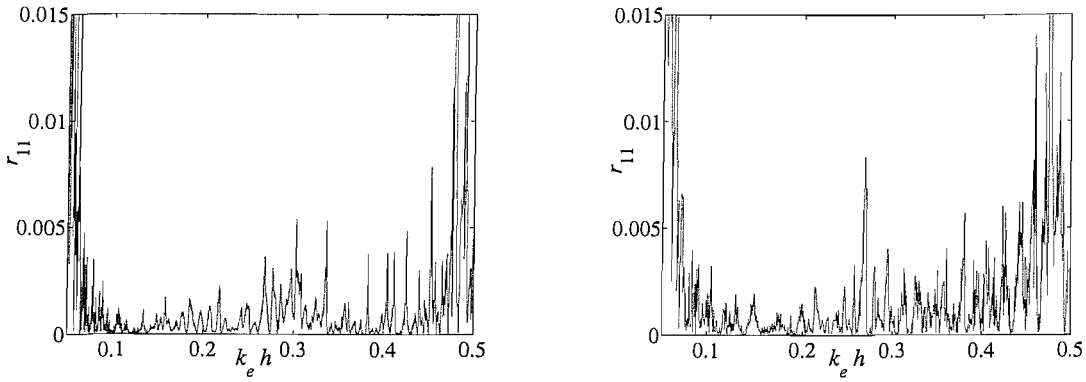

(a) Uniform beam.

(b) $\gamma = 0.13$.

Fig. 6.3: Measured power reflection coefficient r_{11} for a uniform length and slot with $\gamma = 0.13$.

to 6.9. In the figures, the measured values of r_{11} for each specimen are compared to the reflection coefficients estimated from FESE slot models with various depths.

In Figs. 6.4 to 6.9, the measured reflection coefficients are seen to modulate. Assuming that the modulation is a consequence of error, as suggested in the previous chapter, a third-order polynomial least-squares fit is used to estimate the trend of the reflection coefficient. This is done as a visual aid, for comparison with the estimates of the FESE models; it is not intended to represent the reflection coefficient without error.

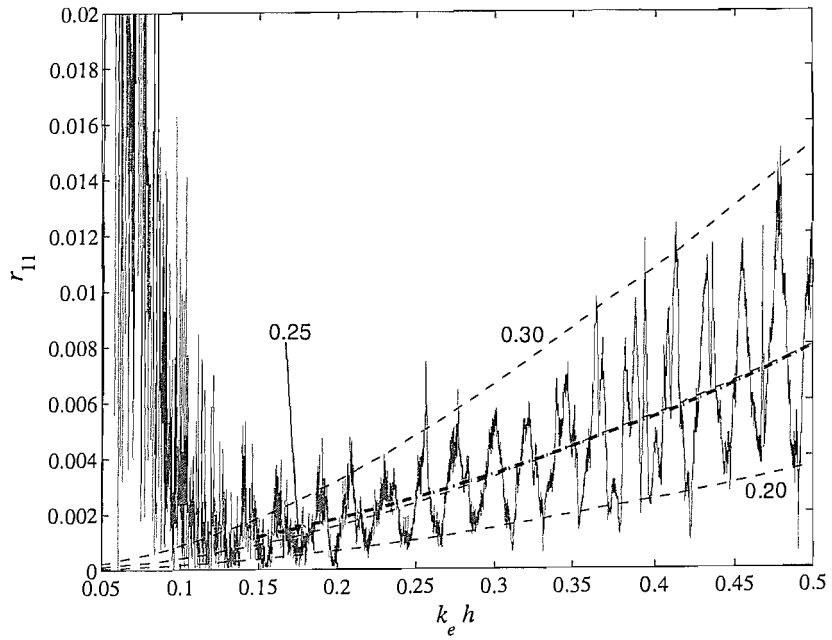

Fig. 6.4: Power reflection coefficient r_{11} for a slot with $\gamma = 0.22$: (—), experimental; (–.–), least-squares fit to experiment; (––), FESE slot models.

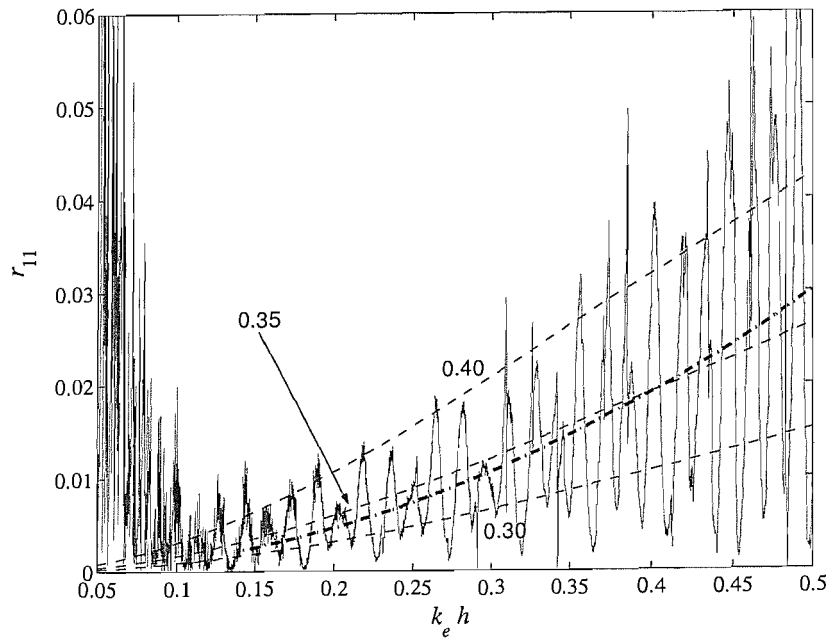

Fig. 6.5: Power reflection coefficient r_{11} for a slot with $\gamma = 0.34$: (—), experimental; (–.–), least-squares fit to experiment; (––), FESE slot models.

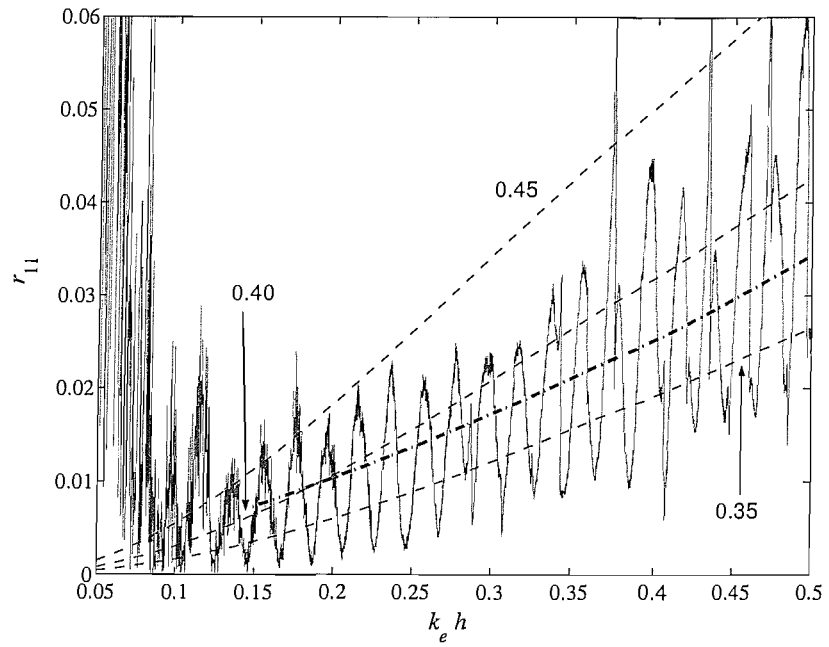

Fig. 6.6: Power reflection coefficient r_{11} for a slot with $\gamma = 0.34$: (—), experimental; (–.–), least-squares fit to experiment; (––), FESE slot models.

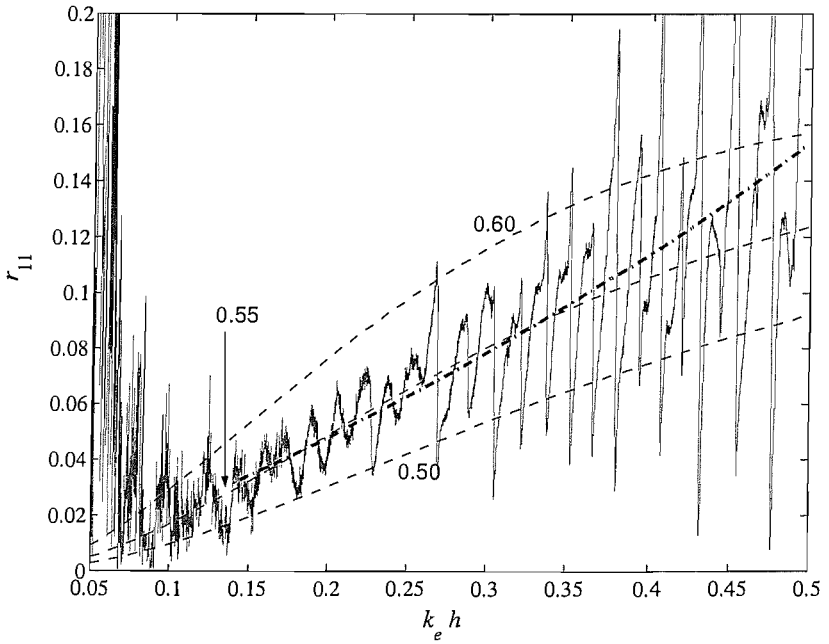

Fig. 6.7: Power reflection coefficient r_{11} for a slot with $\gamma = 0.50$: (—), experimental; (–.–), least-squares fit to experiment; (––), FESE slot models.

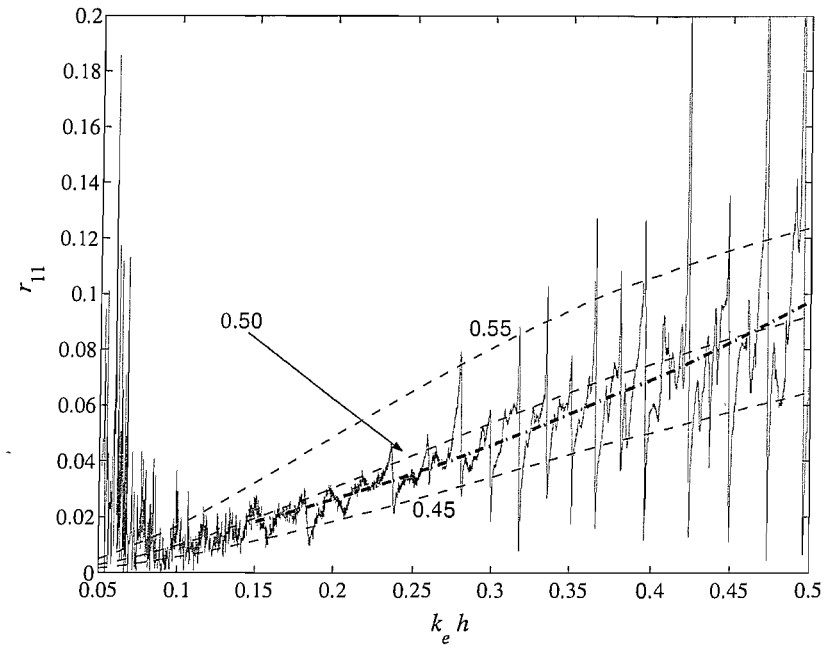

Fig. 6.8: Power reflection coefficient r_{11} for a slot with $\gamma = 0.55$: (—), experimental; (–.–), least-squares fit to experiment; (––), FESE slot models.

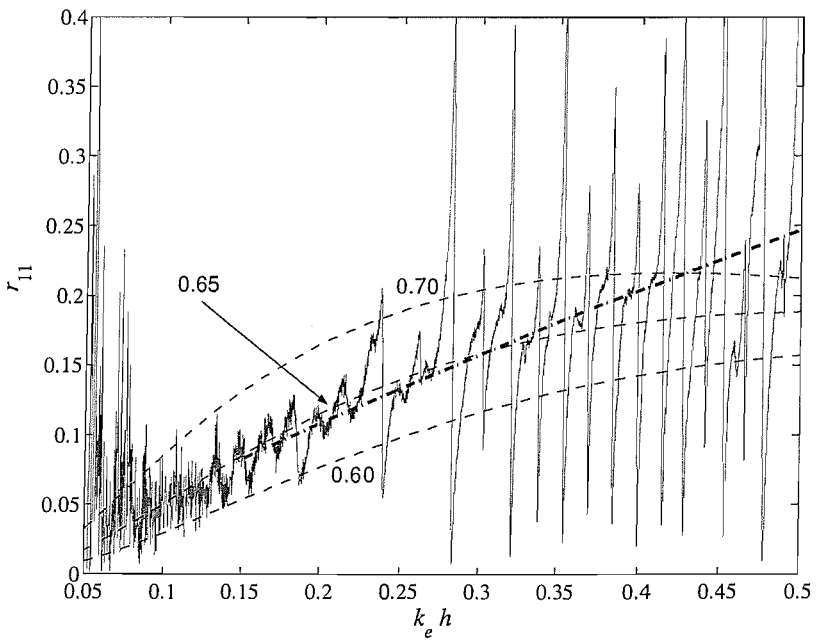

Fig. 6.9: Power reflection coefficient r_{11} for a slot with $\gamma = 0.62$: (—), experimental; (–.–), least-squares fit to experiment; (––), FESE slot models.

6.4. Discussion

Figs. 6.4 to 6.9 show that the measured reflection coefficients are similar to the predictions of the FESE models, though the experimental results show a modulation, which is thought to be caused partly by sensor mis-calibration and errors in the wavenumber estimates. At low frequencies, the experimental results are affected also by noise and ill-conditioning. At high frequencies, there are noticeable differences between the modulation in the measurements for the larger slot depths (Figs. 6.7 to 6.9) in comparison to the other results with smaller depths.

The measured reflection coefficients for larger slots exhibit sharp peaks and troughs, particularly for $k_e h > 0.25$. The peaks occur roughly periodically as a function of frequency and this is shown in Fig. 6.10, where r_{11} is plotted. Given that the period is a function of frequency, this might suggest an influence on the result from axial and/or torsional waves.

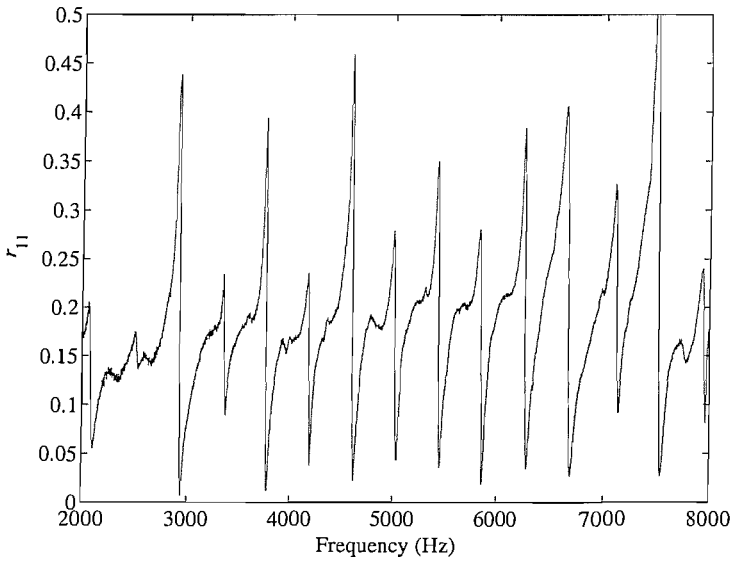

Fig. 6.10: Power reflection coefficient r_{11} as a function of frequency, for $\gamma = 0.62$.

It can be shown numerically that wave-mode conversion causes axial waves to scatter from the slot. It is further possible that wave mode conversion occurs as waves reflect from the sandboxes. If axial waves also propagate along the beam, the reflected flexural wave from the slot is the sum of a reflected incident flexural wave plus reflections of incident axial waves. These axial wave components are not included when the scattering coefficients are calculated, which could result in errors. Moreover, the axial wavelength is much longer than that of the flexural waves and, as a result, such waves are not as well attenuated by the sandboxes.

It is interesting to note that the spacing of the peaks in Fig. 6.10 is approximately 425Hz. The exact boundary conditions of the sand boxes are not known but assuming free-free boundary conditions, the natural frequencies for axial motion are given by the equation

$$f_n = \frac{n\pi}{L_b}\sqrt{\frac{E}{\rho}} \tag{6.1}$$

where L_b = 6m is the total length of the beam and f_n is the nth natural frequency. For the experimental beam, the spacing between each natural frequency, as given by Eq. 6.1, is

$$f_n - f_{n-1} = 406 \tag{6.2}$$

Given the similarities between this value and the spacing of the peaks in Fig. 6.10, it is possible that the peaks are caused by the existence of axial waves. The following subsection presents a numerical example to support this suggestion.

6.4.1. The influence of axial waves on estimates of flexural scattering coefficients

Axial waves are generated when flexural waves scatter at the slot. It is thought that these waves influence the estimates of the flexural wave scattering coefficients when they are reflected by the sandboxes. This effect is simulated in the following example.

Fig. 6.11 illustrates a numerical model comprising an undamped infinite Timoshenko beam including a FESE model of a slot with $\gamma = 0.55$. The scattering coefficients of the sandboxes are not used in this simulation, rather a lumped spring model (see chapter 4) is included on each side of the sensor pairs to simulate the effect of waves reflecting from the sandboxes. The amplitude of the reflected axial waves can be varied by altering the stiffnesses of the springs in the lumped spring model. As in the experiment, the model has two transverse forces and the response at each sensor location is calculated to estimate the scattering coefficients.

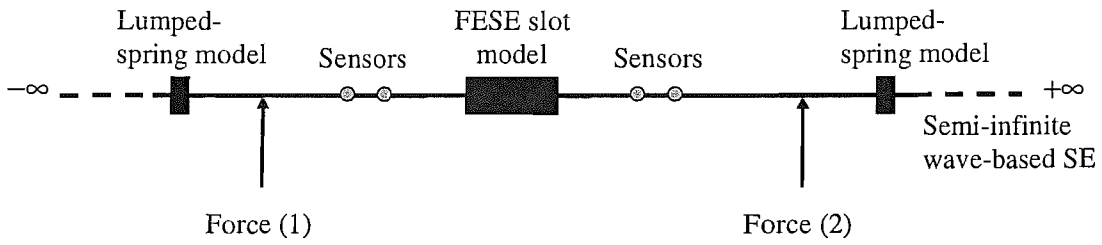

Fig. 6.11: Model used to simulate the experimental estimation of r_{11} for a damaged beam.

The flexural reflection coefficient of the slot was estimated for three examples in which the axial stiffnesses in the lumped-spring models were, in turn, $K_A = 10^{15}$, 10^{10} and 10^8Nm. When $K_A = 10^{15}$Nm, the power axial reflection coefficient of the lumped-spring is less than 10^{-10}; for $K_A = 10^{10}$Nm, it is less that 0.4; and for $K_A = 10^8$Nm, it is close to 1. These three models simulate the cases where there is: a) almost zero axial wave reflection at the sandboxes; b) moderate axial wave reflection at the sandboxes; and c) very large axial wave reflection at the sandboxes. The flexural wave power reflection coefficient is presented in Fig. 6.12 for each of the three models.

These results show that when there is very little axial wave reflection at the lumped springs, the flexural wave reflection coefficient is estimated accurately. As the size of the axial wave reflection from the lumped springs increases, the flexural wave reflection coefficient is less accurate. Most notable are the sharp peaks in r_{11}, which occur when the axial wave reflection coefficients of the springs are large. This result has similarities with the experimental result in Fig. 6.10.

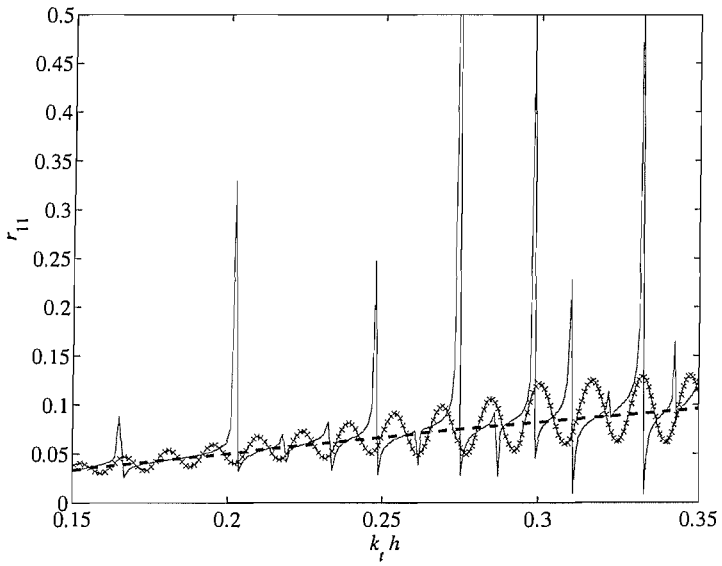

Fig. 6.12: Numerical estimation of r_{11}: (––), $K_A = 10^{15}$N/m; (– × –), $K_A = 10^{10}$N/m; (—), $K_A = 10^{8}$N/m.

There are a number of factors that might contribute to the effect shown in Fig. 6.12. For example, the amplitude of the axial wave generated by wave mode conversion at the slot is frequency dependent. From the FESE notch model, the result presented in chapter 4 (Fig. 4.12) suggested that the amplitude of the axial waves generated at the notch by wave mode conversion is less at low frequencies and larger at high frequencies.

It may be for this reason that large peaks are not seen in Fig. 6.10 at lower frequencies.

Given that the wave mode conversion at the slot and the reflection coefficients of the sandboxes are both frequency dependent, it is difficult to accurately quantify the effects of the axial waves. However, from the numerical results presented here it does appear that the errors seen in the experimental results, such as in Fig. 6.10, can be simulated and are related to axial wave propagation.

6.4.2. Measuring the reflection coefficients on a free-free beam

When the ends of the beam cause large reflections, the measured reflection coefficients are ill-conditioned (chapter 5,§ 5.5). To illustrate this problem the beam was removed from the sandboxes so that the boundary conditions at each end were free-free. The specimen used was that with $\gamma = 0.50$ and the measured power reflection coefficient, r_{11} is presented in Fig. 6.13 (the result for the same specimen, but with ends in sandboxes, is given in Fig. 6.7). The sharp peaks in the result are due to ill-conditioning of the reflection coefficient, resulting from strong resonant behaviour in the beam. Owing to the conditioning issues, it is difficult to estimate the reflection coefficient of the slot from Fig. 6.13.

In a more realistic example, the ends of the beam are likely to be connected at, for example, joints. The size of the reflected waves from the joints are often much smaller than those from the ends of the free-free beam. Therefore, conditioning issues may not cause such severe problems in more practical examples.

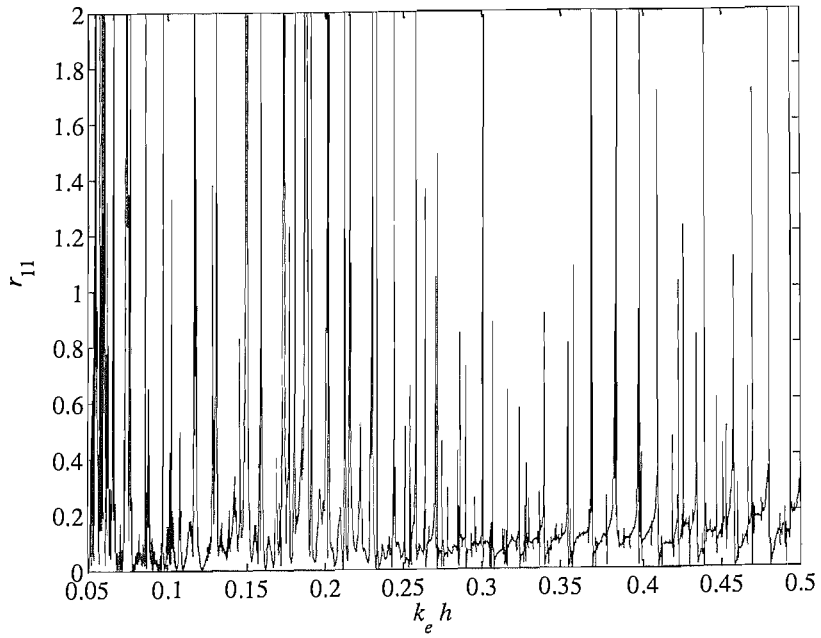

Fig. 6.13: Power reflection coefficient for a slot in a free-free beam with $\gamma \approx 0.50$..

6.5. Summary

Transverse slots have been cut in a number of beam specimens and the reflection coefficients of the slots have been measured. The width of the slot is constant and the depth is approximately uniform over the width of cross-section. The experiments have been used to show how damage can be detected in beams using the reflection coefficients. Various slot depths have been tested and these range from $\gamma = 0.10$ to $\gamma = 0.70$.

As shown in the previous chapter, the measured results suffer from experimental errors. In particular, when the slot is small or at low frequencies, the experimental results are affected by noise. Furthermore, at low frequencies the reflection coefficients are ill-conditioned and are also affected by other errors such as sensor mis-calibration.

At higher frequencies, the results exhibit a noticeable modulation, which can be attributed to experimental errors such as sensor mis-calibration. Importantly, the

reflections from larger slots are more evident at mid and high frequencies.

Comparing the measured results to predictions from FESE models, it was found that the measurements and predictions have similarities. The experimental results suggest three important points:

- it is possible to measure the reflection coefficients of a slot in a beam remote from the damage site;
- it may be possible to estimate the slot depth by comparing the measured reflection coefficients with predictions from FESE models; and
- the modulation in the measured reflection coefficients is related to the distance of the slot from the sensor pairs, hence it may be possible to locate the slot from this feature of the reflection coefficient.

Further to this, if a method could be established to minimise the errors in the experimental results, it may be possible to develop a method that could use the reflection coefficients to suggest the existence of a slot. From the results presented here, it is clear that if one can establish that a non-zero reflection coefficient can be attributed to something other than experimental error, such a result could be used to signify the existence of a discontinuity.

The possibility of estimating the slot depth is explored in the next chapter and chapter 8 considers how the location of the slot can be estimated from the reflection coefficients.

7. Estimating slot depth

7.1. Introduction

The numerical and experimental results presented in chapters 4 and 6 showed that the reflection coefficients of a slot depend on depth and frequency. In this chapter, a method for estimating slot depth from the measured reflection coefficients is considered.

In the experiments, slots of various depths were cut into a number of beams. It was shown that FESE models of the slot predict similar values for the reflection coefficient as the experiment, although the experiment exhibits modulation.

In this chapter, the FESE model is used to create a set of models to develop a reference data set. Each individual model in the set has a single slot depth and is evaluated over a range of frequencies, as described in chapter 4. The analysis is then repeated over many slot depths to create a reference set. The slot depth is estimated by comparing the experimental reflection coefficient to the reference data set.

The more slot depths that are modelled in the reference set, the more accurately the depth can be estimated. The time needed to compute many FESE models is significant, prohibitively so. To avoid this, the results of a small set of FESE models are interpolated to estimate the reflection coefficients at other slot depths and frequencies that are not included in the FESE models.

In the following, it is explained how the reference set is defined and how this can be used to estimate the slot depths of the experimental specimens. This method is supported by numerical and experimental results, which illustrate how accurately the slot depth can be estimated.

7.2. Method

The slot depth is estimated by comparing experimental results to numerical estimates. In this section, the reference data set is defined and it is shown how this can be used with the experimental data to estimate slot depth.

7.2.1. Definition of the reference data set

The experimental power reflection coefficient of a slot is defined as a function of depth and wavenumber, which is given as $r_e(\gamma_e, k_e h)$, where γ_e is the experimental slot depth, which is constant for a given wavenumber, and $k_e h$ is the non-dimensional experimental wavenumber. To estimate the slot depth, γ_e, the value of r_e is compared to a set of reference models.

The set of reference models comprises numerical or analytical models of the damaged beam at various slot depths, over a range of wavenumbers. The power scattering coefficients predicted by the models are used to create a reference data set that is defined as $r_r(\gamma, k_e h)$, where γ is the slot depth. In practice, the set is discrete and is such that an estimate of the power reflection coefficient is known at particular values of γ and $k_e h$.

If it can be assumed that there is a unique value of γ for any two values of r_r and $k_e h$, then $r_r(k_e h) = r_e(k_e h)$ when $\gamma = \gamma_e$.

7.2.2. FESE slot models for the reference set

Here, a number of FESE slot models were used to define the data set r_r. If the shape of the damage was not known, it could be modelled as a notch or a lumped-spring. Both of these models are likely to give results that differ to the slot models and how these differences affect the estimate of the depth is illustrated later in this chapter.

The material properties and dimensions of the experimental specimens were used in

the FESE models. There are differences between the experimental and numerical wavenumbers but they are small for the wavelengths considered.

An FESE model is required for each value of γ in the reference set. Therefore, computational time can become an issue if many values of γ are modelled. For this reason, FESE models were developed only at multiples of $\gamma = 0.05$, i.e., $\gamma = 0, 0.05, 0.10, \ldots, 0.90, 0.95$. This made a total of 19 FESE models and it is assumed that $r_r = 0$ if $\gamma = 0$.

Furthermore, the size of the frequency (or wavenumber) vector is important and, if this includes many frequencies as in the experiment, the computational time can be significant. Therefore, the results of the FESE models were found at fewer frequencies than in the experiment but the frequency ranges of the numerical and experimental results were the same. The FESE models were evaluated at 200 discrete points over the frequency range. Fig. 7.1 illustrates the reference set r_r in the form of a surface plot.

7.2.3. Interpolating the reference data set

In r_r, the variable γ defines to what accuracy the slot depth can be estimated; in this case, to the nearest multiple of $\gamma = 0.05$. This can be improved upon by including more FESE models in r_r at different values of γ. However, if the function r_r is smooth and continuous, the numerical results can be interpolated to estimate the values of r_r at values of γ and $k_e h$ that were not included in the FESE models. Using interpolation is significantly faster, computationally, than producing more models. However, interpolation is an approximation and therefore the result is less accurate than if more models were produced.

A cubic spline is fitted to the results of the FESE model using the `spline` function in Matlab. With the spline, the γ variable is resampled so that it has a resolution of 0.01

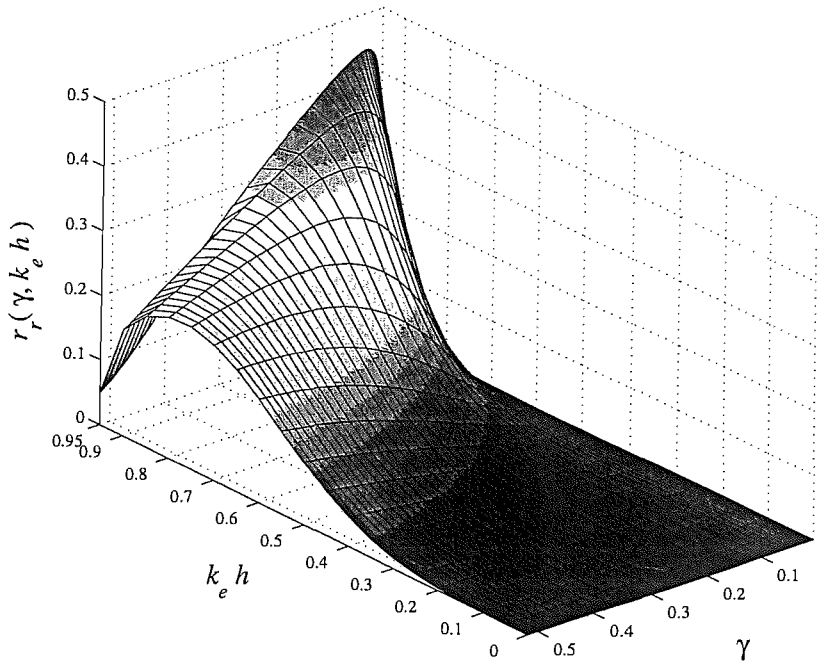

Fig. 7.1: Illutration of the reference data set r_r.

(i.e., the slot depth can be estimated to the nearest multiple of $\gamma = 0.01$). Furthermore, the wavenumber variable is resampled so that it has the same resolution as the experimental results.

7.2.4. Estimating slot depth

At a given wavenumber, r_e is a single experimental value for an unknown slot depth and r_r is a function of γ. An example of this is shown in Fig. 7.2, where r_e is plotted as a constant. This figure shows r_r for a given value of wavenumber, which is like taking a slice through the surface shown in Fig. 7.1. The slot depth is estimated as the value of γ at the point where the two lines intersect, which in this example is approximately 0.40. This is then repeated at all wavenumbers.

In practice, r_e and r_r are discrete functions. The estimate of slot depth is thus found by

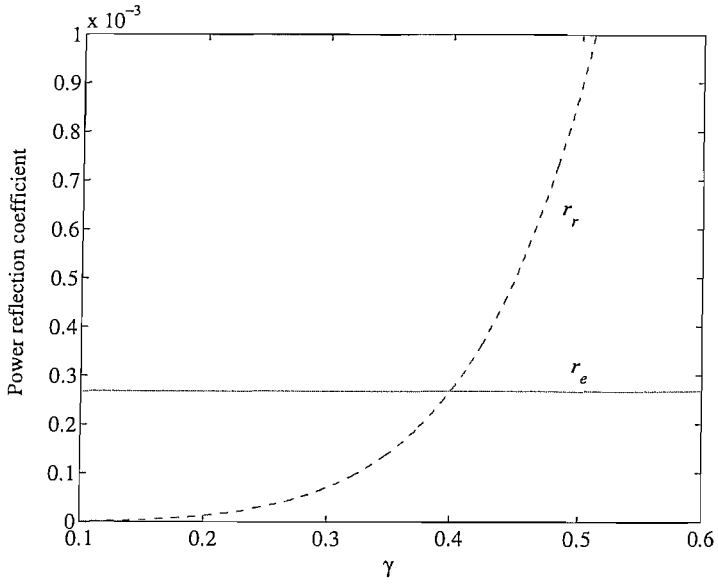

Fig. 7.2: Comparing r_r and r_e for a given value of wavenumber.

minimising the cost function

$$J(\gamma) = | \; r_r(\gamma) - r_e \; | \tag{7.1}$$

i.e., finding the value of γ for which $| \; r_r(\gamma) - r_e \; |$ is minimised. The cost function for the example shown in Fig. 7.2 is shown in Fig. 7.3, where it can be seen that the minimum occurs at $\gamma = 0.4$.

7.2.5. Estimating slot depth at high frequencies

It has been assumed that there is a unique value of γ for given values of r_r and $k_e h$. For large slot depths, the FESE model predicts that the reflection coefficient decreases at high frequencies, as shown in chapter 4 (§ Fig. 4.6). As a result, there is not a unique value of γ for all possible values of r_r and $k_e h$.

Fig. 7.4 shows an example where the cost function has two local minima. In this numerical example $\gamma_e = 0.55$ and is correctly estimated from the smaller of the two minima. In general, however, it can not be assumed that the smaller of the two minima is

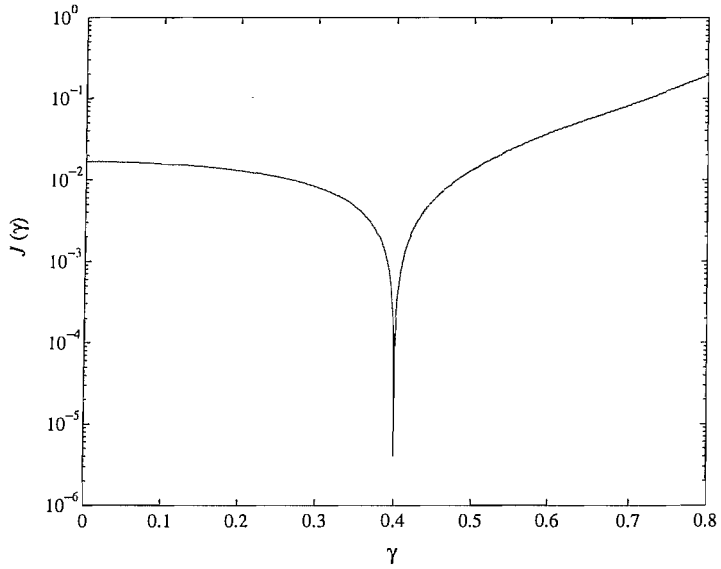

Fig. 7.3: The cost function for a given value of wavenumber.

located at the correct value of slot depth.

The most straightforward way to avoid this problem is to consider low to mid frequencies only, when estimating the depth. However, errors such as noise, particularly at low frequencies, may affect the estimates. Further work might include the development of a more robust method for numerically estimating the slot depth.

7.3. Numerical examples

This section contains two numerical examples that illustrate the estimation of slot depth from the reference data set.

7.3.1. Estimating slot depth

The reflection coefficients are estimated using FESE models for two slotted beams with $\gamma_e = 0.24$ and $\gamma_e = 0.39$, respectively. The reflection coefficients from each model are treated as noise free experimental data and compared to the reference data set to estimate

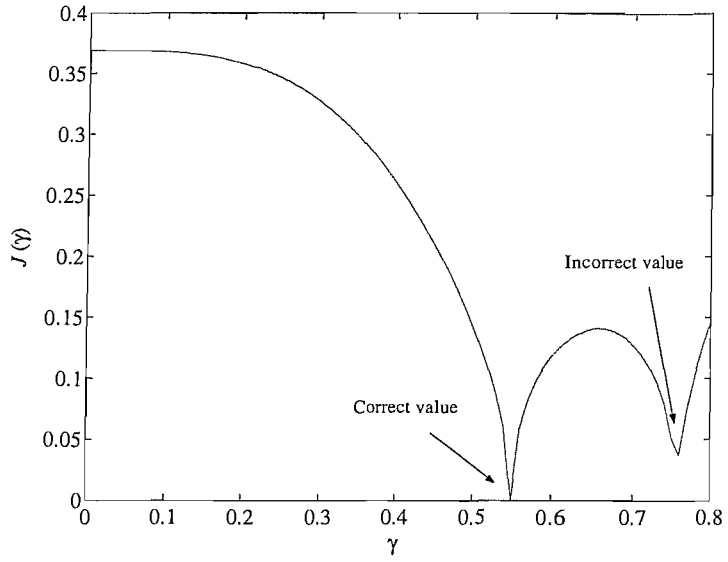

Fig. 7.4: The cost function $J(\gamma)$ when $r_e = 0.1$ and $k_t h = 0.6$.

the slot depth. Furthermore, as neither slot depths were modelled as part of the reference data set, the accuracy of the estimated slot depths depend on the accuracy of the interpolation.

The results in Fig. 7.5 show that slot depths are estimated to good accuracy. For the slot with $\gamma_e = 0.24$, the estimated depth is $\gamma = 0.24$, and for the slot with $\gamma_e = 0.39$ the estimate is 0.38.

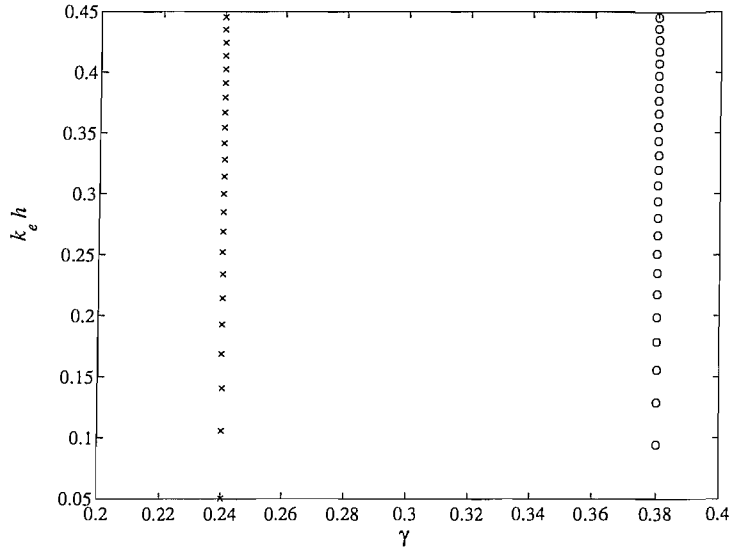

Fig. 7.5: Estimated slot depths: (×), for $\gamma_e = 0.24$; (○), for $\gamma_e = 0.39$.

7.3.2. Example with simulated errors

In chapter 5, a numerical example was used to show how a sensor mis-calibration error or errors in the wavenumber estimate can lead to modulation in the measured scattering coefficients.

Here, the experiment is simulated using a FESE slot model with $\gamma = 0.50$. The model is illustrated in Fig. 7.6, where $L_1 = L_2$ and the output of sensor 1 is multiplied by a factor of 1.05 to simulate a mis-calibration error.

Fig. 7.7(a) shows the reflection coefficient r_{11} as calculated from the model. As shown in chapter 5 (§ 5.5.2), there are significant errors in r_{11} at low frequencies. At higher frequencies, the sensor mis-calibration results in a noticeable modulation in the result.

Fig. 7.7(b) shows the estimates of slot depth. At low wavenumbers, the mis-calibration error causes the slot depth to be, by and large, over estimated. At higher wavenumbers, the modulation seen in the reflection coefficient is also prevalent in the estimate of the slot depth. Furthermore, at high frequencies, there are spurious results

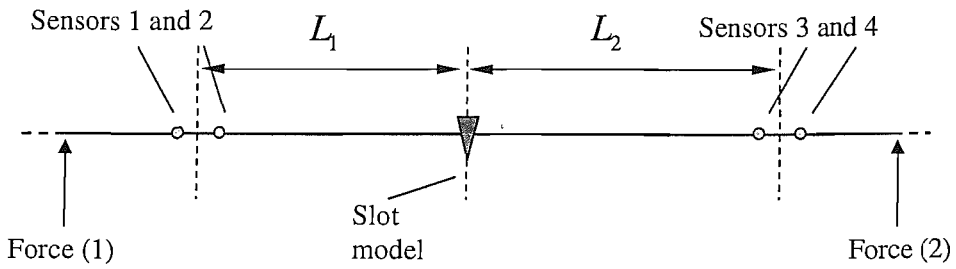

Fig. 7.6: The damaged beam model.

which arise from the fact that there are two local minima in the cost function used to estimate the slot depth and, because the smallest value has been taken, the slot depth is estimated incorrectly at some wavenumbers.

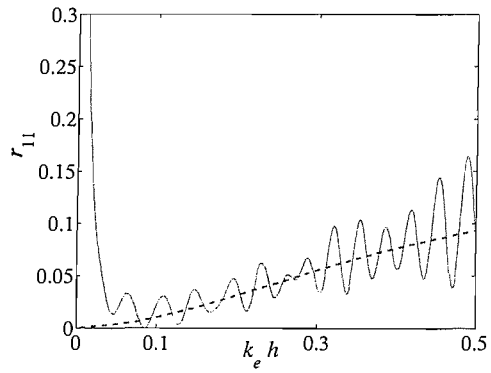

(a) Reflection coefficients: (−−), r_{11} without error; (—), r_{11} with error.

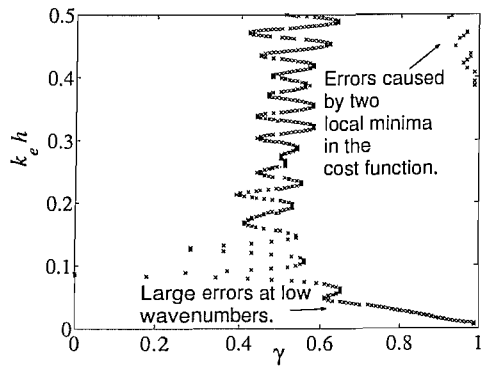

(b) Estimated slot depth with error: (×), $\widehat{\gamma}_e$.

Fig. 7.7: Reflection coefficient and estimated slot depth with a calibration error simulated on the output of sensor 1.

In chapter 6, it was suggested that errors cause the measured reflection coefficient to modulate more-or-less about the true value. Therefore, the slot depth could be estimated

by taking the average of the estimated slot depths, γ_{av}. When taking the average slot depth, care must be taken to discard any obvious signs of error. For example, for the result shown in Fig. 7.7(b), one might discard all values for $k_e h < 0.15$, assuming them to be erroneous. Furthermore, estimates above $k_e h = 0.35$ might also be discarded to remove other possible errors at high wavenumbers. If the slot depth is averaged over this range, one finds that $\gamma_{av} = 0.49$ and the effects of the modulation average out to give a good approximation of the slot depth. However, if the whole wavenumber range is used, and errors are included in the average, the estimate is $\gamma_{av} = 0.59$.

7.4. Experimental results

In chapter 6, Figs. 6.3 to 6.9, the measured power reflection coefficients were given for each damaged beam specimen used in the experiments. Here, the slot depth has been estimated for each specimen using a reference data set comprising FESE models of the slot and the results are presented in this section. In each example, r_{11} and r_{22} were processed to estimate the slot depth. It was found that there were only small differences in the estimated slot depth if r_{22} was processed, so only the results for r_{11} are presented here.

7.4.1. Estimating slot depth

Fig. 7.8 shows the estimated slot depths for the specimen with $\gamma_e = 0.22$. The modulation in this result arises due to the modulation in the measured reflection coefficient. At low frequencies, the reflection coefficient includes error such as noise, ill-conditioning of the scattering coefficients and sensor mis-calibration. As a result of the errors, the measured power reflection coefficient at low wavenumbers can be larger

than any of the values contained in the reference data set. Therefore, the estimated depth is equal to the largest value in the reference set. This can be seen in Fig. 7.8, in which there is a concentration of estimates at $\gamma = 0.95$ for low wavenumbers. Averaging the slot depth over all values of $k_e h$, gives an estimate of $\gamma_{av} = 0.25$.

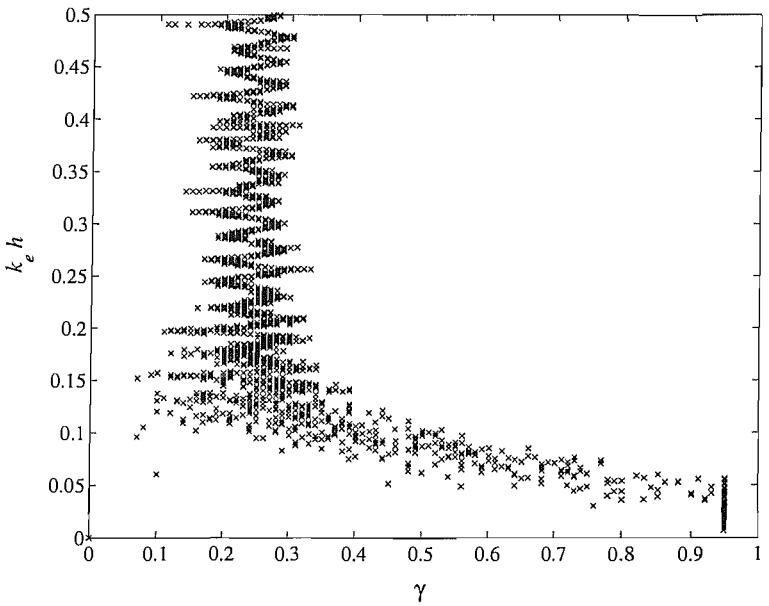

Fig. 7.8: Estimated slot depth for the specimen with $\gamma_e = 0.22$.

A systematic and robust method of removing the erroneous results that are thought to exist in the estimation of slot depth is not considered here. This is due to the fact that the exact causes of the errors can only be speculated, without further investigation into the sources and effects of experimental errors and noise. Such investigation might lead to improvements in the slot depth estimates and could form part of further work. As such, the average slot depth is estimated over the full range of the measurement and this estimate includes any erroneous results. Given that it is expected that errors exist at

lower wavenumbers, for reasons such as sensor mis-calibration error and ill-conditioning, it is expected that this estimate of the slot depth is an overestimate.

The largest slot depth tested was the specimen with $\gamma_e = 0.62$ and the estimated slot depths are plotted in Fig. 7.9. This result shows a concentration of estimates at $\gamma = 0.95$ at low wavenumbers, similar to Fig. 7.8. Again, this is a result of the measured reflection coefficient being larger than the values in the reference data set. However, by inspection of Fig. 7.9, this problem may also occur at higher wavenumbers when the modulation in the reflection coefficient is very large. Taking the average of the depth estimates over all values of wavenumber, it was found that $\gamma_{av} = 0.68$.

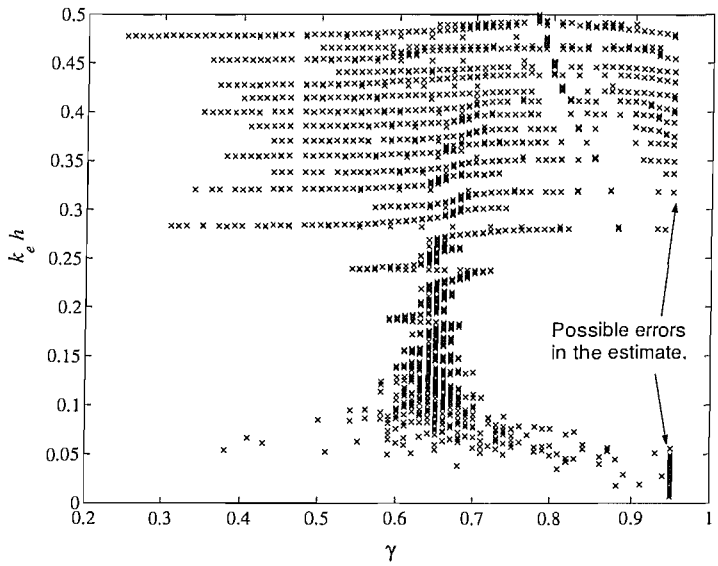

Fig. 7.9: Estimated slot depth for the specimen with $\gamma_e = 0.62$.

The average slot depth was estimated for each experimental specimen and the results are given in Fig. 7.10. In each, the average slot depth is calculated over the whole wavenumber range. Fig. 7.10 shows that the estimated average slot depths give a good

estimate of the actual depth.

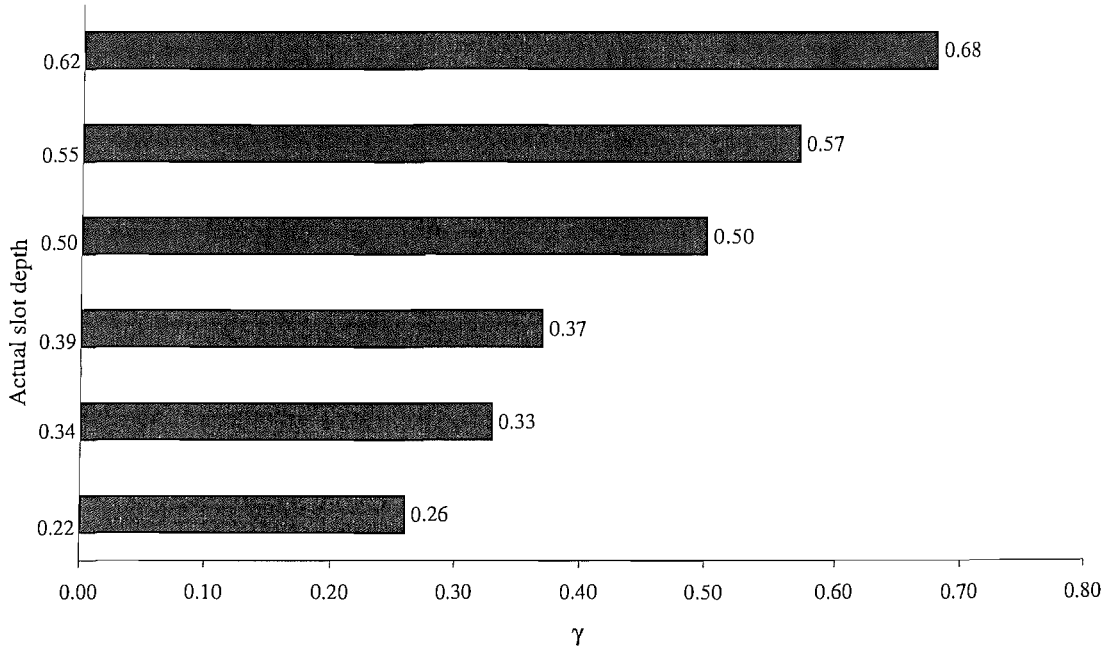

Fig. 7.10: Estimated average slot depths.

7.4.2. Using other damage models to estimate the depth

The results in Fig. 7.10 were calculated using a reference model that was defined using FESE models of a slot. If the shape of the slot is unknown, one might use FESE models of a notch or define the reference set using the lumped-spring notch model, as described in chapter 4.

Two more reference data sets were defined using a FESE notch model and the lumped-spring notch model, respectively. From these reference sets, the average slot depth of each specimen was estimated and the results are presented in Fig. 7.11.

The results show that the slot depth is over-estimated by both models but the results

are still a good approximation. Given that the lumped-spring model is computationally very much more efficient than the FESE models, this result suggests that the lumped spring model can be used, perhaps, as a first approximation to estimate the depth.

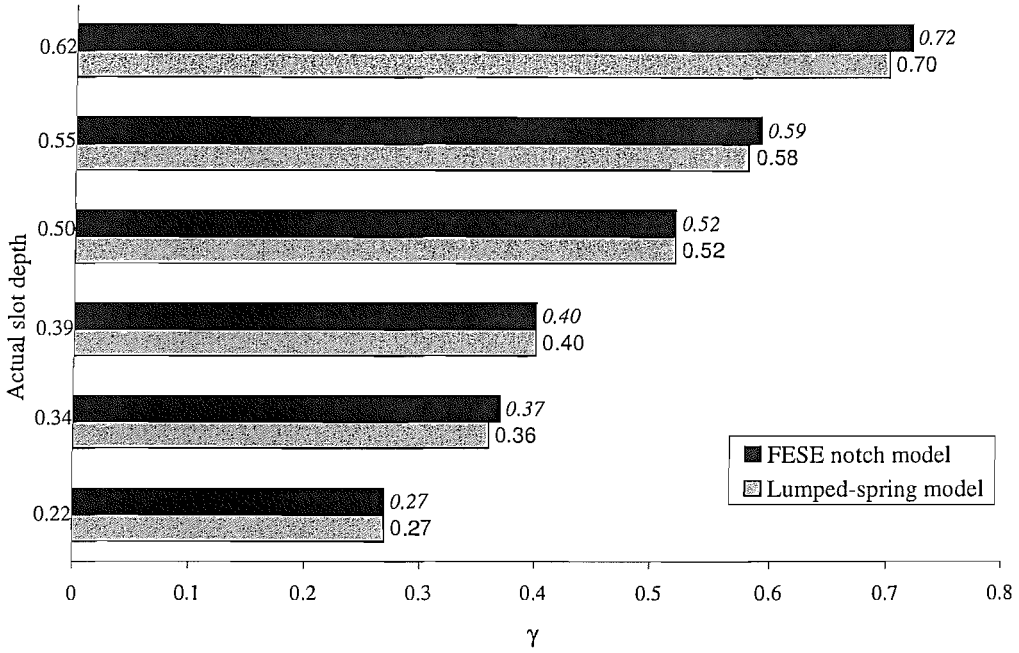

Fig. 7.11: Estimated average slot depths using the FESE notch model and the lumped-spring model.

7.5. Summary

In this chapter, it has been shown that the measured power reflection coefficients of a slot can be used to estimate the slot depth. This was achieved by developing a reference data set from FESE models of the slot, which is then compared to the experimental results.

To reduce the computational time, FESE models were developed for a small number of slot depths and evaluated. A cubic spline was then applied to the reference data set, to

approximate the reflection coefficients at slot depths and frequencies not evaluated in the FESE models.

If the shape of the damage is unknown, the FESE notch model or the lumped-spring model might be used to define the reference data set. Using these models to estimate the depth of the slots in the experiment, it is found that the slot depth is overestimated but the estimates still offer good approximations of the slot depth. The lumped-spring model is much more computationally efficient than the FESE models and, therefore, could be used as a first approximation of the slot depth.

Errors in the measured reflection coefficients make the estimates of the slot depth less accurate. The errors in the measured reflection coefficient are also prevalent in the slot depth estimates. At low wavenumbers, the slot depth is often over-estimated. At higher frequencies, the modulation in the measured reflection coefficient is apparent in the depth estimates. Furthermore, experimental errors can create values of the measured reflection coefficient that are larger than any of the values in the reference data set, thereby introducing errors in the depth estimates.

The slot depth can be estimated by averaging the depth estimates over each value of wavenumber. This estimate proved accurate but might be improved if the sources and effects of experimental error are identified and minimised and erroneous results discarded.

8. Locating slots from the reflection coefficients

8.1. Introduction

An important part of damage detection is the ability to locate the damage. Although, it may be possible to detect the presence of a discontinuity in the structure, positively identifying the discontinuity is a separate issue. One could argue that locating a discontinuity brings us one step closer to identifying it.

In this chapter, a method is described that uses the measured reflection coefficients in chapter 6 to locate the slots in each of the experimental specimens. The scattering coefficients modulate as a function of wavenumber and the frequency of this modulation can be related to the distances from each sensor pair to the slot. The inverse Fourier transform is used to transform the scattering coefficient from the wavenumber to spatial domains and, from this, estimate L_1 and L_2. These distances are shown in Fig. 8.1. Issues that arise in this process, such as sampling and resolution, are addressed herein.

Numerical and experimental results are used to illustrate the accuracy of the estimated locations. Also included is an example to illustrate how the method can be used to locate more than one slot.

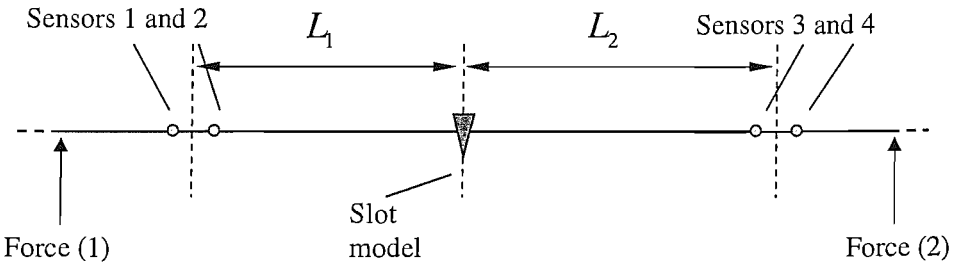

Fig. 8.1: Schematic of the damaged beam.

8.2. Method

In chapter 5, Eq. 5.15, the measured scattering coefficients were given and these can be written as

$$\widehat{R}_{11} = |R_{11}|\, e^{-2ik_e L_1 + i\theta_{11}} \quad ; \quad \widehat{R}_{22} = |R_{22}|\, e^{-2ik_e L_2 + i\theta_{22}} \tag{8.1}$$

where $\theta_{11,22}$ is the phase of the reflection coefficients at the discontinuity. In these estimates, both damping and the contribution of any nearfield waves has been neglected.

The reflection coefficients are complex oscillating functions and have, in general, three terms that vary with frequency: $|R_{11,22}|$, $e^{-2ik_e L_{1,2}}$ and $e^{i\theta_{11,22}}$. The term $|R_{11,22}|$ describes the magnitude of the reflection coefficient, while the phase has two distinct components, one that relates to $\theta_{11,22}$ and one that relates to $L_{1,2}$. Often $e^{i\theta_{11,22}}$ is slowly varying with frequency and analytical and numerical models predict this in the case of a slot. How rapidly the term $e^{-2ik_e L_{1,2}}$ varies with frequency, depends on k_e and $L_{1,2}$. The term $e^{-2ik_e L_{1,2}}$ often varies far more rapidly with frequency than $e^{i\theta_{11,22}}$ unless $L_{1,2}$ is very small.

8.2.1. Inverse Fourier transform in the wavenumber domain

The oscillating components of the reflection coefficient are directly related to the lengths L_1 and L_2. By finding the frequency of the oscillations, $L_{1,2}$ can be estimated. The term

'frequency' is normally used in structural vibration to describe the oscillations per unit time. To avoid confusion, here the term "k-frequency" is used to describe the number of oscillations per unit wavenumber. In the same way that a spectrum of a time history is said to describe the harmonic content of the signal, the k-frequency content, or k-harmonics, are described by the k-spectrum. Relating these terms to the reflection coefficients: the reflection coefficients oscillate at k-frequencies that relate to the phase terms and by finding the k-harmonic content of the reflection coefficient, the lengths L_1 and L_2 can be estimated.

To determine the k-harmonic content of the reflection coefficient, the inverse Fourier transform (IFT) is used. The IFT transforms the reflection coefficients from the wavenumber domain to the spatial (or wavelength) domain. Again, often the IFT is used in structural analysis to transform the frequency domain to the time domain, so the term kIFT is used here to make it clear that the transform is from wavenumber to space. The kIFT can be written

$$s(\Lambda) = \int_{-\infty}^{\infty} S(k) e^{2\pi i k \Lambda} \, dk \tag{8.2}$$

where k is the wavenumber and the variable Λ has units of length. The variable Λ is directly related to the physical distance by $x = \pi\Lambda$. It is important to note that S must be a function of k and k must be known.

One might make the observation that $s(\Lambda)$ is a form of spatial impulse response and should be real, but it is unclear what the kIFT of a scattering coefficient physically represents. Here, $s(\Lambda)$ is treated as a spectrum, which is referred to as the 'k-spectrum', and this describes the k-harmonic composition of the function $S(k)$, in the spatial domain.

8.2.1.1. *Example of the kIFT*

To illustrate the application of the *k*IFT, suppose that $S = \widehat{R}_{11}$, as given in Eq. 8.1, but assume that $|R_{11}|$ and θ_{11} are constant for all k_e. Transforming S with the *k*IFT, it is found that

$$s(\Lambda) = \int_{-\infty}^{\infty} \left|\widehat{R}_{11}\right| e^{i\theta_{11}} e^{2\pi i k_e (x - L_1/\pi)}\, dk_e$$

$$= \left|\widehat{R}_{11}\right| e^{i\theta_{11}} [\delta (x - L_1/\pi)] \tag{8.3}$$

where δ denotes the delta-function. The k-spectrum has one k-harmonic that is represented by a delta-function at $\Lambda = L_1/\pi$ and, therefore, $x = L_1$. This simple example shows how L_1 can be estimated from the reflection coefficient.

8.3. Practical considerations

8.3.1. Resampling the reflection coefficients

In the experiments, $\widehat{R}_{11}$ and $\widehat{R}_{22}$ are sampled variables. Therefore, $s(\Lambda)$ is calculated using the inverse fast Fourier transform (*k*IFFT). To apply the *k*IFFT, $\widehat{R}_{11}$ and $\widehat{R}_{22}$ must be functions of wavenumber.

From the measurement, the reflection coefficients are always sampled in the frequency domain. Let the measured reflection coefficient be $\widehat{R}(f_s)$, where $f_s = n\Delta f$ is the frequency sample vector, n is the sample number and Δf is the sample spacing, which is constant for all frequencies.

The reflection coefficient in the wavenumber domain is described by $\widehat{R}(k_s)$, where $k_s = n\Delta k$ is the wavenumber sample vector and Δk is the sample spacing in the wavenumber domain.

To apply the *k*IFFT to $\widehat{R}(k_s)$, the sample period of k_s must be constant for all

wavenumbers. The variables f_s and k_s are related by the dispersion relation. If the wavenumber is proportional to frequency (e.g., axial waves) then $\Delta k \propto \Delta f$, such that Δk is constant. However, for flexural waves, it is assumed that $k_s \propto \sqrt{f_s}$ and, as such, the sample spacing is not constant in the wavenumber domain.

To get around this problem, the reflection coefficient is resampled using a new wavenumber sample vector k'_s, which has a constant sample period $\Delta k'$. The vector k'_s has the same number of samples as k_s and covers the same range. The sample period of k'_s is given by

$$\Delta k' = \frac{N}{k_{max} - k_{min}} \tag{8.4}$$

where k_{max} and k_{min} are the maximum and minimum values of the original sample vector k_s and N is the number of samples.

The reflection coefficient is resampled using the `spline` function in Matlab. The function was used to interpolate between the sample points, to estimate the values of the reflection coefficient at the new sample points in k'_s.

An example to illustrate the resampling procedure is shown in Fig. 8.2. This figure shows a function $\widehat{R} = \sin(kL)$, with $L = 1$ and $k = 0.8\sqrt{f}$. The function is plotted against the three sample vectors, f_s, k_s and k'_s. A point of interest is the small number of sample points for small values of k_s. It is in this region that the interpolation may be less accurate.

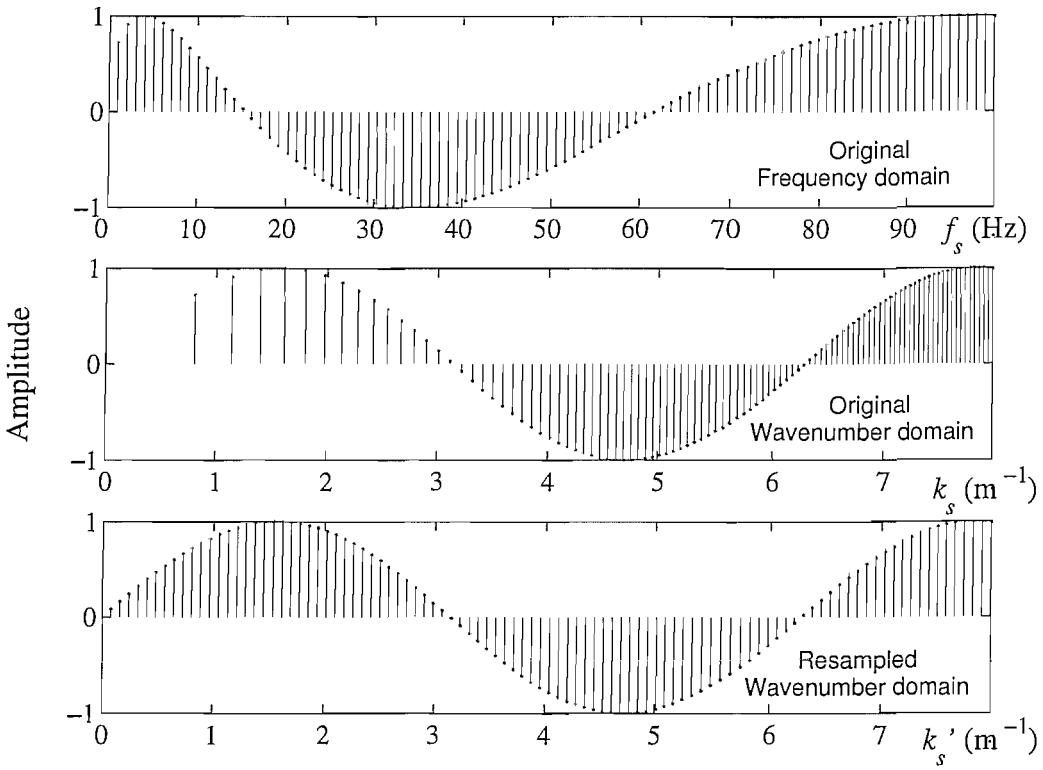

Fig. 8.2: Illustration of the resampling of the reflection coefficient.

8.3.2. Resolution

In the *k*-spectrum, the spatial variable Λ is discrete and is given by

$$\Lambda = \frac{N}{M}\left(\frac{[0,1,2,\ldots,M-1]}{k_{max}-k_{min}}\right) \tag{8.5}$$

where M is the number of points in the *k*IFFT. The resolution of Λ and hence x determines how accurately the lengths L_1 and L_2 can be estimated.

The resolution can only be improved by increasing the number of points in the *k*IFFT or by increasing the wavenumber range. How much the wavenumber range can be increased is constrained by factors such as the frequency range of the experimental equipment. Moreover, when the wavelength is shorter than the dimensions of the cross-section, higher order wave modes cut on and the estimates of $\widehat{R}_{11}$ and $\widehat{R}_{22}$, as given

here, are invalid.

Given the importance of the resolution, every effort should be made to improve it, where possible. Making improvements to the experiment equipment may be costly and time consuming. For flexural motion, the frequency range would need to be quadrupled in order to halve the resolution. For axial or torsional motion, the frequency range would need to be doubled to halve the resolution. Over a given frequency range, the axial and torsional wavenumbers are often much smaller than the flexural wavenumber for thin beams. Therefore, often the resolution is best when flexural waves are measured.

8.3.3. Windowing

The measured scattering coefficient has a finite bandwidth in the wavenumber domain and, as such, the effect of the finite window smears the k-spectrum, $s(\Lambda)$. Theoretically [63], for $s(\Lambda)$ to show a k-harmonic, $\widehat{R}_{11,22}$ must include at least one oscillation within the wavenumber range, therefore

$$L_{1,2} > \frac{\pi}{k_{max} - k_{min}} \tag{8.6}$$

This result states that a discontinuity must be located at a minimum distance from either of the sensor pairs in order for it to be located using the k-spectrum.

8.3.4. Aliasing

The sampling rate of the original sample vector f_s is $1/\Delta f$. Although there is no fixed sampling rate for the sample vector k_s, for the new wavenumber sampling vector, k'_s, the sampling rate, k_{smp}, is

$$k_{smp} = \frac{1}{\Delta k'} \tag{8.7}$$

This sampling rate has units of length. Therefore, we can also define a theoretical folding k-frequency, k_{ff}, at approximately

$$k_{ff} = \frac{1}{2\Delta k'} \tag{8.8}$$

This limit defines the maximum k-frequency that can be analysed without causing aliasing. The folding k-frequency determines the maximum values of $L_{1,2}$ that can be estimated using the kIFFT. The maximum value of $L_{1,2}$, L_{max}, is theoretically

$$L_{max} = \pi k_{ff} \tag{8.9}$$

The folding k-frequency depends on the wavenumber and the number of sample points in k'_s. Often, k_{ff} is large compared to $L_{1,2}$, e.g., in the experiments that were discussed in chapter 6, $L_{max} > 100$m, such that effects of aliasing are not a concern.

8.3.5. Measurement error and noise

Experimental error affects the accuracy of the estimates of $L_{1,2}$ (e.g., errors in the estimation of the wavenumber). Assuming that the reflection coefficients are known, errors in wavenumber affect the derivation of the wavenumber sample vectors k_s and k'_s. As a result, the spatial variable x of the k-spectrum includes error.

Noise on the reflection coefficient can also affect the estimation of $L_{1,2}$. This is a well known problem of a sinusoidal signal embedded in noise. When the signal to noise ratio is small, the k-harmonic may be masked by noise and it is more difficult to estimate $L_{1,2}$.

8.4. Numerical examples

In this section, the results of a number of numerical examples are presented to illustrate the estimation of slot location using the kIFFT. In all the numerical and experimental results, the k-spectrum is plotted as a function of x (or $\pi\Lambda$).

8.4.1. Resampling the reflection coefficient

The reflection coefficient is resampled by interpolating between the sample points in the original frequency vector along a new wavenumber sample vector. This process is approximate and may affect the accuracy of the estimates of $L_{1,2}$.

To illustrate the accuracy of the resampling method, suppose that $S(k) = \widehat{R}_{11} = e^{-2ikL_1}$, where $L_1 = 1\text{m}$, $k = 0.87\sqrt{f}$ and the frequency range is from 0 to 9600Hz with 16384 sample points. The number of points used to calculate the kIFFT is also 16384. These values are similar to the experimental work.

The function S can be defined in two ways. First, it is defined by a frequency sample vector k_s that has a constant sampling period in the frequency domain. As explained, this function must be resampled along a new sample vector k_s' in order to apply the kIFFT. A second function $S(\tilde{k}_s)$ is also defined, in which $\tilde{k}_s$ has a sample period that is constant in the wavenumber domain. As such, $S(\tilde{k}_s)$ does not require resampling before it is transformed using the kIFFT. The purpose of comparing the two is to illustrate the accuracy of the resampling procedure. If the resampling is accurate, the k-spectrum of $S(k_s')$ should be equivalent to that of $S(\tilde{k}_s)$.

Fig. 8.3 shows part of $S(k)$ and the power k-spectra, $|s(\Lambda)|^2$, for each case. Each row of subfigures in Fig. 8.3 is labelled, (a), (b) and (c), respectively. The figures in row (a) show $S(k_s)$ and its k-spectrum. It is clear that the k-spectrum has little meaning when the sample period is not constant as a function of wavenumber. The figures in row (b) show $S(k_s')$ and its k-spectrum, which is the resampled version of $S(k_s)$. The value chosen for L_1 was 1m and it can be seen that the peak in the k-spectrum of $S(k_s')$ occurs near to $x = 1\text{m}$. Finally, row (c) shows $S(\tilde{k}_s)$, which did not require resampling. Its k-spectrum is almost identical to that found for $S(\tilde{k}_s)$ with only minor differences found in the

magnitude of the peak.

Fig. 8.4 shows the region of the k-spectra for $S(\tilde{k}_s)$ and $S(k_s')$ around the peak. The peak value occurs at $x \approx 0.995$m, and the resolution of x is 0.037m in this example.

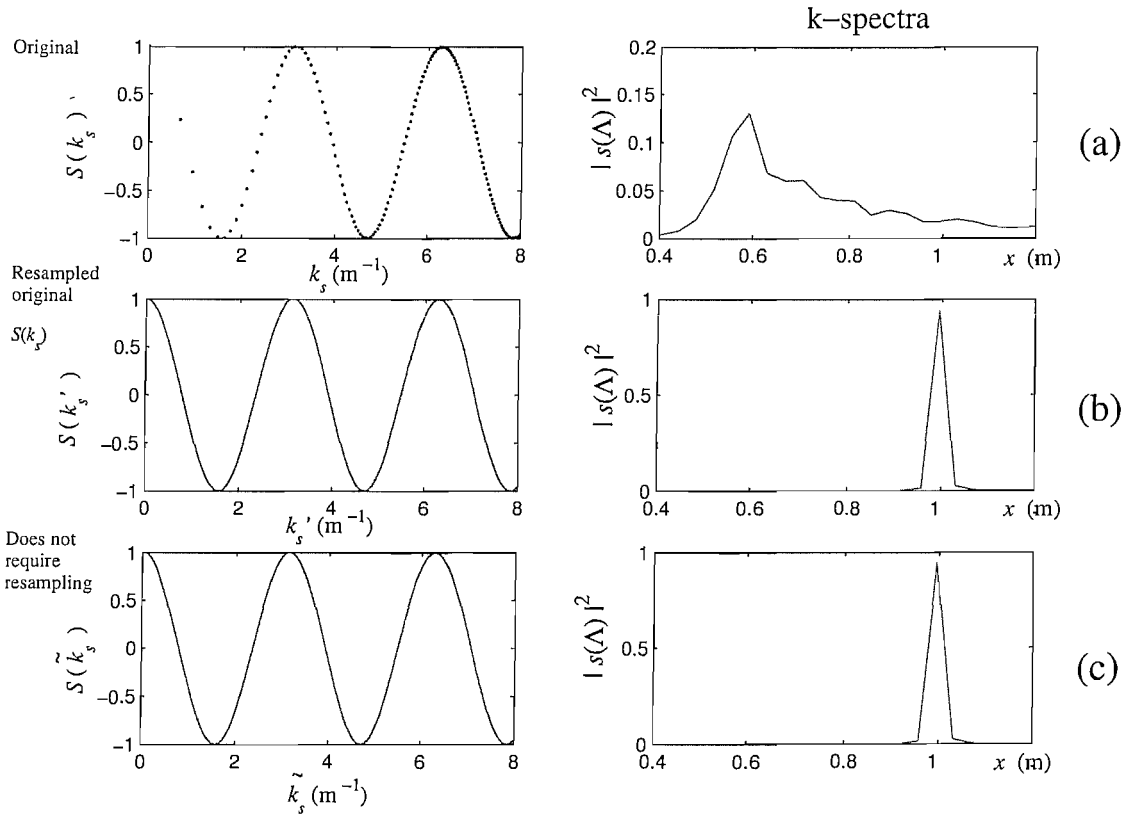

Fig. 8.3: Illustration of the k-spectra for variables when the sample period is constant or is not constant as a function of wavenumber, where L_1 = 1m.

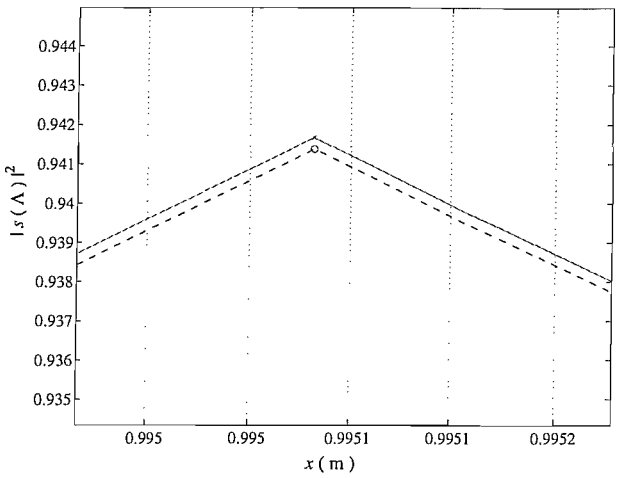

Fig. 8.4: Estimation of location using the *k*IFFT, $L_1 = 1$m: $(- \circ -)$, function was resampled; $(- \times -)$, function was not resampled.

8.4.2. Locating damage in an infinite beam

In this subsection, the *k*IFFT is used to locate a notch with $\gamma = 0.50$ in an infinite beam. A numerical model is used to simulate the experiment, which is illustrated in Fig. 8.5. The sensor spacing is 2cm and the beam is excited by point forces. The frequency range is from 0.1 to 9600Hz with 16384 sample points. The model was created using the lumped-spring notch model.

The *k*IFFT is used to transform both reflection coefficients, $\widehat{R}_{11}$ and $\widehat{R}_{22}$ found from the model after they have been resampled, i.e., the reflection coefficients "measured" by sensor pairs 1 and 2. The *k*-spectra are shown in Fig. 8.6 and the estimated distances from the sensor pairs to the notch, rounded to the nearest millimetre, are shown in the figure and given in Table 8.1, where $\widehat{\cdot}$ denotes the estimates. The estimates are taken from the location of the tips of the *k*-harmonics. The resolution of x is approximately 3.7cm, as calculated from Eq. 8.5. These results indicate that the location of the lumped-spring can be estimated with good accuracy from the *k*-spectrum.

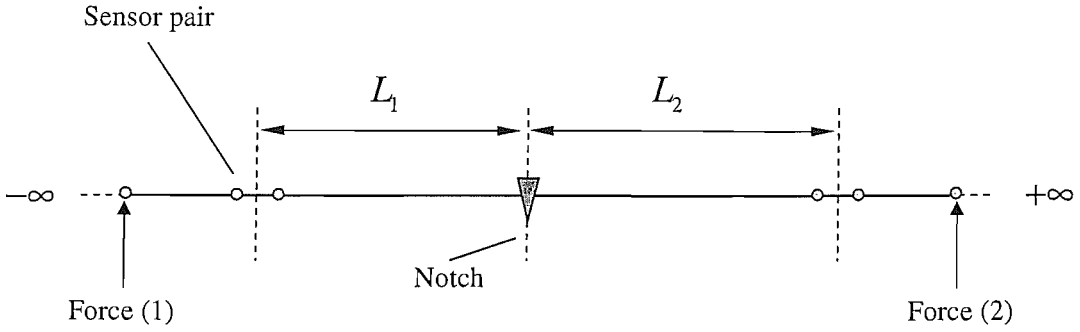

Fig. 8.5: Infinite beam model with a notch.

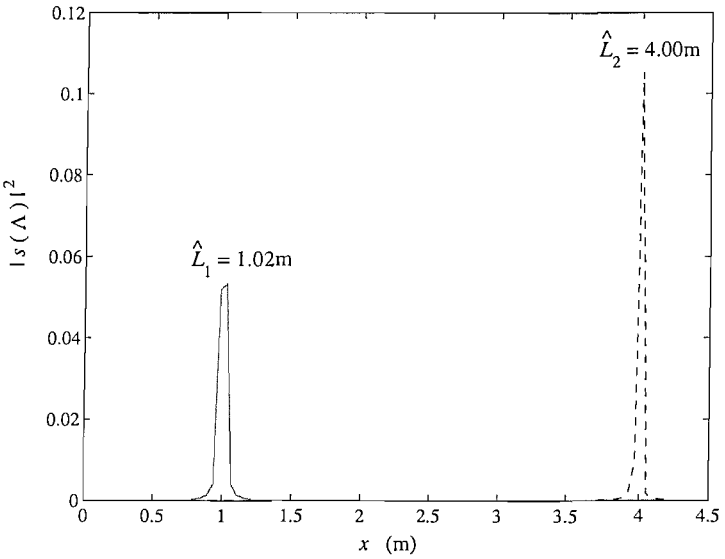

Fig. 8.6: Locating a notch in an infinite beam with $\gamma = 0.50$: (—), k-spectrum for $\widehat{L}_1$ from $\widehat{R}_{11}$; (– –), k-spectrum for $\widehat{L}_2$ from $\widehat{R}_{22}$.

	$\widehat{R}_{11}$		$\widehat{R}_{22}$	
γ	L_1 (m)	$\widehat{L}_1$ (m)	L_2 (m)	$\widehat{L}_2$ (m)
0.50	1.00	1.024	4.00	4.009

Table 8.1: Estimated notch locations for a numerical model of a cracked infinite beam.

8.5. Experimental results

8.5.1. Slotted beam specimens

The *k*IFFT is now applied to the reflection coefficients that were measured on each of the beam specimens that were considered in chapter 6. The *k*-spectrum for the specimen with $\gamma = 0.50$ is shown in Fig. 8.7 (the measured reflection coefficient can be found in Fig. 6.7, chapter 6, § 6.3.).

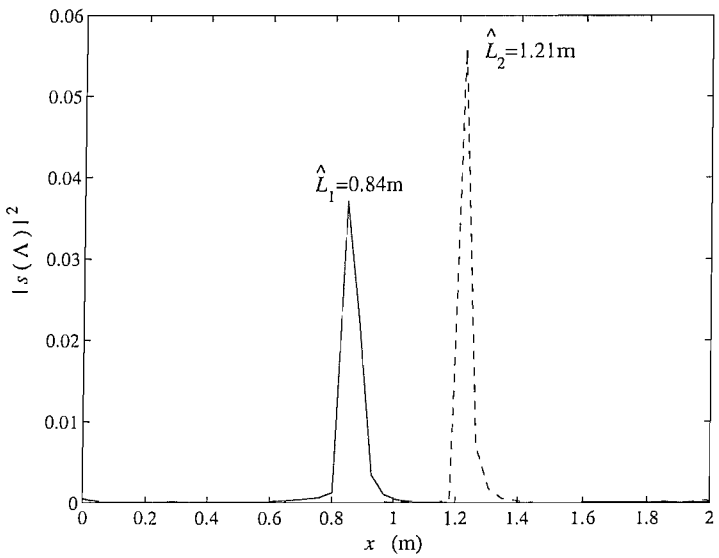

Fig. 8.7: Estimation of the location of a slot with $\gamma = 0.50$: (—), *k*-spectrum for $\widehat{L}_1$ from $\widehat{R}_{11}$; (−−), *k*-spectrum for $\widehat{L}_2$ from $\widehat{R}_{22}$.

The distances from the slot to the sensor pairs were measured to the nearest centimetre and are L_1 = 0.83m and L_2 = 1.18m; these are referred to as the 'actual' values. The location of the slot can be estimated from the k-harmonics shown in Fig. 8.7 and the values, found to the nearest centimetre, are $\widehat{L_1}$ = 0.84m and $\widehat{L_2}$ = 1.21m, which are in good agreement with the actual values.

	$\widehat{R}_{11}$			$\widehat{R}_{22}$		
γ	L_1 (m)	$\widehat{L_1}$ (m)	Error (m)	L_2 (m)	$\widehat{L_2}$ (m)	Error (m)
0.13	0.84	0.83	0.01	1.19	1.16	0.03
0.22	0.84	0.86	0.02	1.17	1.19	0.02
0.34	0.81	0.83	0.02	1.21	1.25	0.04
0.39	0.86	0.84	0.02	0.98	0.96	0.02
0.50	0.83	0.84	0.01	1.18	1.21	0.03
0.55	0.83	0.85	0.02	1.18	1.17	0.01
0.62	0.83	0.80	0.03	1.19	1.16	0.03

Table 8.2: Actual and estimated slot locations for the experimental beams.

The *k*IFFT was applied to the reflection coefficients of each beam specimen and the estimated locations are given in Table 8.2. This table also shows the 'actual' locations of the slots, measured to the nearest centimetre. The results show a good agreement between the actual and estimated values, where the resolution of x is 3.7cm.

Interestingly, Fig. 6.3(b) (chapter 6, § 6.3) showed that it was not possible to

accurately estimate the reflection coefficient of the slot when $\gamma = 0.13$ because the magnitude of the reflection coefficients were similar to the magnitudes due to errors and noise. However, applying the *k*IFFT to the reflection coefficient, Fig. 8.8, shows that it is possible to estimate the location of the slot. The reflection coefficients are small for this slot and, as such, the magnitudes of the *k*-harmonics are small. Also, the noise is more obvious in the *k*-spectrum, given in Fig. 8.8. Noise is more likely to be an issue when locating small slots using the *k*IFFT.

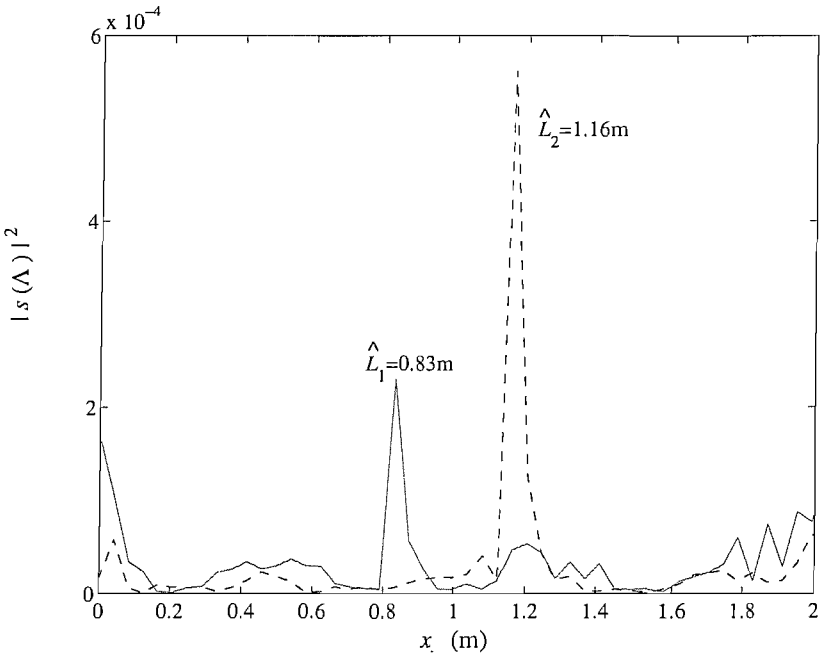

Fig. 8.8: Estimation of the location of a slot with $\gamma = 0.13$: (—), *k*-spectrum for $\widehat{L_1}$ from $\widehat{R}_{11}$; (– –), *k*-spectrum for $\widehat{L_2}$ from $\widehat{R}_{22}$.

8.5.2. Free-free beam

An example that illustrated the difficulties of measuring the scattering coefficients on a free-free beam was given in chapter 6 (§ 6.4.2, Fig. 6.13). Large reflections from the

ends of the beam cause the estimates of the scattering coefficients to be ill-conditioned and this also occurs when any large scatterers exist outside the span of the sensor pairs. The reflection coefficient R_{11} is (from Eq. 5.15)

$$R_{11} = \left(\frac{a_-^{(1)} b_-^{(2)} - a_-^{(2)} b_-^{(1)}}{a_+^{(1)} b_-^{(2)} - a_+^{(2)} b_-^{(1)}} \right) e^{2ik_e L_1} \tag{8.10}$$

and when $a_+^{(1)} b_-^{(2)} \approx a_+^{(2)} b_-^{(1)}$ the reflection coefficient is very sensitive to measurement errors. The oscillations in the complex reflection coefficient are described in the phase term e^{2ikL_1} and there is also a phase term associated with the complex wave amplitudes. Although analytically it would seem that the term e^{2ikL_1} is unaffected if the calculation is ill-conditioned, numerically this is only the case up to machine accuracy. However, the reflection coefficient is only likely to be so large at a few frequencies. Therefore, the oscillation caused by the term e^{2ikL_1} may still be apparent in the measured reflection coefficient.

Fig. 8.9 shows the k-spectrum for the free-free beam with $\gamma = 0.55$. The estimated and actual slot locations are given in Table 8.3. This result shows that there is more noise in the k-spectrum for the free-free case than when the beam is in sandboxes and this is thought to be a result of the conditioning errors in the calculation of the scattering coefficients. Although this does not appear to affect the estimated locations in this example, it may pose a problem for estimating smaller damage when there are large scatterers outside the span of the sensors.

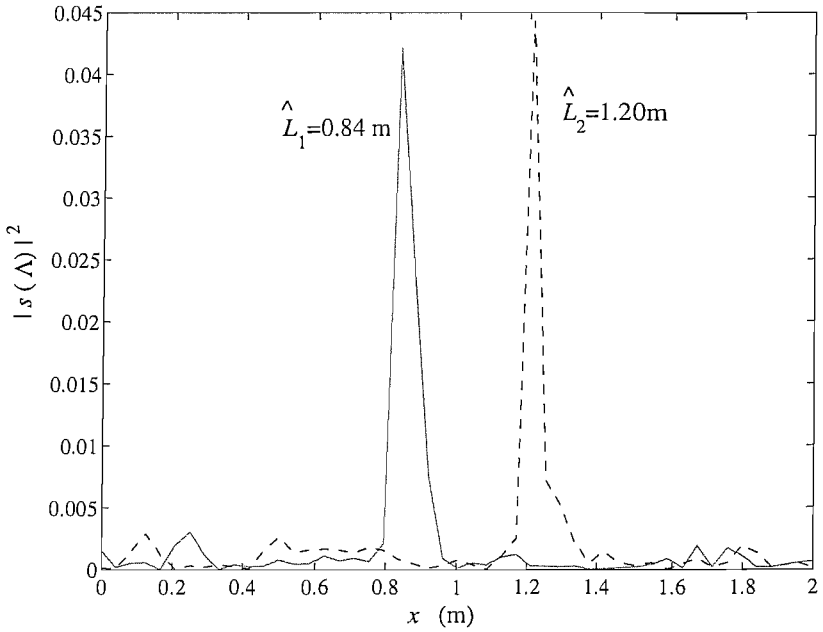

Fig. 8.9: Estimation of the location of a slot with $\gamma = 0.55$, in a free-free beam: (—), k-spectrum for $\widehat{L}_1$ from $\widehat{R}_{11}$; (−−), k-spectrum for $\widehat{L}_2$ from $\widehat{R}_{22}$.

	$\widehat{R}_{11}$			$\widehat{R}_{22}$		
γ	L_1 (m)	$\widehat{L}_1$ (m)	Error (m)	L_2 (m)	$\widehat{L}_2$ (m)	Error (m)
0.55 (free-free)	0.83	0.84	0.01	1.18	1.20	0.02

Table 8.3: Actual and estimated slot locations for the free-free beam with $\gamma = 0.55$.

8.5.3. Remarks

For the experimental specimens tested here, the kIFFT has been used to locate the slots. The method worked well for all the specimens tested, although the harmonics are clearer when the reflection coefficient is large. If the reflection coefficient is small, its harmonics may be masked by noise.

8.6. Locating multiple slots

Of great interest in the field of damage detection is the ability to locate multiple slots. In this section, it is shown that this can be achieved through analysis of the scattering coefficients.

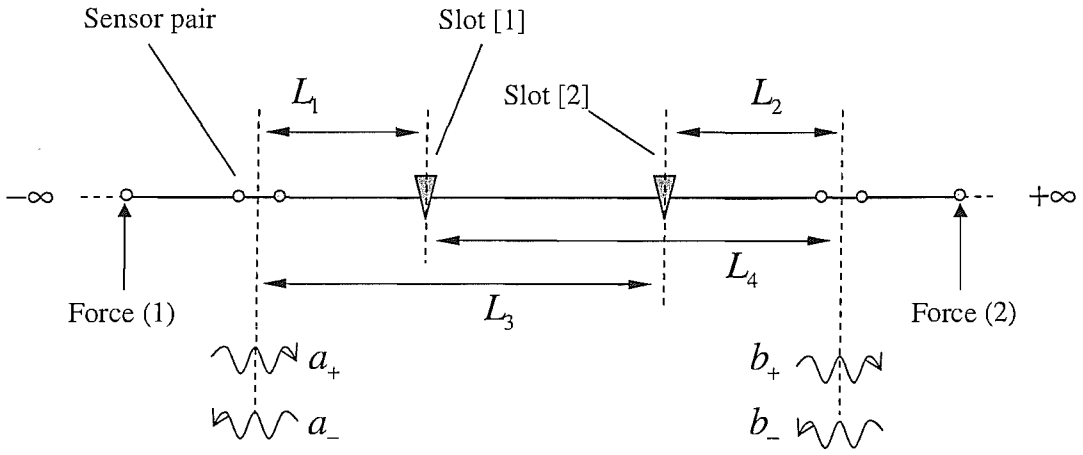

Fig. 8.10: Infinite beam model with two slots.

Fig. 8.10 illustrates an infinite beam with two slots. Both slots must be in-between the sensor pairs. The wavefield can be described by two equations, that are

$$a_- = \left\{ R_{11}^{[1]} e^{-2ik_e L_1} + \sum_{n=1}^{N} \left[R_{11}^{[2]} T_{12}^{[1]} T_{21}^{[1]} \right]^n \left[R_{22}^{[1]} \right]^{(n-1)} e^{-2ik_e \{L_1 + n(L_3 - L_1)\}} \right\} a_+ + \ldots$$
$$+ \left\{ \sum_{n=1}^{N} \left[T_{21}^{[1]} T_{21}^{[2]} \right]^n \left[R_{22}^{[1]} R_{11}^{[2]} \right]^{(n-1)} e^{-ik_e \{L_2 + L_3 + 2n(L_4 - L_2)\}} \right\} b_- \qquad (8.11)$$

$$b_+ = \left\{ R_{22}^{[2]} e^{-2ik_e L_2} + \sum_{n=1}^{N} \left[R_{22}^{[1]} T_{12}^{[2]} T_{21}^{[2]} \right]^n \left[R_{11}^{[2]} \right]^{(n-1)} e^{-2ik_e \{L_2 + n(L_4 - L_2)\}} \right\} b_- + \ldots$$
$$+ \left\{ \sum_{n=1}^{N} \left[T_{12}^{[1]} T_{12}^{[2]} \right]^n \left[R_{22}^{[1]} R_{11}^{[2]} \right]^{(n-1)} e^{-ik_e \{L_2 + L_3 + 2n(L_4 - L_2)\}} \right\} a_+ \qquad (8.12)$$

where the superscripts [1] and [2] denote the scattering coefficients of slots [1] and [2]. In Eqs. 8.11 and 8.12, the summation terms describe waves that scatter between the slots. These waves create additional k-harmonics that relate to the distance from the sensor pair plus multiples of the distance between the slots. If the second slot does not exist, Eqs. 8.11 and 8.12 are equivalent to Eqs. 5.12 and 5.13

If the measured scattering coefficients are found using Eqs. 5.15 and 5.16, from chapter 5 (§ 5.3), and Eqs. 8.11 and 8.12, it can be shown that

$$\widehat{R}_{11} = R_{11}^{[1]} e^{-2ik_e L_1} + \sum_{n=1}^{N} \left[R_{11}^{[2]} T_{12}^{[1]} T_{21}^{[1]}\right]^n \left[R_{22}^{[1]}\right]^{(n-1)} e^{-2ik_e\{L_1 + n(L_3 - L_1)\}} \tag{8.13}$$

$$\widehat{R}_{22} = R_{22}^{[2]} e^{-2ik_e L_2} + \sum_{n=1}^{N} \left[R_{22}^{[1]} T_{12}^{[2]} T_{21}^{[2]}\right]^n \left[R_{11}^{[2]}\right]^{(n-1)} e^{-2ik_e\{L_2 + n(L_4 - L_2)\}} \tag{8.14}$$

The reflection coefficients in Eqs. 8.13 and 8.14 do not represent a single reflected wave but are a combination of multiple reflections. However, the k-harmonic components of $\widehat{R}_{11}$ and $\widehat{R}_{22}$ in Eqs. 8.13 and 8.14 are related to the distances from the sensor pairs to each slot.

The magnitude of each successive k-harmonic component in $\widehat{R}_{11,22}$ depends upon the reflection and transmission coefficients of each discontinuity and, in general, would depend on damping. If there were many discontinuities, the amplitude of the reflected wave for each successive discontinuity decreases. This means that the magnitude of each successive k-harmonic component decreases also.

8.6.1. Experimental result

Two slots were cut in a beam specimen, as described in chapter 6. One slot has $\gamma = 0.45$ and the second has $\gamma = 0.64$. This specimen is different to the others in that the second slot is cut through the cross-section at an angle as illustrated in Fig. 8.11. The original

purpose of this specimen was to investigate how the reflection coefficients of a skewed slot differ from a slot that it is at 90° to the edge of the beam, although these results are not included in this thesis.

The skewed slot extends over 3cm and its location is given as the distance along the centre-line to the slot. Fig. 8.12 shows $|s(\Lambda)|^2$ for both reflection coefficients and the actual and estimated locations are given in Table 8.4. Again the agreement is good and the estimates are within a few centimetres of the actual locations.

	$\widehat{R}_{11}$			$\widehat{R}_{22}$		
γ	L_1 (m)	$\widehat{L}_1$ (m)	Error (m)	L_2 (m)	$\widehat{L}_2$ (m)	Error (m)
0.45	0.69	0.69	0.00	1.33	1.35	0.02
0.64 (slanted)	1.44	1.43	0.01	0.58	0.57	0.01

Table 8.4: Actual and estimated slot locations for the beam with two cracks.

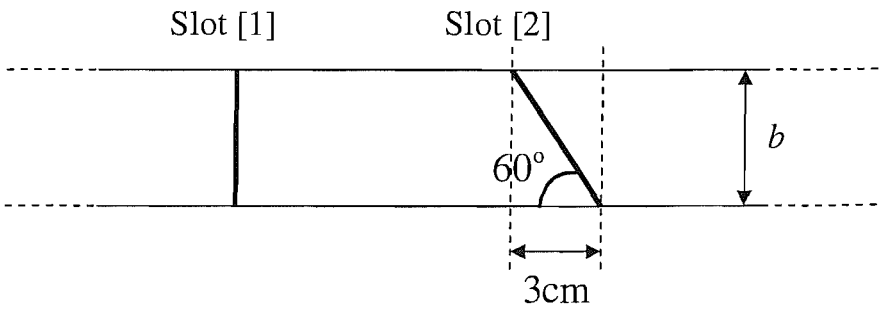

Fig. 8.11: Illustration of the experimental beam with two slots (note that the width of the beam is shown and the slot depth goes into the plane).

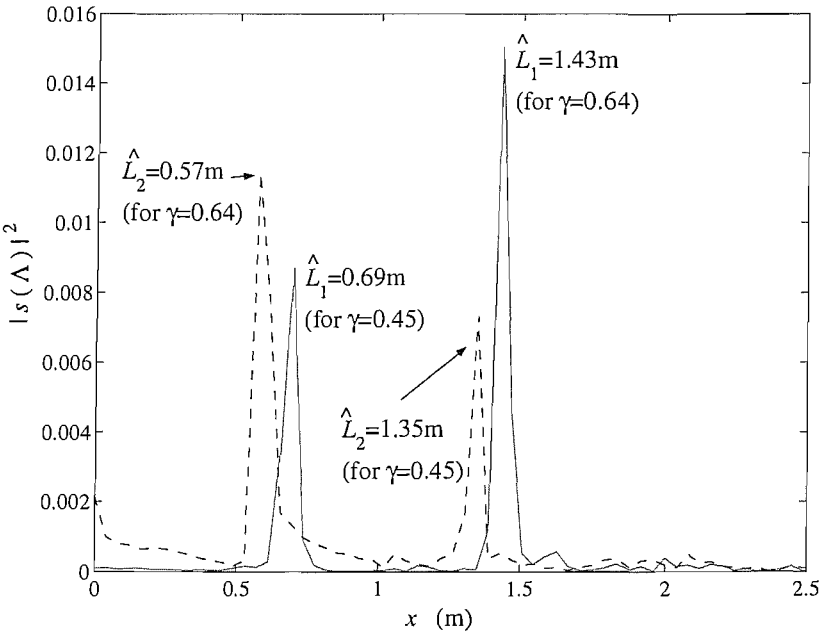

Fig. 8.12: Estimation of the location of two slots with $\gamma = 0.45$ and $\gamma = 0.64$: (—), k-spectrum for $\widehat{L_1}$ from $\widehat{R}_{11}$; (– –), k-spectrum for $\widehat{L_2}$ from $\widehat{R}_{22}$.

8.7. Summary

A method has been described for estimating the location of a slot in a beam, from the measured reflection coefficients. The modulating components of the reflection coefficients are related to the location of the slot. A wavenumber to space kIFFT is used to transform the reflection coefficients to determine the k-harmonics. To use this method the wavenumber must be known.

The method has been used to estimate the location of slots in numerical and experimental examples. The accuracy of the estimated locations depends on the resolution of the k-spectrum and experimental errors. Here, the experiments showed that the slots could be located to within a few centimetres. Moreover, it was possible to locate a shallow slot ($\gamma = 0.13$) and a slot in a beam with free-free boundary conditions. Furthermore, the method can also be applied to beams with multiple slots and a similar

level of accuracy has been obtained. Also, this approach is not restricted to slots and can be applied to any other types of scatterer.

The *k*IFFT method works better when the slot and hence the magnitude of the *k*-harmonic is large. If the slot is small, as in the case where $\gamma = 0.13$, the *k*-harmonics may be obscured by noise.

9. Locating slots from the phase of the point FRF

9.1. Introduction

In the previous chapter, a method for locating damage using the measured reflection coefficients was described. A disadvantage of this approach is the need to take measurements with sensor pairs either side of the region in which the slot might lie.

In this chapter, an alternative method of estimating the slot location is considered. The method analyses the phase of the point FRF, the k-harmonics of which are related to the distance between the excitation point and scatterers in the beam.

FRF methods have been considered before for damage detection in which the locations of the resonances and anti-resonances have been used to signify damage (e.g., [33]). Often, to assess the damage, the measured FRF is compared with a model of the undamaged or damaged structure. The method described herein does not require knowledge of the undamaged structure, other than the location of known discontinuities (such as ends or joints) and the wavenumber.

The method is described and is then illustrated by numerical and experimental results. In keeping with the experimental work, only the flexural waves will be considered here, although the method can be applied to other wave types.

9.2. Theory

The phase of a wave changes as it propagates and when it is scattered. In the following examples it is shown how this fact can be exploited to locate discontinuities.

9.2.1. Discontinuity in an infinite beam

Fig. 9.1 shows an infinite Timoshenko beam with a discontinuity. The beam is excited at $x = 0$ by a point transverse force, creating propagating and nearfield flexural waves which travel along the beam and reflect from the discontinuity.

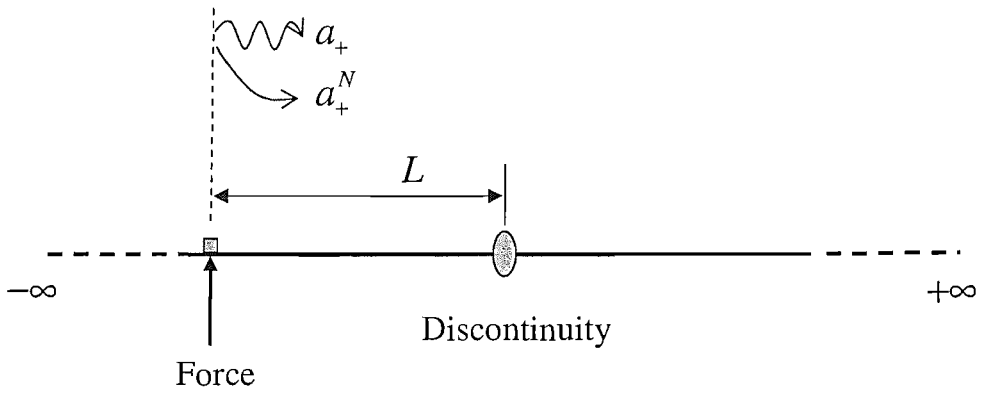

Fig. 9.1: An infinite beam with a discontinuity, excited by a point transverse force.

Neglecting damping and the contribution of nearfield waves that are scattered by the discontinuity, the accelerance at the excitation point, μ_p, is

$$\begin{aligned}\mu_p &= -\omega^2\left(a_+ + a_+^N + |R_{11}|\, a_+ e^{-2ik_t L + i\theta_{11}}\right) \\ &= -\omega^2\left(a_+ + a_+^N\right)\left[1 + \frac{|R_{11}|\, a_+ e^{-2ik_t L + i\theta_{11}}}{a_+ + a_+^N}\right]\end{aligned} \tag{9.1}$$

where the subscript p denotes that it is a point FRF. The phase of μ_p is θ_p and is given by

$$\theta_p = \mathrm{Im}\left\{\ln\left(-\omega^2\left(a_+ + a_+^N\right)\left[1 + \frac{|R_{11}|\, a_+ e^{-2ik_1 L + i\theta_{11}}}{a_+ + a_+^N}\right]\right)\right\}$$
$$= \pi + \mathrm{Im}\left\{\ln\left[a_+ + a_+^N\right] + \ln\left(1 + \frac{|R_{11}|\, a_+ e^{-2ik_1 L + i\theta_{11}}}{a_+ + a_+^N}\right)\right\} \tag{9.2}$$

In general, a_+ and a_+^N are complex such that $a_+ + a_+^N = Ce^{i\theta}$, where C is real, θ is a phase angle and both variables are frequency dependent. The second logarithmic term in Eq. 9.2 can be expanded as an infinite series. The first three terms of the series are

$$\theta_p = \pi + \theta + \mathrm{Im}\left\{\sum_{n=1}^{\infty} -(-1)^n \frac{1}{n}\left(\frac{|R_{11}|\, a_+ e^{-2ik_t L + i\theta_{11}}}{a_+ + a_+^N}\right)^n\right\} \tag{9.3}$$

$$= \pi + \theta + \mathrm{Im}\left\{\frac{|R_{11}|\, a_+ e^{-2ik_t L + i\theta_{11}}}{a_+ + a_+^N} - \frac{1}{2}\frac{(|R_{11}|\, a_+)^2 e^{-4ik_t L + 2i\theta_{11}}}{(a_+ + a_+^N)^2} + \ldots\right.$$
$$\left. + \frac{1}{3}\frac{(|R_{11}|\, a_+)^3 e^{-6ik_t L + 3i\theta_{11}}}{(a_+ + a_+^N)^3} + \ldots\right\} \tag{9.4}$$

The series in Eq. 9.4 includes an infinite number of complex exponential terms, the arguments of which relate to multiples of the distance $2L$. The magnitudes of the exponential terms depend on the reflection coefficient and, in general, on damping. Also, the phase component $e^{i\theta_{11}}$ and its multiples are often much more slowly varying with wavenumber in comparison to $e^{-2ik_t L}$ and its multiples. This is very similar to the problem in the last chapter and it is proposed that the location of a slot can be estimated by calculating the k-spectrum of the phase of the point FRF.

Similar expressions to Eq. 9.4 exist for finite beams, although the fact that waves travel in both directions and reflect at the ends of the beam make the expressions more complicated. However, the resulting expressions include a similar series of complex exponential terms with arguments relating to distance. These involve not only the distance to the discontinuity (i.e., the slot) but also the distances to the ends of the beam and other discontinuities.

To find the k-harmonic components of the phase and estimate the distance L, the kIFT (see previous chapter) is applied to θ_p. As in the previous chapter, the physical interpretation of the k-spectrum of the phase is unclear. Here it is treated as a spectrum and is complex. It might also be considered to be a modified cepstrum. The cepstrum is real and can be defined as the IFT of the logarithm of a complex spectrum [64]. The k-spectrum of the phase differs in that the imaginary part of the logarithm is taken to find the phase. The cepstrum has previously been applied in the wavenumber and spatial domains in [65, 66] to estimate scattering coefficients.

Here, θ_p is measured as a function of frequency but the kIFFT is applied in the wavenumber domain. As in the previous chapter, the phase must be resampled so that the sample spacing is constant as a function of wavenumber.

The experimental measurement of θ_p may have a D.C. offset and may also exhibit a trend. A D.C. offset or a trend in the measured phase may cause significant k-harmonics and leakage in the k-spectrum, at small values of x. These components might be reduced by removing the mean and the trend of the experimental data. The function `detrend` in Matlab can be used to remove the D.C. offset and any linear trend in the experimental data and this was used in the numerical and experimental work that follows.

9.3. Numerical examples

In this section a number of numerical examples are presented to show how the k-spectrum of the phase of the point FRF can be used to locate a notch. In each example the beam is modelled using Timoshenko beam theory and the lumped spring model is used to model the notch. The beam is mild steel with $E = 210\text{GNm}^{-2}$, $\rho = 7850\text{kgm}^{-3}$, $h = 0.006$ and $\upsilon = 0.3$. Moreover, the frequency vector is from 0.1 to 9600 Hz and has

16384 sample points.

9.3.1. A notch in an infinite beam

An infinite beam with a notch is illustrated in Fig. 9.1. Using the model with a crack depth of $\gamma = 0.50$, the point accelerance is calculated and shown in Fig. 9.2(a). The kIFFT is used to transform θ_p and determine the k-spectrum, which is presented in Fig. 9.2(b).

In Fig. 9.2(b), the first k-harmonic occurs when $x \approx L$. Estimating the location at the tip of the first peak, is was found that $x = 0.998L$ and the resolution of the x variable is approximately $0.037L$. Although it is difficult to see from Fig. 9.2(b), a very small k-harmonic occurs at $x = 2L$ and smaller ones occur at other multiples of L.

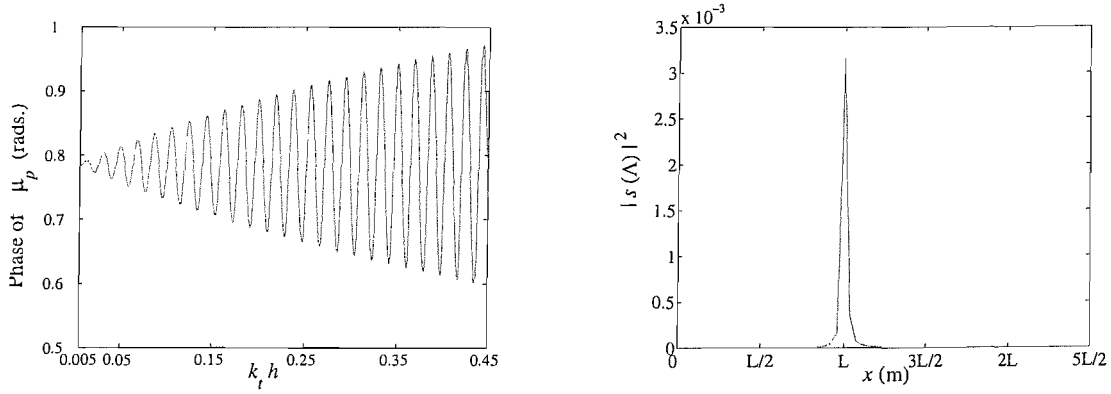

(a) Phase of the point accelerance.

(b) The k-spectrum of the phase.

Fig. 9.2: The phase and k-spectrum of the point accelerance of an infinite beam with a notch.

9.3.2. A notch in a finite beam

In a finite beam, waves reflect from the ends of the beam and any other discontinuities. Here, a finite beam with a single notch is considered and illustrated in Fig. 9.3, where L_0 and L_2 are the distances from the excitation to the ends of the beam and L_1 is the distance from the excitation to the notch.

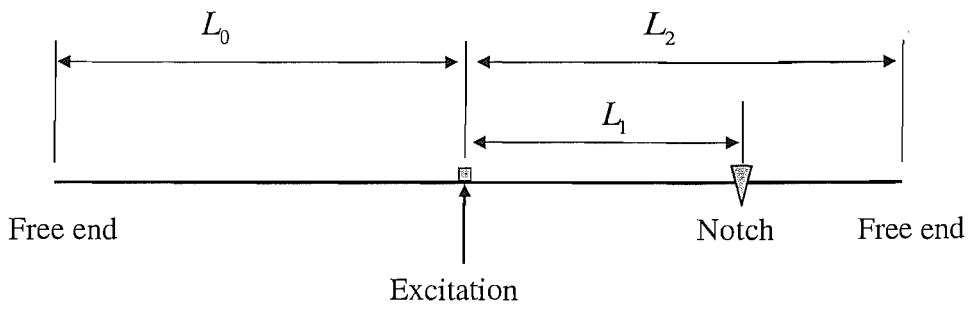

Fig. 9.3: Beam model for estimating the location of a notch.

The wavefield includes waves that travel in both directions and scatter from all discontinuities. Thus, one might expect that the k-harmonic components of the phase of the point FRF, and hence the peaks in the k-spectra, relate to distances from the excitation point to the discontinuities: L_0, L_1, L_2; plus multiples of these values, nL_0, nL_1, nL_2 (for $n = 1, 2, \ldots, \infty$); and sums of combined values and their multiples, e.g., $L_0 + L_1$, $nL_1 + L_2$, etc. .

The peaks in the k-spectrum can be related to known scatterers and, in some cases, it may be possible locate the notch with a single measurement. However, more than one measurement is often needed because the k-spectrum only describes the distances to the scatterers and not the direction in which they lie, in respect to the excitation.

In order to estimate the location of the damage, a measurement is made and the k-spectrum recorded. Known scatterers (e.g., the ends of the beam, joints) are identified in the k-spectrum and the distance from the excitation to the damage might also be estimated. The point FRF and k-spectrum are then measured at a different location. By noting how the k-harmonics move in respect to where the point FRF is measured, it is possible to note whether the k-harmonic associated with the damage moves closer to or further away from the measurement, thus, making it possible to determine on which side of the excitation the damage lies.

It is desirable to have a more systematic approach for locating the damage in the k-spectra. One of the difficult issues is identifying higher k-harmonics of the scatterers. Whether or not higher k-harmonics exist in the k-spectrum, over the distances that are of interest, depend on the specific problem. One method that might be used is illustrated in Fig. 9.4.

At the top of Fig. 9.4, the beam is shown with a notch. Excitation position {1} is located to the left of the notch. Firstly, the point FRF and k-spectrum are measured for excitation position {1} (the peaks in the k-spectrum are illustrated in the figure). The mirror image of the k-spectrum is also plotted, using the excitation as the origin, as illustrated in Fig. 9.4. Plotting the k-spectrum and its mirror image in this way shows all the possible locations of the scatterers on each side of the excitation. If peaks occur outside the length of the beam, they can be ignored.

Suppose that the excitation is moved to position {2} (see Fig. 9.4). The k-spectrum is plotted again, this time with excitation position {2} as the origin. The peaks that correspond to the locations of the scatterers should concur with the relative locations found when excitation position {1} was used. These peaks are ringed in Fig. 9.4. The

comparison between the k-spectrum for excitations positions {1} and {2} show that the notch is to the right of the excitation.

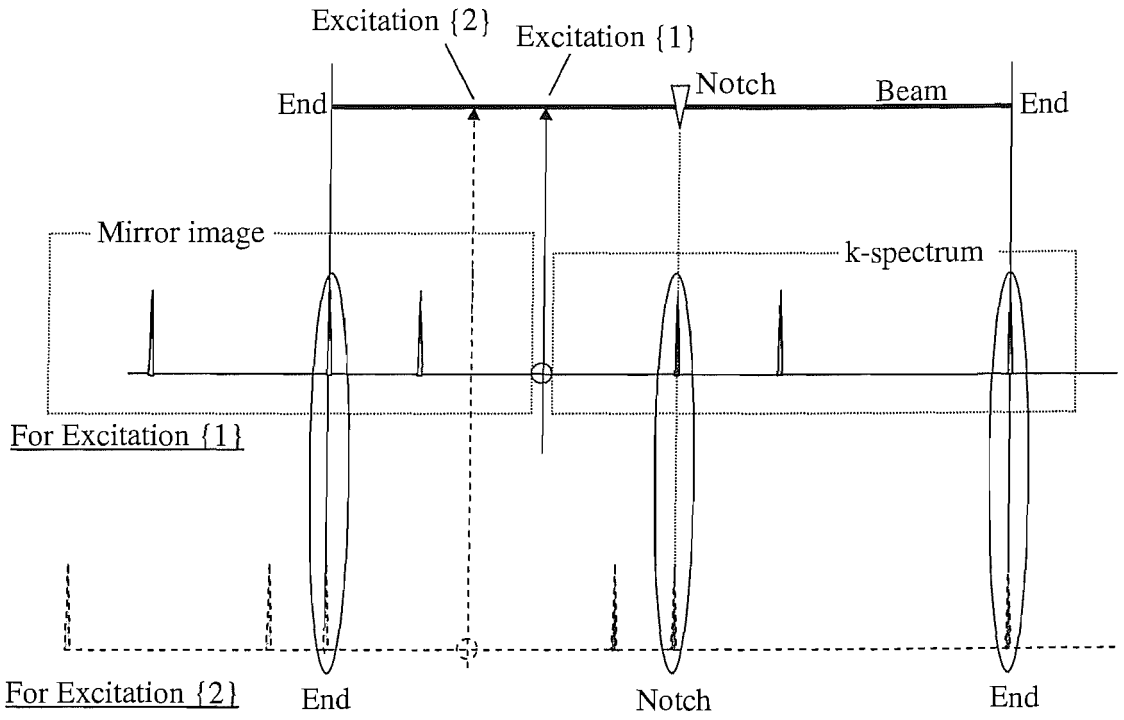

Fig. 9.4: Estimating damage location using the k-spectrum of the phase of the point FRF.

The example shown in Fig.9.4 illustrates a systematic approach to locating damage. In practice, the peaks differ in magnitude and higher k-harmonics can occur. Both these factors can make the identification of the scatterers more difficult.

9.3.2.1. Numerical example

The damaged finite beam in Fig. 9.5 is modelled using TBT, with the properties $E = 210\text{GNm}^{-2}$, $\rho = 7850$, $h = 0.006$ and $\upsilon = 0.3$. In addition, the total length of the beam is $L = 6\text{m}$ and the notch is modelled using a lumped spring with a depth of $\gamma = 0.50$. The location of the notch and excitations, relative to the left-hand end of the beam, are shown in Fig. 9.5, where the notch is at $x = 3\text{m}$ and excitations positions {1} and {2} are at $x = 2.50\text{m}$ and 2.25m, respectively. The distance between excitations positions {1} and {2} is $L' = 0.25\text{m}$.

The magnitude and phase of the point accelerance, for excitation position {1}, are presented in Fig. 9.6. This result shows how the notch causes changes in the resonance frequencies and the occurrence of new resonances in the FRF for the damaged case. It should be further added that this example is noise free.

The k-spectrum is calculated from the phase of the point accelerance for excitation positions {1} and {2}. As described in the previous subsection, the k-spectra are plotted along with their mirror images, with the origin at the excitation and this is shown in Fig. 9.7. The vertical lines in the plot show the k-harmonics that remain in the same place when the excitation is moved. This result shows that the notch is to the right of both excitations. The location of the notch is estimated, with good accuracy, as $x = 2.99\text{m}$ for both excitations.

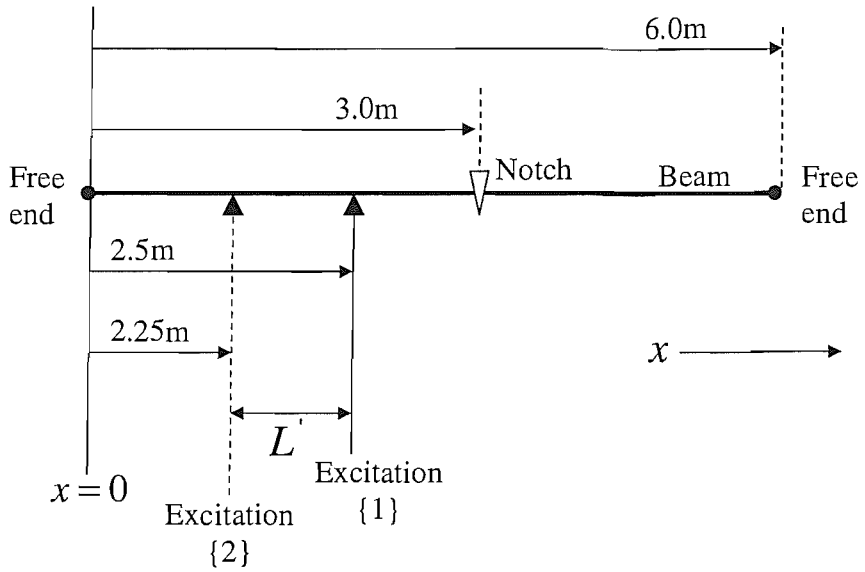

Fig. 9.5: A damaged finite beam.

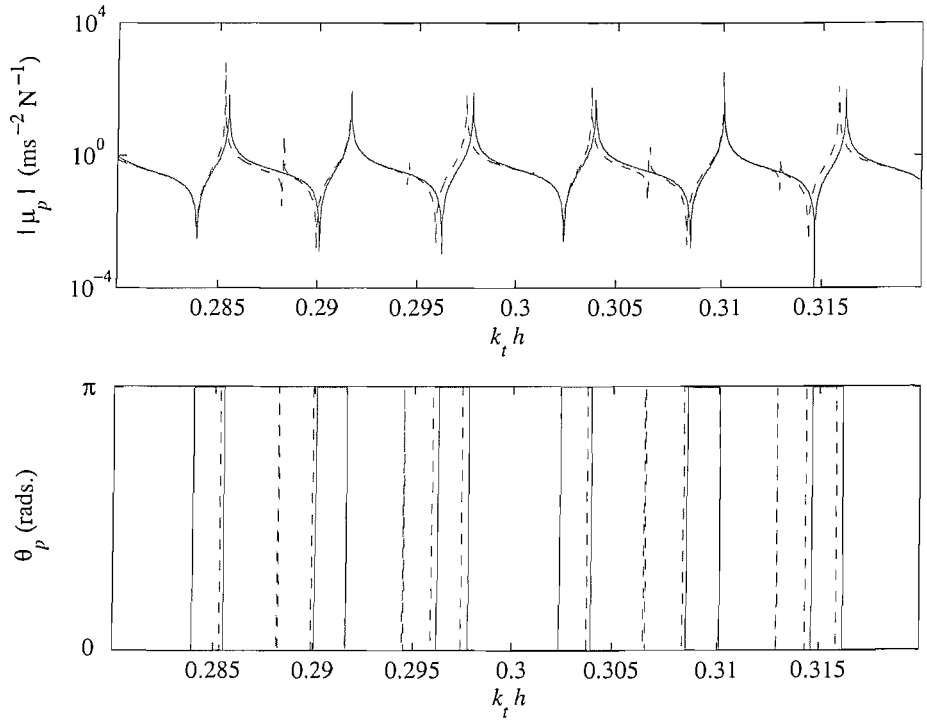

Fig. 9.6: Point accelerance of a finite beam: (—), undamaged; (– –), damaged (for which $\gamma = 0.50$).

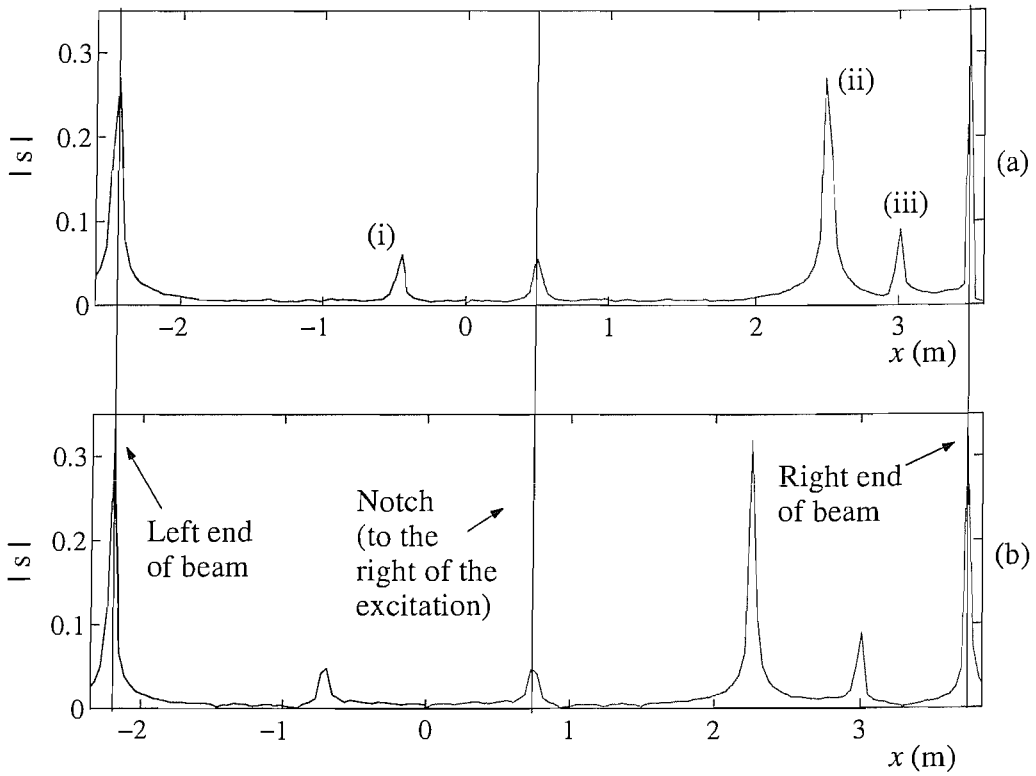

Fig. 9.7: k-spectra for a beam with one crack: (a), excitation position {1}; (b), excitation position {2}. Other peaks: (i) the mirror image of the notch k-harmonic; (ii) the mirror image of the left end k-harmonic; (iii) k-harmonic associated with the distance to the notch plus the distance to the left end.

9.3.3. A finite beam with two notches

Given that reflections from each scatterer in the beam can result in peaks in the k-spectrum, one might expect that peaks will occur in the event that the beam has multiple notches. The following example is used to show that the k-spectrum might be

used for locating two notches.

Fig. 9.8 shows a model of a beam with two notches. This example uses the same material properties as the example in § 9.3.2.1. Again, a lumped-spring is used to model both notches which are of depth $\gamma = 0.50$. Fig. 9.8 details the locations of the excitations and the notches, where the only difference between this and the example in § 9.3.2.1 is the second notch at $x = 4$m.

The k-spectra for each excitation are shown in Fig. 9.9. Both notches are predicted to be to the right of the excitations and the notch locations are estimated as $x = 2.99$m, for the first notch, and $x = 3.99$m for the second notch. This result shows that both notches can be located with a good degree of accuracy.

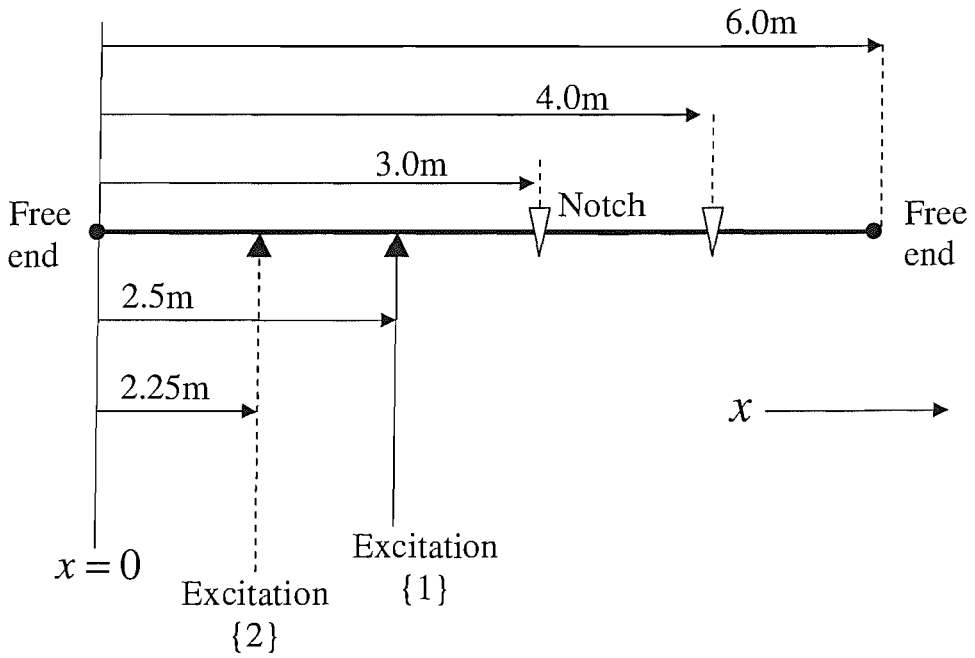

Fig. 9.8: A finite beam with two notches.

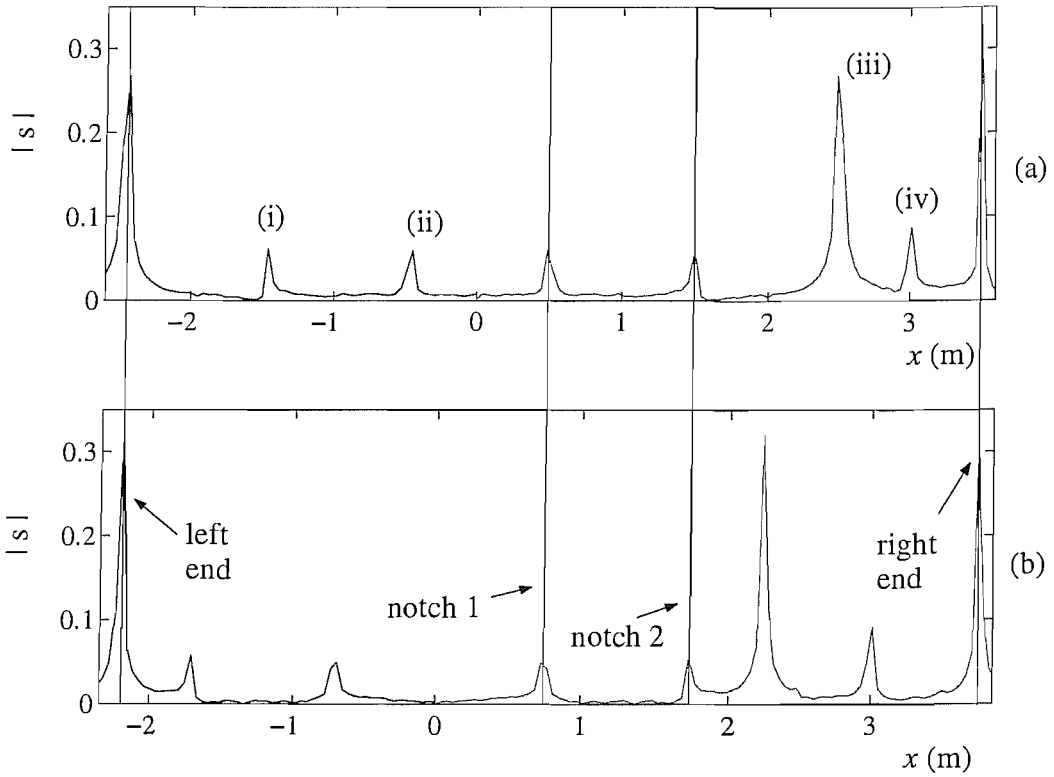

Fig. 9.9: k-spectra for a beam with two notches: (a), excitation position {1}; (b), excitation position {2}. Other peaks: (i) the mirror image of crack 2 k-harmonic; (ii) the mirror image of notch 1 k-harmonic; (iii) the mirror image of the left end k-harmonic; (iv) k-harmonic associated with the distance to notch 2 plus the distance to the left end.

9.4. Experimental results

The point accelerance was measured on each of the experimental slotted beam specimens described in chapter 6, in which slots were cut into the beams and the beams were tested with each end placed in sand. For each specimen, the kIFFT was used to calculate the k-spectra from the phase. The location of the slot in each specimen was

estimated from the k-spectrum and the results are presented in this section.

The point accelerance was measured by placing an accelerometer at a point on the centre-line of the beam and an instrumented hammer was used to excite the beam at the same point but on the opposite side of the beam. Fig. 9.10 shows the point accelerance measured on the specimen with $\gamma = 0.55$. In this result, the measured phase has a D.C. offset that appears to be roughly constant over the range $k_e h = 0.05$ to $k_e h = 0.40$. At low wavenumbers, when $k_e h < 0.05$, the phase changes erratically. The coherence between the force input and the response was much less than 1 in this region, and it is thought that a poor signal to noise ratio (particularly at anti-resonances) may cause these errors.

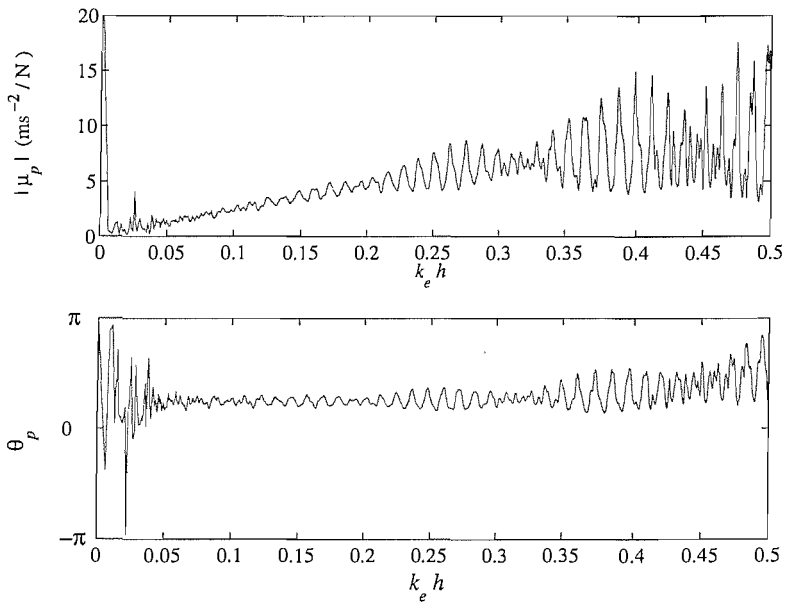

Fig. 9.10: Point accelerance measured on the slotted beam with $\gamma = 0.55$.

Including the portion of the phase below $k_e h = 0.05$ in the calculation of the k-spectrum affects the result. Fig. 9.11 shows two k-spectra for the specimen with

$\gamma = 0.55$, that have been derved from the result shown in Fig. 9.10. In one of the k-spectra, the kIFFT was applied over the range $k_e h = 0$ to $k_e h = 0.50$. In the second result, the k-spectrum was calculated for the range $k_e h = 0.05$ to $k_e h = 0.50$. By not including the errors, the noise floor of the k-spectrum is lowered. Given that the magnitudes of the peaks in the k-spectrum are related to the size of the reflection coefficients of the scatterers, it may be more difficult to locate smaller scatterers (e.g. small cracks) if the noise floor in the k-spectrum is of a similar magnitude. Also in Fig. 9.11, it is noted that at very low values of x there appears a large peak. This is thought to result from the trend seen in the measured phase at higher wavenumbers.

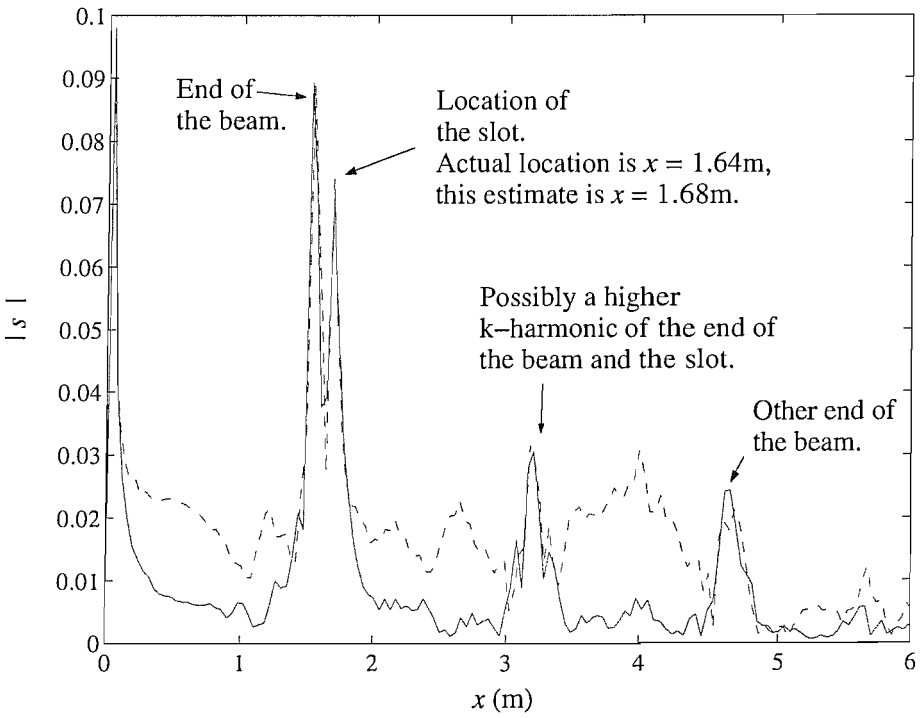

Fig. 9.11: The k-spectra of a slotted beam specimen with $\gamma = 0.50$:(––), calculated over the range $k_e h = 0$ to $k_e h = 0.55$; (—), calculated over the range $k_e h = 0.05$ to $k_e h = 0.50$.

The peaks in Fig. 9.11 indicate the locations of the scatterers. The peak at $x \approx 1.50$m represents one end of the beam, the next peak represents the slot and is at $x \approx 1.68$m and the peak at $x \approx 4.58$m is the other end of the beam. The actual location of the slot is $x = 1.64$m and the accuracy of the location estimates are determined by the resolution of the x variable, which is approximately 5cm for this result.

The results measured on the specimens with $\gamma = 0.22$ to $\gamma = 0.62$ were processed using the *k*IFFT and the *k*-spectrum was used to estimate the locations of the slots. The results are given in Table. 9.1.

γ	actual (m)	estimate (m)
0.22	1.510	1.570
0.34	1.530	1.471
0.39	1.550	1.630
0.50	1.530	1.579
0.55	1.640	1.680
0.62	1.475	1.496

Table 9.1: Actual and estimated slot locations.

For these results, the location of the slot was known. However, when the location of the slot is unknown it can be located by plotting the mirror image of the *k*-spectrum, as was explained in § 9.3.2.1 and 9.3.3. As an example, this method was implemented on the specimen with $\gamma = 0.50$. Two *k*-spectra for this specimen are shown in Fig. 9.12. The first excitation is located at 1.07m from the slot and the second is at 0.77m. The

estimates from the k-spectra are 1.08m and 0.79m, respectively. From the plots of the k-spectra, the slot is correctly predicted as being to the right of both excitations.

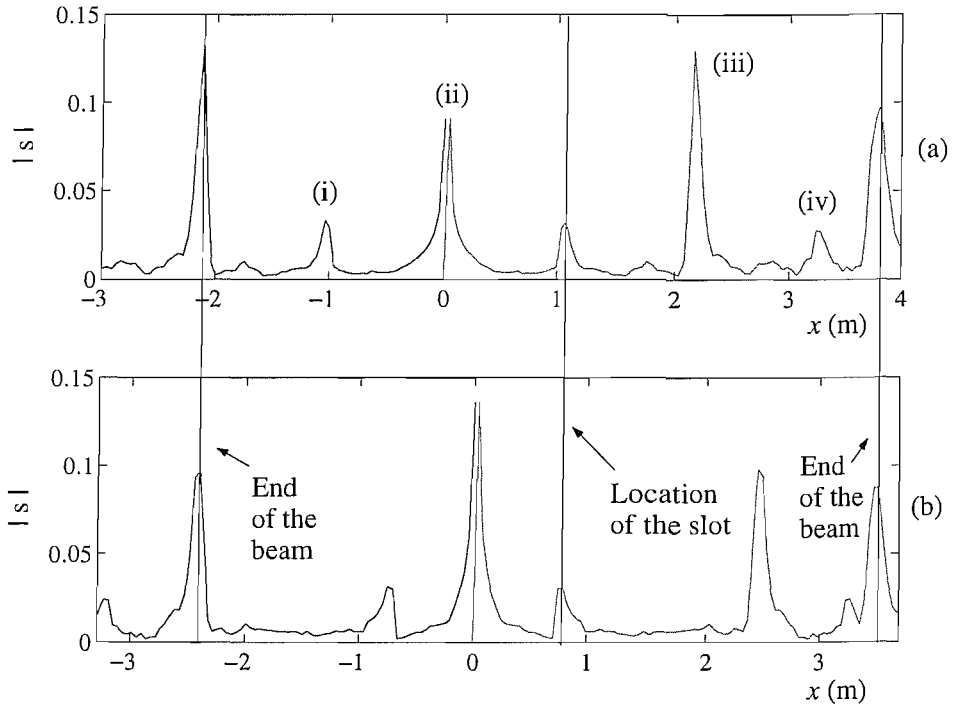

Fig. 9.12: k-spectra for the specimen with $\gamma = 0.50$: (a), excitation at 1.07m from the slot; (b), excitation at 0.77m from the slot. Other peaks: (i) the mirror image of the slot k-harmonic; (ii) k-harmonics associated with the trend in the data; (iii) the mirror image of the left end k-harmonic; (iv) k-harmonic associated with the distance to the slot plus the distance to the left end.

9.5. Summary

In this chapter, it was shown that discontinuities can be located from the phase of the measured point FRF. The phase of the point FRF, as a function of wavenumber, comprises many modulating components that relate to the distances from the excitation

to any scatterers in the beam. By applying the kIFFT to the phase, these distances can be estimated from the peaks in the k-spectrum.

The magnitude of the peaks in the k-spectrum depend on the reflection coefficient of that particular scatterer. Therefore, it is easier to locate large damage. Small notches/slots have small peaks in the k-spectra and estimating their location can be more difficult if there is a significant amount of noise present in the measurement.

The location of a peak in the k-spectrum gives the distance from the excitation to the scatterer but does not give information in regards to on which side of the excitation the scatterer lies. This must be deduced from the locations of known scatterers, such as the ends of the beam, and it may be necessary to make further measurements, moving the excitation and sensor to other locations, in order to estimate the location of the damage.

The numerical and experimental results given here show that the method can be used to show the existence of a slot and estimate its location. The accuracy of the estimates depend on the resolution of the spatial variable which is defined by the frequency range of the measurement. Increasing this range, as in chapter 8, can improve the resolution.

10. Further work and concluding remarks

In this final chapter, the main outcomes of the thesis are discussed and suggestions are made for possible improvements and further work.

10.1. Outcomes

In this thesis, the use of wave scattering for detection of notches/slots in beams has been considered. In summary, the main contributions are:

- A method for combining FE and wave models (FESE) has been used to estimate the scattering coefficients of a notch or slot in a beam. This model provides a more detailed description of the dynamic properties of the damage. The numerical results show the significance of wave mode conversion at increased notch or slot depths and frequency. The FESE modelling method, as applied here, can be used to estimate scattering coefficients of other types of discontinuity, which might have application in other areas of structural analysis.

- A slot was cut into a beam and its scattering coefficients were measured. The experimental results for a number of specimens with different slot depths are given. The measured reflection coefficient might be used to signify the existence of a damage.

- By comparing the measured reflection coefficients to the FESE models, it was shown that the depth of the slot can be estimated. This is dependent on the damage model used and the correct estimation of the wavenumber and the material

properties.

- It was also shown that the location of the slot can be estimated from the measured reflection coefficients. This is accomplished through application of the inverse Fourier transform from the wavenumber to spatial domains. This method is applicable to other types of discontinuity.

- Finally, in addition to the previous point, a method for estimating the location of a slot from a measurement of the point FRF is given. This method is quick and straightforward and can be used to signify the existence of damage as well as estimate its location. In this method the locations of other discontinuities in the beam, such as boundaries, are found also.

Using the wave method for damage detection has a number of advantages:

- it can be used to show the existence and location of damage and may give an estimate of the extent of the damage;

- it is useful for remote sensing of damage; and

- the experimental methods are well-known and would not necessarily require a skilled operator for use.

Equally, there are a number of important limitations, which might be addressed in further work:

- smaller slots have smaller reflection coefficients;

- experimental error and noise makes measuring small damage difficult, at low frequencies in particular;

- to estimate the reflection coefficients, the wavenumber of the beam must be known; and
- strong reflectors other than the damage can cause conditioning problems, which affect the estimates of the reflection coefficient.

10.2. Further work

10.2.1. Improvements

In certain areas the methods described in this thesis can be improved. In the FESE model, the reflections at the interface boundary between the FE and SE models is a concern when the reflection coefficient of a discontinuity is small. The discontinuity at the interface is due to the fact that the models are different but the constraints that are used assume that the models have equivalent stress distributions. It may be possible to improve the assembly procedure by using polynomial functions to describe the constraints and find the best fit of the nodes on the FE interface boundary to those on the SE models. This might be optimised by minimising the reflection coefficient of the boundary.

Experimental error and noise is a major issue and is very important when trying to measure small scale damage. Some of the effects of errors are illustrated in chapters 5 to 7, however, these only give examples. In further work, it would be useful to establish the sensitivities of the measured scattering coefficients and wavenumber to experimental error. This may highlight the important errors that affect the accuracy of the damage detection and suggest further improvements to the method.

10.2.2. Damage identification

The problem of identifying damage has not been considered here. However, one might be able to identify the damage from the scattering coefficients. The scattering coefficients have two important features: phase and magnitude. Therefore, it may be possible to treat the scattering coefficients as a form of "spectral ident" which can be compared to a database of other common discontinuities in order to predict its type. Given that a major component of the phase of the measured reflection is related to the location of the damage, identification might be better based on the power scattering coefficients.

It is possible that two types of discontinuity have similar scattering coefficients over the same frequency range. For example, it was suggested in [37] that the reflection coefficient of a notch resembles that of a point mass. If this is the case, the identification procedure is more complicated as a number of possibilities may suggest themselves for a particular result. However, it may be possible to rule out certain types of discontinuity.

Another approach to identification might be to combine the wave method given here with other damage detection methods such as modal and FRF methods. In each of the methods, damage affects the parameters in different ways and, as such, combining this knowledge might lead to better predictions of the damage type.

10.2.3. Sensor/actuator technologies

To apply the wave method to autonomous SHM requires actuators and sensors suitable for when the structure is in use. The methods described in this thesis use hammer excitation and standard (though small) accelerometers. Sensor/actuator technologies such as piezo actuators might be mounted on the structure to make measurements, and further work should consider the most appropriate technologies to implement the

experimental methods considered in the previous chapters.

10.2.4. Extension to non-uniform beams and two dimensional problems

It is desirable that the wave method can be used to detect damage in more general structures such as a non-uniform beams and plates. In theory, if the wavenumber is known for a non-uniform beam, it may be possible to apply the same methods as given here.

It is not obvious how the scattering methods described herein can be adapted and used for damage detection in two dimensions. Clearly, damage in plates will also scatter the waves that travel through the plate. Damage detection using the wave method in two dimensions poses a number of problems, in particular that of the the direction of wave propagation.

10.3. Concluding remarks

The results in this thesis have shown that wave methods can be used to predict the existence of a slot and estimate its location and depth with a good degree of accuracy. It is more difficult to measure smaller slots given the size of experimental errors in comparison to the magnitude of the reflection coefficients. The methods work best when the reflection coefficients are large, i.e., at high frequencies or with large slot depths.

A. Appendix

A.1. Calculation of Timoshenko wavenumbers

Eqs. 3.14, 3.15 and 3.19 are combined to give

$$\begin{bmatrix} k^2GA\kappa - \rho A\omega^2 & ikGA\kappa \\ ikGA\kappa & \rho I\omega^2 - k^2EI - GA\kappa \end{bmatrix} \begin{Bmatrix} v \\ \psi \end{Bmatrix} = 0 \tag{A.1}$$

The wavenumbers are found from the determinant of the matrix in Eq. A.1 and are the roots of

$$0 = k^4 - \left(k_0^2 + k_s^2\right)k^2 + (k_0^2k_s^2 - k_b^4) \tag{A.2}$$

where $k_0 = \omega\sqrt{\rho/E}$ is the longitudinal wave number, $k_s = \omega\sqrt{\rho/G\kappa}$ is the shear wave number and $k_b = \sqrt[4]{\omega^2\rho A/EI}$ is the Euler-Bernoulli wave number.

A.2. Time averaged wave power

Table A.1 gives the time averaged power of waves for each rod and beam model [67]. The time averaged power is quoted in terms of the phase and group velocity, the values of which can be found in Table A.2 [67].

Model	Time Averaged Wave Power
LRT	$\frac{1}{2}\rho A c_g^{(0)} \omega^2 \lvert a_+^A \rvert^2$
LVRT	$\frac{1}{2(1-[\upsilon g k_0]^2)} \rho A c_g^{(L)} \omega^2 \lvert a_+^A \rvert^2$
EBT	$\frac{1}{2}\rho A c_g^{(b)} \omega^2 \lvert a_+^F \rvert^2$
TBT	$\frac{1}{2}\rho A \omega^2 c_t \left(1 + \frac{k_1^2 - k_s^2}{k_b^4}\right) \lvert a_+^F \rvert^2$

Table A.1: Time averaged wave power.

Model	Phase Velocity	Group velocity
LRT	$c_0 = \sqrt{E/\rho}$	$c_{g0} = c_0$
LVRT	$c_L = c_0 \sqrt{1 - (\upsilon g k_0)^2}$	$c_{gL} = c_L \left\{1 - (\upsilon g k_0)^2\right\}$
EBT	$c_b = \sqrt{\omega}\, \sqrt[4]{EI/\rho A}$	$c_{gb} = 2c_b$
TBT	$c_t = \frac{c_b \sqrt{2}}{\sqrt{(\delta^2+\beta^2) + \sqrt{(\delta^2-\beta^2)^2+4}}}$	$c_{gt} = c_t \left\{1 + \frac{1}{\left(\frac{k_1^2}{k_b^4} \sqrt{(k_0^2-k_s^2)^2+4k_b^4}\right)-1}\right\}$

Table A.2: Phase and group velocities for rods and beams.

References

[1] **Staszewski, W., Boller, C.** and **Tomlinson, G.**, Health Monitoring of Aerospace Structures: Smart Sensor Technologies and Signal Processing, Wiley, U.K., 2004.

[2] **Farrar, C., Doebling, S.** and **Nix, D.**, *Vibration based structural damage identification*, Philosophical Transactions of the Royal Society of London A, Vol. 359, pp. 131–149, 2001.

[3] **Worden, K., Manson, G.** and **Allman, D.**, *Experimental validation of a structural health monitoring methodology: Part I. Novelty detection on a laboratory structure*, Journal of Sound and Vibration, Vol. 259, No. (2), pp. 323–343, 2003.

[4] **P.F. Rizos, N. A.** and **Dimarogonas, A.**, *Identification of crack location and magnitude in a cantilever beam from the vibration modes*, Journal of Sound and Vibration, Vol. 138, No. (3), pp. 381–388, 1990.

[5] **Ostachowicz, W.** and **Krawczuk, M.**, *Analysis of the effect of cracks on the natural frequencies of a cantilever beam*, Journal of Sound and Vibration, Vol. 150, No. (2), pp. 191–201, 1991.

[6] **Doyle, J.**, Wave Propagation in Structures: Spectral Analysis Using Fast Discrete Fourier Transforms, Springer, 2nd edn., 1997.

[7] **Dimarogonas, A.**, *Vibration of cracked structures: A state of the art review*, Engineering Fracture Mechanics, Vol. 55, No. 5, pp. 831–857, 1996.

[8] **Panteliou, S. D., Chondros, T. G., Argyrakis, V. C.** and **Dimarogonas, A. D.**, *Damping factor as an indicator of crack severity*, Journal of Sound and Vibration, Vol. 241, No. 2, pp. 235–245, 2001.

[9] **Chu, Y.** and **Shen, M.-H.**, *Analysis of forced bilinear oscillators and the application to cracked beam dynamics*, AIAA, Vol. 30, No. (10), pp. 2512–2519, 1992.

[10] **Irwin, G.**, *Analysis of stresses and strains near the end of a crack transversing plate*, Journal of Applied Mechanics - Transactions of the ASME, Vol. 24, pp. 361–364, 1957.

[11] **Tada, H., Paris, P.** and **Irwin, G.**, The Stress Analysis of Cracks Handbook, American Society of Mechanical Engineers, 3rd edn., 2000.

[12] **Rivola, A.** and **White, P.**, *Bispectral analysis of the bilinear oscillator with application to the detection of fatigue cracks*, Journal of Sound and Vibration, Vol. 216, No. (5), pp. 889–910, 1998.

[13] **Vanhoenacker, K., Schoukens, J., Guillaume, P.** and **Vanlanduit, S.**, *The use of multisine excitations to characterise damage in structures*, Mechanical Systems and Signal Processing, Vol. 18, pp. 43–57, 2004.

[14] **Qain, G.-L., Gu, S.-N.** and **Jiang, J.-S.**, *The dynamic behaviour and crack detection of a beam with crack*, Journal of Sound and Vibration, Vol. 138, No. (2), pp. 233–243, 1990.

[15] **Mei, C., Karpenko, Y., Moody, S.** and **Allen, D.**, *Analytical approach to free and forced vibrations of axially loaded cracked Timoshenko beams*, Journal of Sound and Vibration, Vol. 291, pp. 1041–1060, 2006.

[16] **Fernndez-Sez, J.** and **Navarro, C.**, *Fundamental frequency of cracked beams in bending vibrations: an analytical approach*, Journal of Sound and Vibration 256, , No. (1), pp. 17–31, 2002.

[17] **Routolo, R.** and **Surace, C.**, *Natural frequencies of a bar with multiple cracks*, Journal of Sound and Vibration, Vol. 272, pp. 301–316, 2004.

[18] **Sinha, J., Friswell, M.** and **Edwards, S.**, *Simplified models for the location of cracks in beam structures using measured vibration data*, Journal of Sound and Vibration, Vol. 251, No. 1, pp. 13–38, 2002.

[19] **Cawley, P.** and **Adams, R.**, *The location of defects in structures from measurements of natural frequencies*, Journal of Strain Analysis, Vol. 14, pp. 49–57, 1979.

[20] **Thyagarajan, S., Schulz, M., Pai, P.** and **Chung, J.**, *Detecting structural damage using frequency response functions*, Journal of Sound and Vibration, Vol. 210, No. (1), pp. 162–170, 1998.

[21] **Chondros, T. G., Dimarogonas, A. D.** and **Yao, J.**, *Vibration of a beam with a breathing crack*, Journal of Sound and Vibration, Vol. 239, No. 1, pp. 57–67, 2001.

[22] **Gopalakrishnan, S.** and **Doyle, J.**, *Super spectral-elements for wave propagation in structures with local non-uniformities*, Computer methods in applied mechanics and engineering, Vol. 121, pp. 77–90, 1995.

[23] **Mahmood, A., Popplewell, N.** and **Shah, A.**, *Scattering of elastic waves by cracks in steel pipes*, Vol. VIII International conference on recent advances in structural dynamics of *Southampton, UK, 14-16 July 2003*, 2003.

[24] **Lakshmanan, K.** and **Pines, D.**, *Modelling damage in rotorcraft flexbeams using wave mechanics*, Smart materials and structures, Vol. 6, pp. 383–392, 1997.

[25] **Ewins, D.**, Modal testing: Theory and practice, Research Studies Press, 1984.

[26] **Lele, S.** and **Maiti, S.**, *Modelling of transverse vibration of short beams for crack detection and measurement of crack extension*, Journal of Sound and Vibration, Vol. 257, No. (3), pp. 559–583, 2002.

[27] **Nandwana, B.** and **Maiti, S.**, *Detection of the location and size of a crack in stepped cantilever beams based on measurements of natural frequencies*, Journal of Sound and Vibration, Vol. 203, No. (3), pp. 435–446, 1997.

[28] **Alvandi, A.** and **Cremona, C.**, *Assessment of vibration-based damage identification techniques*, Journal of Sound and Vibration, Vol. 192, pp. 179–202, 2006.

[29] **Baminos, Y., Douka, E.** and **Trochidis, A.**, *Crack identification in beam structures using mechanical impedance*, Journal of Sound and Vibration, Vol. 256, No. (2), pp. 287–297, 2002.

[30] **Lee, U.** and **Shin, J.**, *A frequency-domain method of structural damage identification formulated from the dynamic stiffness method*, Journal of Sound and Vibration, Vol. 257, No. (4), pp. 615–634, 2002.

[31] **Lui, D., Gurgeni, H.** and **Veidt, M.**, *Crack detection in follow section structures through coupled response measurements*, Journal of Sound and Vibration, Vol. 261, pp. 17–29, 2003.

[32] **Owolabi, G., Swamidas, A.** and **Seshadri, R.**, *Crack detection using changes in frequencies and amplitudes of frequency response functions*, Journal of Sound and Vibration, Vol. 265, pp. 1–22, 2003.

[33] **Douka, E., Bamnios, G.** and **Trochidis, A.**, *A method for determining the location and depth of cracks in double-cracked beams*, Applied Acoustics, Vol. 65, pp. 997–1008, 2004.

[34] **Dharmaraju, N.** and **Sinha, J. K.**, *Some comments on the use of antiresonance for crack identification in beams*, Journal of Sound and Vibration, Vol. 286, pp. 669–671, 2005.

[35] **Palacz, M.** and **Krawczuk, M.**, *Analysis of longitudinal wave propagation in a cracked rod by the spectral element method*, Computers and structures, Vol. 80, pp. 1809–1816, 2002.

[36] **Palacz, M., Krawczuk, M.** and **Ostachowicz, W.**, *The dynamic analysis of a cracked Timoshenko beam by the spectral element method*, Journal of Sound and Vibration, Vol. 264, pp. 1139–1153, 2003.

[37] **Rousseau, M., Waters, T.** and **Mace, B.**, *An audio-frequency wave technique for damage detection in beams*, Proceedings of the 5th international conference on damage assessment in structures (DAMAS 2003), Southampton, UK, 1-3 July, pp. 433–442, 2003.

[38] **Wang, C.** and **Rose, L.**, *Wave reflection and transmission in beams containing delamination and inhomogeneity*, Journal of Sound and Vibration, Vol. 264, pp. 851–872, 2003.

[39] **Su, Z., Ye, L.** and **Lu, Y.**, *Guided Lamb waves for identification of damage in composite structures: A review*, Journal of Sound and Vibration, , No. 295, pp. 753–780, 2006.

[40] **Viktorov, I.**, Rayleigh and Lamb Waves, Plenum Press, 1970.

[41] **Cawley, P.** and **Alleyne, D.**, *The use of Lamb waves for the long range inspection of large structures*, Ultrasonics, , No. 34, pp. 287–290, 1996.

[42] **Cawley, P.** and **Alleyne, D.**, *The interaction of Lamb waves with defects*, IEEE Trans. on Ultrasonics, Ferroelectrics and Frequency Control, , No. 39, pp. 381–397, 1992.

[43] **Hurlebaus, S., Niethammer, M., Jacobs, L.** and **Valle, C.**, *Automated methodology to locate notches with Lamb waves*, Acoustics Research Letters Online, , No. 2, pp. 97–102, 2001.

[44] **Cracknell, A.**, Ultrasonics, Wykeham Publications, 1980.

[45] **Wang, C., Rose, J.** and **Chang, F.**, *A synthetic time-reversal imaging method for structural health monitoring*, Smart Material and Structures, Vol. 13, pp. 415–423, 2004.

[46] **Lin, X.** and **Yuan, F.**, *Detection of multiple damages by prestack reverse-time migration*, AIAA Journal, Vol. Vol. 39, No. No.11, pp. 2206–2215, 2001.

[47] **Samuel, P.** and **Pines, D.**, *A review of vibration-based techniques for helicopter transmission diagnostics*, Journal of sound and vibration, , No. 282, pp. 475–508, 2005.

[48] **Kim, H.** and **Melhem, H.**, *Damage detection of structures by wavelet analysis*, Engineering Structures, Vol. 26, pp. 347–362, 2004.

[49] **Chang, C.-C.** and **Chen, L.-W.**, *Vibration damage detection of a Timoshenko beam by spatial wavelet based approach*, Applied Acoustics, Vol. 64, pp. 1217–1240, 2003.

[50] **Worden, K., Manson, G.** and **Fieller, N.**, *Damage detection using outlier analysis*, Journal of Sound and Vibration, Vol. 229, No. (3), pp. 647–667, 2000.

[51] **Hadjileontiadis, L. J., Douka, E.** and **Trochidis, A.**, *Crack detection in beams using kurtosis*, Computers and structures, Vol. 83, pp. 909–919, 2005.

[52] **Graff, K.**, Wave Motion in Elastic Solids, Dover, 1991.

[53] **Timoshenko, S.**, *On the correction for shear of the differential equation for transverse vibrations of prismatic bars*, Philosophy Magazine, pp. 744–746, 1921.

[54] **Cowper, G.**, *The shear coefficient in Timoshenko's beam theory*, Journal of Applied Mechanics, ASME, Vol. 33, No. 2, pp. 335–340, 1966.

[55] **Abbas, B.** and **Thomas, J.**, *The second frequency spectrum of Timoshenko beams*, Journal of Sound and Vibration, Vol. 51, No. 1, pp. 123–137, 1977.

[56] **Mace, B.**, *Wave reflection and transmission in beams*, Journal of Sound and Vibration, Vol. 97, No. (2), pp. 237–246, 1984.

[57] **Petyt, M.**, Introduction to finite element analysis, Cambridge University Press, 1990.

[58] **Fahy, F.**, Sound and Structural Vibration, Academic Press, 1995.

[59] **Mace, B., Jones, R.** and **Harland, N.**, *Wave transmission through structural inserts*, Journal of the Acoustic Society of America, Vol. 109, No. 4, pp. 1417–1421, 2001.

[60] **Timoshenko, S.** and **Goodier, J.**, Theory of Elasticity, McGraw-Hill, New York, 1970.

[61] **Mace, B.** and **Halkyard, C.**, *Time domain estimation of response and intensity in beams using wave decomposition and reconstruction*, Journal of Sound and Vibration, Vol. 230, No. (3), pp. 561–589, 2000.

[62] **Halkyard, C.** and **Mace, B.**, *Structural intensity in beams - waves, transducer systems and the conditioning problem*, Journal of Sound and Vibration, Vol. 185, No. 2, pp. 279–298, 1995.

[63] **Bendat, L.** and **Piersol, J.**, Analysis of Random Data, 1974.

[64] **Oppenheim, A.** and **Schafer, R.**, Digital Signal Processing, Prentice Hall, 1975.

[65] **Khalili, N.** and **Hammond, J.**, *Application of cepstral techniques for the determination of reflection coefficients for dispersive systems - 1. Theory and numerical results*, Mechanical systems and signal processing, Vol. 7, No. 5, pp. 425–435, 1993.

[66] **Khalili, N.** and **Hammond, J.**, *Application of cepstral techniques for the determination of reflection coefficients for dispersive systems - 2. Comparison*

between theory and experiment, Mechanical systems and signal processing, Vol. 7, No. 5, pp. 437–449, 1993.

[67] **Cremer, L., Heckl, M.** and **Ungar, E.**, Structure Borne Sound, Springer-Verlag, 1973.